KARADENİZ TECHNICAL UNIVERSITY
THE GRADUATE SCHOOL OF NATURAL AND APPLIED SCIENCES

DEPARTMENT OF ELECTRICAL AND ELECTRONICS ENGINEERING

MODELLING AND CONTROL OF 6/8 EXTERNAL ROTOR SWITCHED RELUCTANCE MOTOR

DOCTORATE THESIS

MUSTAFA AYDEMIR

APRIL 2023
TRABZON

KARADENİZ TECHNICAL UNIVERSITY
THE GRADUATE SCHOOL OF NATURAL AND APPLIED SCIENCES

DEPARTMENT OF ELECTRICAL AND ELECTRONICS ENGINEERING

MODELLING AND CONTROL OF 6/8 EXTERNAL ROTOR SWITCHED RELUCTANCE MOTOR

MUSTAFA AYDEMIR
ORCID : - - -

This thesis is accepted to give the degree of
DOCTOR OF PHILOSOPHY
By
The Graduate School of Natural and Applied Sciences at
Karadeniz Technical University

The Date of Submission : 30 / 01 /2023
The Date of Examination : 05 / 04 /2023

Thesis Supervisor : Prof. Dr. Halil İbrahim OKUMUŞ
ORCID : - - -

Trabzon 2023

PREFACE

The switched reluctance motor (SRM) was an interesting topic regarding the electromechanical torque generation principle. The starting point of this Phd thesis work was to investigate this type of electric machine which could be used as a low cost, direct drive in-wheel electric traction motor. Throughout the four years of research and experimental study period, the usage of the SRM espacially for mobility applications was well understood from my point of view.

Firstly, I'd like to thank to my advisor Prof. Dr. H. İbrahim OKUMUS for encouraging me to select this Phd thesis topic and his supports during the thesis study. I'd like to thank to Prof. Dr. Mustafa ULUTAS and Asst. Prof. Hakan KAHVECI for their constructive suggestions as the thesis monitoring comitee. Special thanks to all our department staff for their kind and friendly approach during this period.

At the beginning of the thesis work, I had difficulty finding the SRM prototype in Türkiye. Thanks to Prof. Dr. M. Timur AYDEMIR, he recommended me to contact with one of his friends Prof. Dr. Ferhat DALDABAN in Erciyes University in Kayseri. Special thanks to Prof. Dr. DALDABAN and Assoc. Prof. Nurettin USTKOYUNCU for their helps about providing me the three phase 6/8 external rotor switched reluctance motor. I used this motor's geometric parameters to build the laboratory prototype.

This Phd thesis was financially supported by TUBITAK (The Scientific and Technological Research Council of Türkiye) under 1002 support program with the project number 119E020. It's my pleasure to thank to TUBITAK for the financial support.

Last but not least, I'd like to thank to my parents for their moral supports. They are the actual enthusiasts behind my curiosity to science and technology. I hope that I'll have more opportunities throughout my life to make lots of contributions to the technological advancement of the humanity.

Mustafa AYDEMIR

Trabzon 2023

THESIS ETHICS STATEMENT

I hereby declare that, I finished this Phd thesis which I presented with the title of "Modelling and Control of 6/8 External Rotor Switched Reluctance Motor" under the responsibility of my advisor (Prof. Dr. Halil İbrahim OKUMUS) from start to finish. I collected the datas/samples myself. I did the experiments/analysis in the related laboratuaries. I showed the informations which I provided from other sources inside the text and resources. I acted properly according to the research and ethic rules during the study and I accept all the legal results in case of otherwise emerged. 05/04/2023

Mustafa AYDEMİR

CONTENTS

Page Number

Doktora Tezi
ÖZET

6/8 DIŞTAN ROTORLU ANAHTARLAMALI RELÜKTANS MOTORUN MODELLENMESİ VE DENETİMİ

Mustafa AYDEMIR

Karadeniz Teknik Üniversitesi
Fen Bilimleri Enstitüsü
Elektrik Elektronik Mühendisliği Anabilim Dalı
Danışman: Prof. Halil İbrahim OKUMUŞ
2023, 83 Sayfa, 10 Sayfa Ek

Bu çalışmada, altı statör ve sekiz rotor kutuplu dıştan rotorlu anahtarlamalı relüktans motorun Matlab & Simulink ortamında modellenmesi ve denetleyici tasarımı yapıldı. Motor denetiminde önemli bir parametre olan faz akı bağlantısının (flux linkage) tahmini, sadece faz akımının giriş olarak kullanıldığı yapay sinir ağları yöntemiyle gerçekleştirilerek literatüre özgün bir katkı sağlandı. Bunun için literatürde "nonlinear autoregressive network with exogenous input - NARX Neural Network" olarak tanımlanan "dıştan girişli doğrusal olmayan özbağlanımlı sinir ağı" olarak adlandırılabilecek olan bir yapay zeka ağ türü seçildi. Geliştirilen faz akı bağlantısı tahmin algoritmasının gerçek zamanlı uygulaması yapıldı. Elde edilen sonuçlar, literatürde bulunan önemli diğer tahmin yöntemleriyle elde edilen sonuçlarla karşılaştırmalı olarak incelendi. Ek olarak rotor ve statör kutuplarının hizalanma durumunu tespit etmeyi sağlayan ekonomik ve kolay uygulanabilir bir hall etkili konum algılama sistemi de geliştirilerek patent başvurusu yapıldı.

Tez çalışmasında elde edilen sonuçlar, NARX sinir ağının anahtarlamalı relüktans motoru faz akı bağlantısı tahmininin rotor konumundan bağımsız olarak, sadece faz akımı kullanılarak gerçekleştirilebileceğini göstermektedir. Elde edilen sonuçlar, rotor konum bilgisi ile birlikte faz akımının giriş olarak kullanıldığı "Sonlu elemanlar analizi yöntemi ve moment denge yöntemi (torque balance method)" ile yapılan faz akısı tahminiyle karşılaştırıldığında, NARX sinir ağıyla yapılan faz akı bağlantısı tahmininin, faz akısı bağlantısı formülü kullanılarak çevrim dışı hesaplanan değerlere daha yakın sonuç verebildiği gözlemlenmiştir. Ayrıca, hall etkili sensörlerin ARM'de doğru yerleşimiyle, özellikle elektrikli taşıtlarda teker içi doğrudan sürüşlü uygulamalarda 2000 devir/dakika altındaki hızlarda çalışmak üzere tasarlanan dıştan rotorlu anahtarlamalı relüktans motorun, yük altında, özel bir moment dalgalılık azaltma yöntemi kullanılmadan %13 seviyesinde bir moment dalgalanmasında çalışmasına katkı sağladığı görülmüştür.

Anahtar Kelimeler: Anahtarlamalı relüktans motor, NARX NN, Faz akısı tahmini, Rotor konum tespiti, Teker içi elektrik motoru.

PhD. Thesis

SUMMARY

MODELLING AND CONTROL OF 6/8 EXTERNAL ROTOR SWITCHED RELUCTANCE MOTOR

Mustafa AYDEMIR

Karadeniz Technical University
The Graduate School of Natural and Applied Sciences
Electrical and Electronics Engineering Graduate Program
Supervisor: Prof. Halil İbrahim OKUMUS
2023, 83 Pages, 10 Pages Appendix

In this study, external rotor switched reluctance motor with six stator and eight rotor poles modelled in Matlab & Simulink and the controller was designed. The phase flux linkage was estimated with artificial neural networks in which solely the phase currents were used as the input. For this purpose, one type of artificial intelligence network, which is called “Nonlinear Autoregrassive Network with Exogenous Input - Narx Neural Network” was selected as the network architecture. The real-time application of the developed phase flux estimation algorithm was performed. The results were examined comparatively with the results obtained from other important phase flux estimation methods found in the literature such as finite element analysis method, torque balance method and voltage balance method in which the inputs of the phase flux estimator was phase currents and the rotor position. In addition, a patent application was made for the economic and easily applicable hall effect type rotor position detection system, developed throughout the Phd thesis study. The motor was successfully operated with PI controller using this rotor position detection system.

The results obtained in this Phd thesis study showed that the phase flux linkage estimation of the switched reluctance motor can be achieved with the NARX Neural Network in which only the phase current is taken as the input, regardless of the rotor position information. In addition, the developed hall-effect sensor system contributed to the moment ripple of the external rotor - switched reluctance motor which was measured as 13%.

Key Words: Switched reluctance motor, NARX NN, Phase flux linkage estimation, Rotor position detection, In wheel electric motor.

FIGURES DIRECTORY

Page Number

TABLES DIRECTORY

Page Number

SYMBOLS DIRECTORY

SRM	Switched reluctance motor
ERSRM	External rotor switched reluctance motor
ANN	Artificial neural network
LUT	Lookup table
NN	Neural network
NARX	Nonlinear autoregressive network with external input
FEA	Finite element analysis
TBM	Torque balance method
PC	Personel computer
DSP	Digital signal processor
WOS	Web of science
OLC	Open loop control
FEMM	Finite element method magnetics

1. GENERAL INFORMATION

1.1. Introduction

Switched reluctance motors (SRMs) attract attention in electric traction applications with their simple, robust, and fault-tolerant structure [1]. After the rare earth permanent magnet price crisis which occurred in 2011 [2], the research on reluctance type electric machines was accelerated as they could be a substitute to the permanent magnet type electric machines [1,3].

SRM can continue torque generation if one stator phase is in faulty condition [4]. Hence, the motor has a fault-tolerant structure. Additionally, the moment-speed characteristics make it preferable in electric vehicle traction applications [5].

In-wheel electric motors bring the advantage of eliminating the powertrain components such as gears and differentials. This both reduces the vehicle's weight and increases the free space in the vehicle [6].

In [3] electric motor types used as electric vehicle traction motors were compared. According to this research, switched reluctance motor scored the highest mark. Its superiority among others was explained especially regarding wide speed range, robustness, and ease of manufacturing criteria.

As efficiency, weight, and cost are major issues in electric vehicle applications, in [1], SRM was scored with the highest mark among other types of electrical motors too. The results supported the work in [3].

With the evaluation of this information, switched reluctance motor was selected as the in-wheel traction motor considering its ease of manufacturing, robustness, fault-tolerant structure, and low-cost features. Additionally, within the last decade, the major problematic features of this type of motor were mostly solved which were torque ripple and acoustic noise by either making mechanical modifications to the motor structure or designing advanced control algorithms [13, 14].

The external rotor three-phase switched reluctance motor (ERSRM) studied in this Ph.D. thesis has six stator and eight rotor poles. Working principles, modelling, and control techniques were investigated and explained in detail. A novel phase flux linkage estimation technique based on an artificial neural network (ANN) and an original rotor position detection system was introduced. The developed algorithm and the Hall sensor system were explained in detail and the real-time measurement results were given.

1.2. SRM Working Principle

1.2.1. Torque Generation Principle

The stator phase inductance depending on the rotor angle and phase current is expressed in the torque formula of the SRM [7].

SRM working principle relies on a variable reluctance path that occurs between each stator and rotor pole. The main principle of the rotor's angular rotation is the orientation of the magnetic flux lines to the lower reluctance route. And this results in mechanical torque which rotates the motor.

Obtaining the SRM electrical equations and the torque equation was explained as follows [8].

Derivation of voltage equation:

$$v = i\,.R_m + \frac{d\emptyset}{dt} \tag{1.1}$$

If the derivation term in (1.1) is expanded, (1.2) is obtained.

$$v = i.R_m + \frac{\partial\emptyset}{\partial i}\frac{di}{dt} + \frac{\partial\emptyset}{\partial\theta}\frac{d\theta}{dt} \tag{1.2}$$

$$L = \frac{\partial\emptyset}{\partial i} \tag{1.3}$$

$$K_b = \frac{\partial\emptyset}{\partial\theta} = \frac{\partial(L(\theta,i).i)}{\partial\theta} = i.\frac{\partial L}{\partial\theta} \tag{1.4}$$

In (1.3) and (1.4), $L(\theta,\mathrm{i})$ is inductance and $K_b(\theta,\mathrm{i})$ is reverse electromotive force (emf) respectively. Using (1.3) and (1.4) at (1.2), (1.5) is obtained.

$$v = i\,R_m + L(\theta,\mathrm{i})\frac{di}{dt} + K_b(\theta,\mathrm{i})\frac{d\theta}{dt} \tag{1.5}$$

$$\frac{d\theta}{dt} = \omega \tag{1.6}$$

$$v = i\,R_m + L(\theta, \mathrm{i})\frac{di}{dt} + K_b(\theta, \mathrm{i}).\,\omega \tag{1.7}$$

In (1.1), the phase current term is multiplied by the terms on both sides and this results in (1.8).

$$vi = i^{\,2}.\,R_m + i\frac{d\emptyset}{dt} \tag{1.8}$$

In (1.8), the $i^{\,2}.\,R_m$ term is the ohmic loss, $i\frac{d\emptyset}{dt}$ could be expressed in power components as shown in (1.9).

$$i\frac{d\emptyset}{dt} = \frac{dW_m}{dt} + \frac{dW_f}{dt} \tag{1.9}$$

- $\frac{dW_m}{dt}$: Instantaneous mechanical power.
- $\frac{dW_f}{dt}$: Magnetic field stored power.

$$\frac{dW_m}{dt} = T.\,\omega = T.\frac{d\theta}{dt} \tag{1.10}$$

If (1.10) is written in (1.9), (1.11) is obtained.

$$i\frac{d\emptyset}{dt} = T.\frac{d\theta}{dt} + \frac{dW_f}{dt} \tag{1.11}$$

From (1.11), torque equation (1.12) is written.

$$T = i\frac{d\emptyset}{d\theta} - \frac{dW_f(\theta,\emptyset)}{d\theta} \tag{1.12}$$

In (1.12), the magnetic field stored energy (W_f) depends on the flux linkage. The coenergy formula is used to write this expression depending on the phase current. The coenergy formula is represented in Figure 1.1. It is represented by the area under the Ø(θ, i) curve. For each constant rotor angle (θ), it is formulated as (1.13).

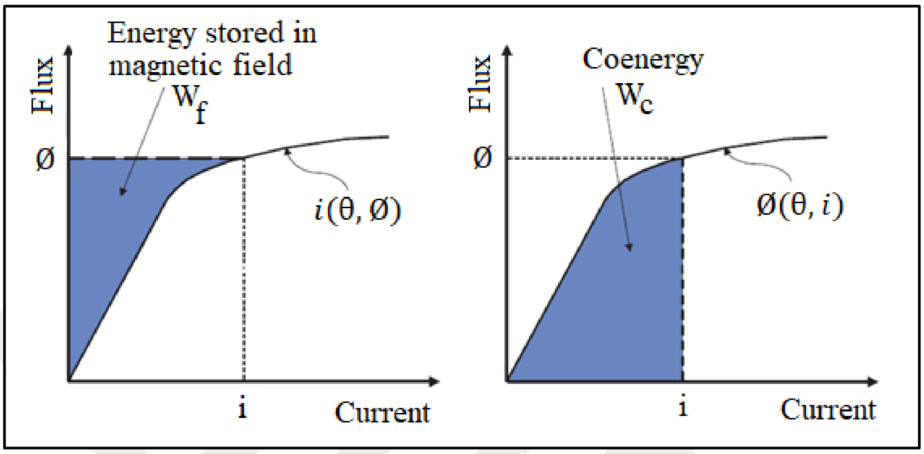

Figure 1.1. Energy and coenergy representation [26].

$$W_c = \int_0^i Ø(\theta, I)\mathrm{di} \tag{1.13}$$

The flux linkage formula is (1.14):

$$Ø = \mathrm{L} \, . \, \mathrm{i} \, ; \tag{1.14}$$

$$W_c = \frac{1}{2} L(\theta, \mathrm{i}). i^2 \tag{1.15}$$

$$W_c + W_f = i \, . Ø \tag{1.16}$$

In (1.16), both sides are derivated and the generalized torque equation is found as (1.20).

$$dW_c + dW_f = i \, . \, dØ + Ø \, . \, \mathrm{di} \tag{1.17}$$

$$dW_f = i \, . \, dØ + Ø \, . \, \mathrm{di} - dW_c \tag{1.18}$$

$$T = i\frac{d\emptyset}{d\theta} - \frac{i.d\emptyset + \emptyset.di - dW_c}{d\theta} \tag{1.19}$$

$$T = \frac{dW_c - \emptyset.di}{d\theta} \tag{1.20}$$

To write (1.20) completely dependent on current and inductance, the derivative of the coenergy term is written from (1.15) and finally, the torque equation is achieved as (1.21). The relationship between torque-inductance-current and rotor angle is interpretable from the torque equation.

$$T = \frac{1}{2}i^2\frac{dL}{d\theta} - L.i.\frac{di}{d\theta} \tag{1.21}$$

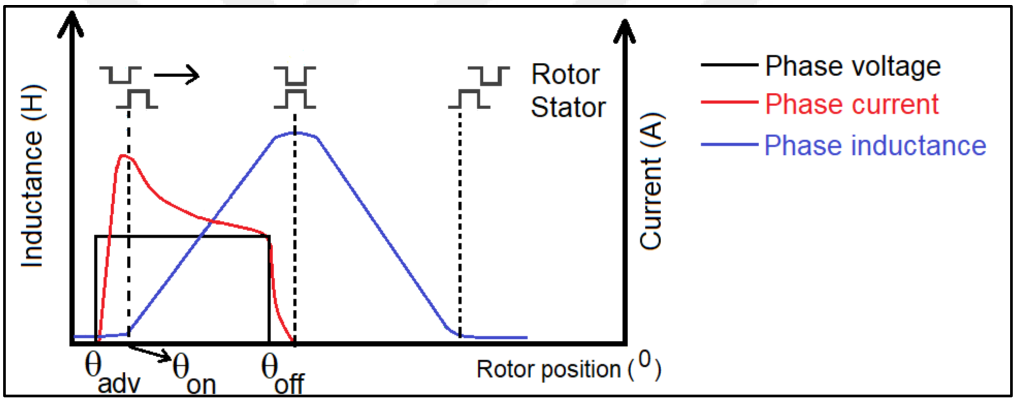

Figure 1.2. Theoretical current, voltage, and inductance waveform of an ERSRM [9].

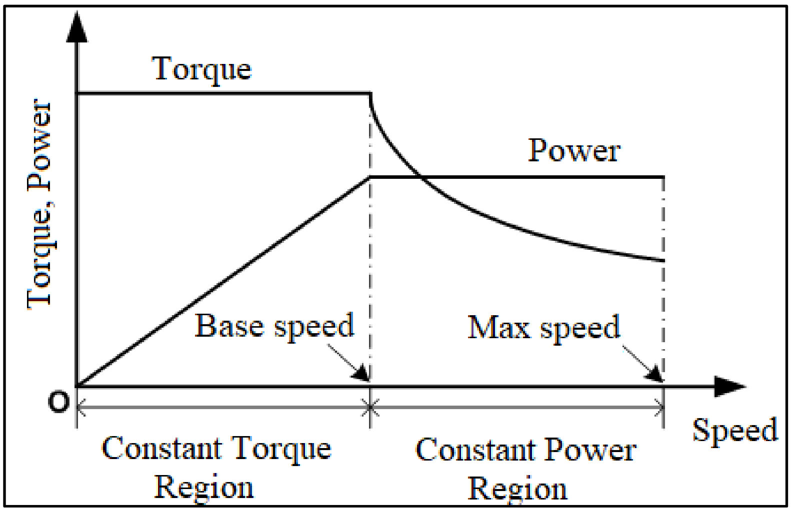

Figure 1.3. Moment speed graph of SRM [1].

The theoretical current and inductance waveforms subject to the applied stator voltage are shown in Figure 1.2. The moment speed graph of a typical switched reluctance type electrical machine is given in Figure 1.3.

1.2.2. SRM Driver Working Principle

The driver topology for three-phase SRM is in Figure 1.4. The switching states are named magnetization, freewheel, and demagnetization working regions as shown in Figure 1.5.

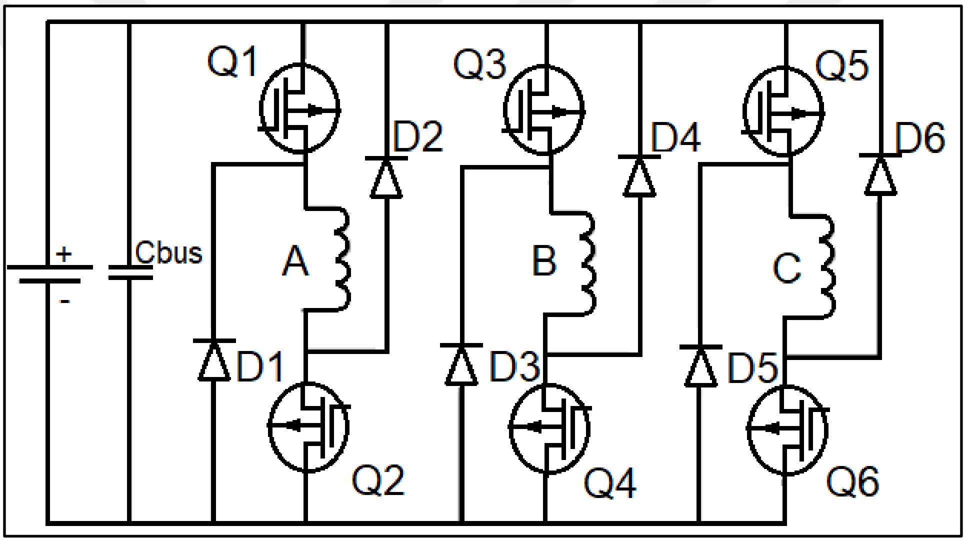

Figure 1.4. The asymmetrical half-bridge converter topology [9].

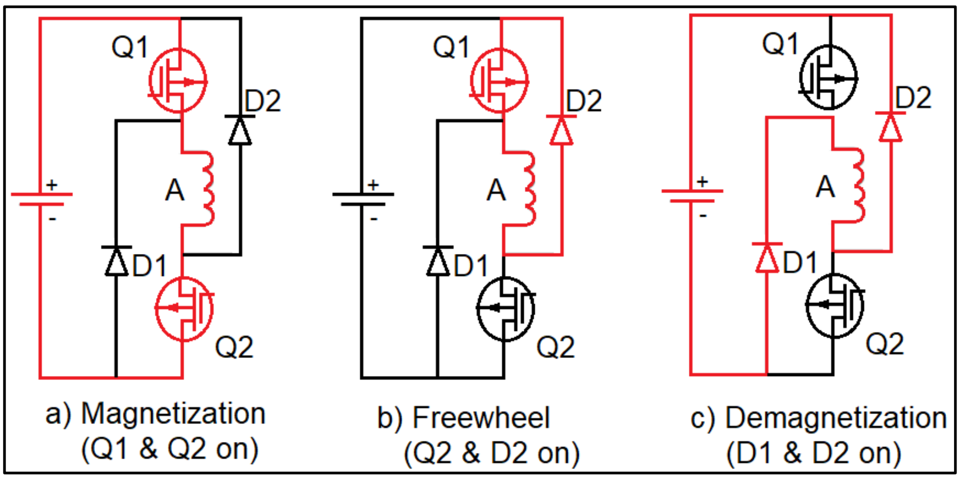

Figure 1.5. Switching states for motor operation [9].

For motor operation, each stator phase should be energized at the rotor-stator poles alignment position and de-energized when the rotor-stator poles are fully aligned as shown in Figure 1.6. To operate the motor at the positive torque region, phase excitation is performed according to this principle.

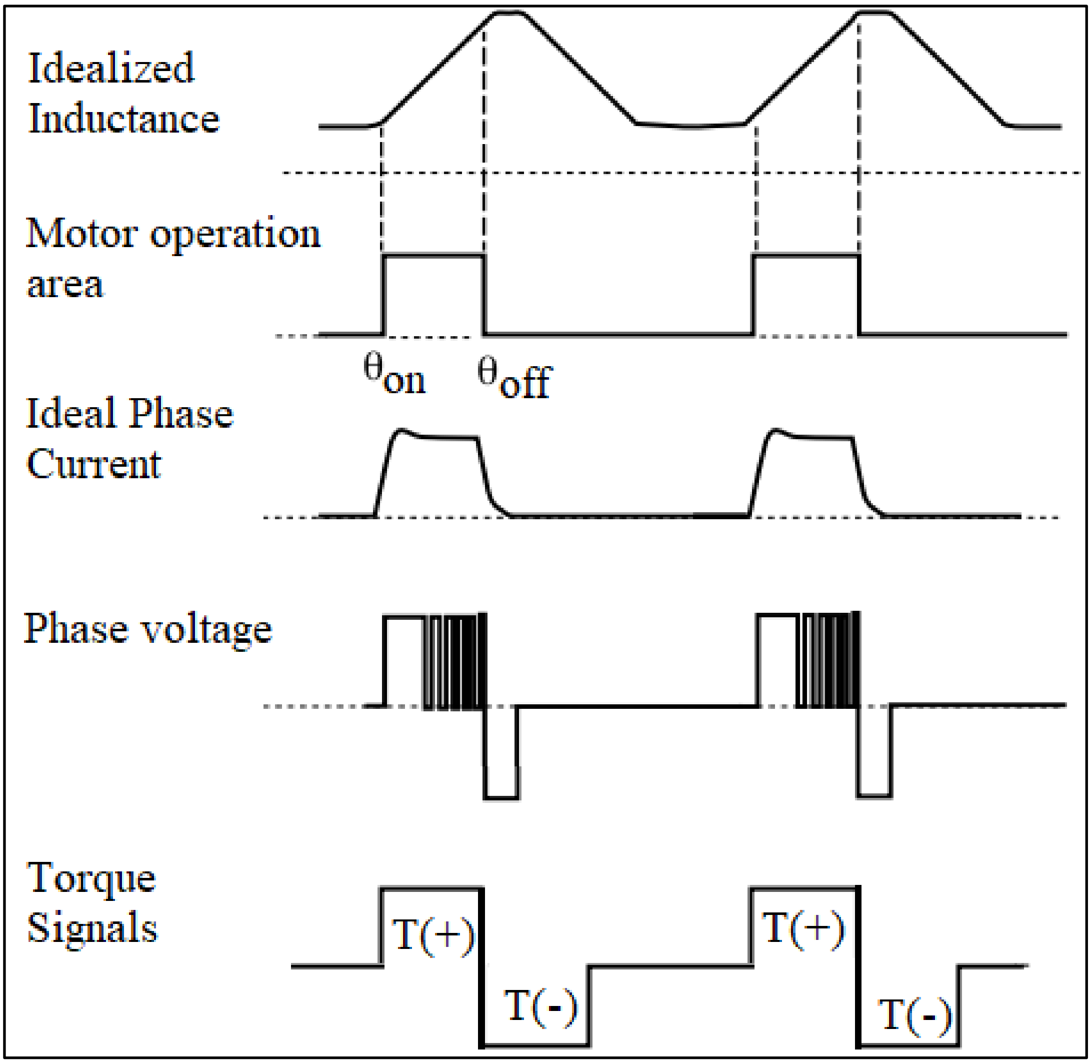

Figure 1.6. Inductance, current, voltage, and torque waveforms of SRM [8].

1.3. Problem Statement

SRM is generally modeled with lookup tables (LUT) or neural networks (NN) [11]. One LUT consists of torque T(i,θ) data, and the other LUT consists of the flux linkage λ(i,θ) data. Figure 1.7 and Figure 1.8 illustrates the torque waveform and flux waveform of three phase 6/8 ERSRM respectively.

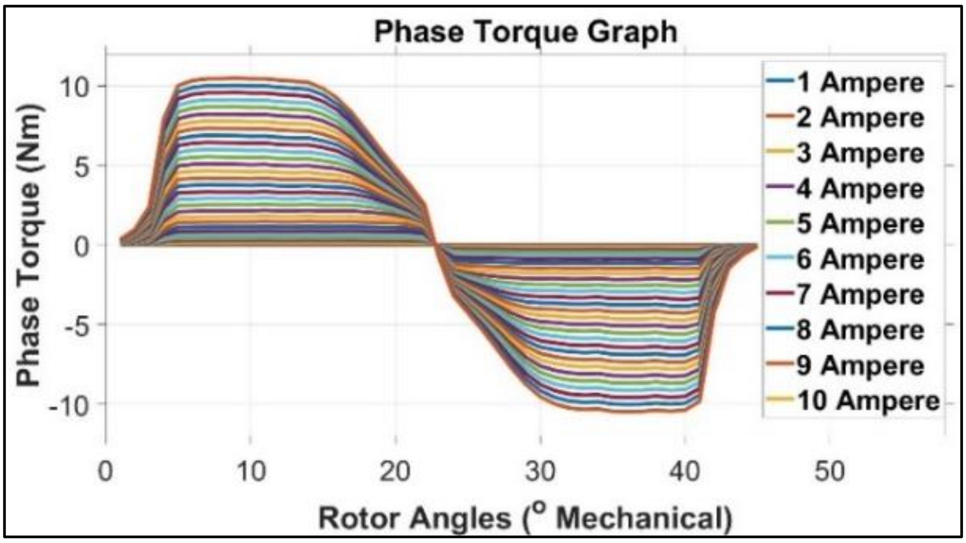

Figure 1.7. Phase torque graph of SRM

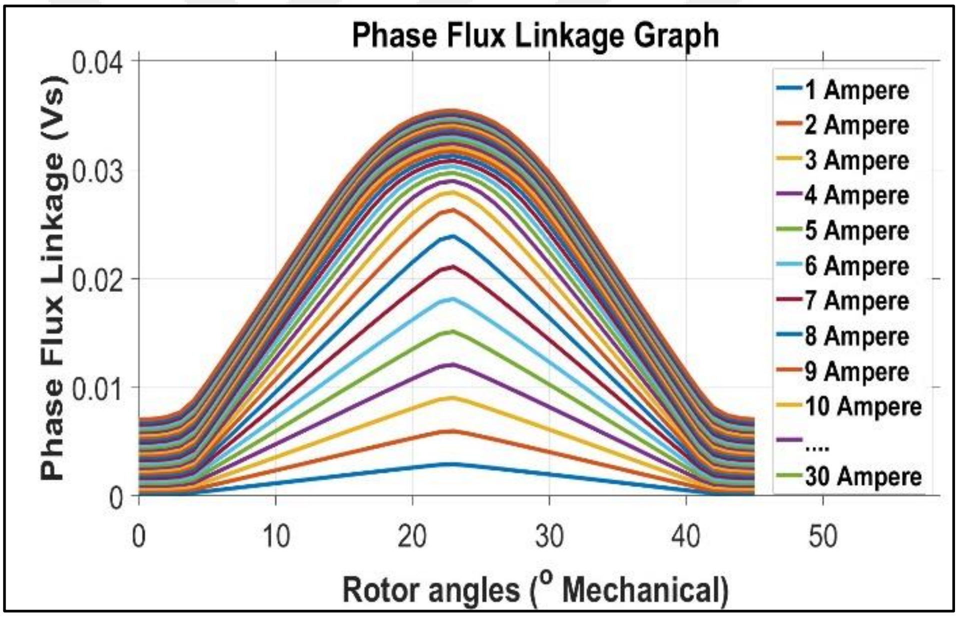

Figure 1.8. Flux linkage graph of SRM

The estimation of the phase flux linkage using the lookup tables technique requires rotor angular position (θ) information. This information could be gathered either using rotor position sensors or using estimation algorithms. The rotor position sensor overwhelms the cost advantage and reduces the reliability of the driver. The rotor position estimator requires prior knowledge of the motor's magnetic characteristics. Estimating SRM phase flux linkage accurately, and independent of rotor position information will contribute to the widespread usage of SRMs.

1.4. Hypothesis

It is possible to estimate SRM phase flux linkage in real-time, solely from phase current measurements using the ANN technique while eliminating the necessity of the rotor angle information.

Since the training dataset of the ANN is time-series data, the ANN structure is selected as a nonlinear autoregressive network with exogenous input (NARX) neural network (NN). "NARX NN can learn to predict one time series, from past values of the same time series as feedback input and another time series input called the external time series [12]".

1.5. Literature Review and State of The Art

1.5.1. SRM Flux Linkage Estimation Techniques

The torque generation of the switched reluctance motor (SRM) relies on its double-salient-pole structure. Since the magnetic flux lines prefer the lower reluctance path, this causes the rotor's angular rotation. In the last decades, SRMs have gained popularity with their robust and fault-tolerant structure and ease of production. The torque ripple and acoustic noise problems [13] were commonly solved by the development of advanced control techniques and the motor's geometrical improvements [14]. Consequently, the industrial usage of SRMs stands out, especially in aerospace and automotive traction motor applications, where the environmental conditions are compelling and fault tolerance is of high priority.

The magnetization characteristics of the SRM are required for drive system modelling. There are various techniques to obtain these characteristics such as the magnetic equivalent circuit method, finite element analysis (FEA) method, or by making measurements [15].

The accuracy of the magnetic equivalent circuit method [16, 17, 18, 19, 20] is lower compared to other methods due to the theoretical assumptions and simplifications made in this method [21].

More commonly, the FEA modelling technique is used in the literature for the extraction of the motor's magnetization characteristics [22, 23, 24, 25], however, the verification of the extracted data should be performed by making experimental measurements. The experimental verification process is time-consuming and might not be practical for motors operating on the factory floor [26].

The phase flux linkage measurement methods can be classified as direct or indirect measurements [27]. Magnetic sensors were employed in the direct flux linkage measurement method [28, 29, 30]. CoCu nanowires that expose a giant magnetoresistive (GMR) effect are used for the direct measurement technique proposed in [28]. The motor's FEA model was validated using the measurement data. In [31], the number of sensors was reduced and its effect on the torque computation accuracy was studied. The direct measurement technique using magnetic sensors requires additional development and cost-reducing improvements.

In the indirect measurement method, the flux linkage profile is calculated from the voltage equation using the voltage, phase current, and phase resistance measurements. This method was more commonly used in the literature [21, 26, 32, 33, 34]. In [35], the extraction of the flux-linkage profile from the static torque measurements was also specified as an indirect method. Additionally, it was mentioned that numerical integration of the voltage equation had yielded better results.

The phase flux linkage of an SRM was measured indirectly in [26] from the phase winding voltage and the phase current measurements with and without rotor locking devices. The authors expressed the disadvantage of using a rotor locking device as the requirement of an additional mechanical construction to lock the rotor at each angular position and the spent time to perform the measurements. However, it was highlighted that eliminating the rotor locking device for the flux linkage profile measurement brings the necessity of an appropriate driver with special software.

A rotor clamping device was used in [21] to measure the flux linkage so that the rotor was fixed at each angular position by the stepper motor. The voltage-balance method was used to calculate the flux-linkage profile.

The torque balance method (TBM) which was explained in [33, 34] is another method for extracting the SRM flux linkage profile. This method reduces the measurement effort, but the rotor position is still required for real-time flux linkage estimation.

An online phase resistance compensation was proposed in [32] to improve the accuracy of the flux-linkage estimation.

The data reconstruction method was proposed in [36] to obtain the flux linkage profile of SRM, excluding the extra mechanics and absolute position encoder. The torque balance method was used for flux linkage measurements and the flux linkage profile at each angular rotation was interpolated from the measured data.

The flux-linkage estimation model based on an artificial neural network (ANN) was proposed in [37]. The air gap magnetic field between the stator and translator was measured using a Hall effect sensor. The position and the phase current were used as inputs of an ANN which consists of two hidden layers. This ANN was used to estimate the flux linkage.

In this study, different from the state of the art, the phase flux linkage estimation was achieved using only the phase current as the input of the NARX NN. The SRM was initially operated in open loop control (OLC). The Simulink host-target communication was used to monitor and save the phase excitation signals and phase currents on the personal computer (PC). TI TMS320F28379D digital signal processor (DSP) was used as the embedded platform.

The measurement dataset was used to calculate the phase flux linkage values offline for each stator and rotor pole alignment. The training of the ANN was performed using the offline calculated flux linkage values and measured phase currents. Using this technique, the flux linkage of SRM was accurately estimated in real-time without the requirement of the prior calculation of the motor magnetic characteristics, which needs additional mechanical setup as discussed in [26].

The NN model developed in this Ph.D. thesis consists of two hidden layers. 26 neurons exist in the first hidden layer and 18 neurons exist in the second hidden layer. The methodology of the determination of the number of neurons was performing trials. It started from 10 neurons and increased by five for each trial. The number of neurons in the second layer was defined as 2/3 of those in the first layer plus one [38]. The tangent sigmoid transfer function was chosen as the activation function.

1.5.2. SRM Rotor Position Sensing Techniques

Three patents were found which were related to the rotor position sensing system that was developed in this Ph.D. thesis. The information about the patents was given as follows.

- **Record 1/3 KR1987206B1**

Title (English): Switched reluctance motor

Publication Date: 2019-06-11

Assignee - Original: NEW MOTECH CO. LTD.

• **Record 2/3 CN208401694U**

Title (English): A switched reluctance motor

Publication Date: 2019-01-18

Assignee - Original: Zhongshan Resun Intelligent Control System Co. Ltd.

• **Record 3/3 KR529938B1**

Title (English): Switched reluctance motor

Publication Date: 2005-11-22

Assignee - Original: LG Electronics Inc.

The WOS literature review about low-cost rotor position detection of SRM is as follows.

In [42], an inductive position sensor based on a variable reluctance structure was introduced. The high-frequency signal injection method was applied to detect the phase variable inductance depending on the rotor position. Similarly, the SRM configuration was used as a position sensor [43]. Again, the developers benefited from the unsaturated inductance. The high-frequency signal injection technique was applied to obtain the electromagnetic characteristic curves with respect to the rotor position. The voltage vector coordination transformation method was used to estimate the rotor position. In [44], the induction principle was used for linear SRM. The sensor output was a quadrature signal which could be used as an encoder input of a standard 3-phase motor driver. The technique combined a low-cost position sensor with a non-sinusoidal interpolation circuit for rotor position detection.

A built-in search coil was studied in [45]. The rotor position was detected from the back emf of the search coil which occurs during rotation. The rotor's initial position was detected with 2 degrees of mechanical angular error rate using the Squared Euclidean distance method.

In [46], only one Hall sensor was used with an optimized slotted disk. The rotor's initial position was detected by analyzing the phase current peaks. In [47], the starting procedure of an inner runner three phases 6/4 SRM was explained using a magnetic ring and only one Hall sensor.

One of the drawbacks of using Hall sensors in such an application could be the misaligned position sensors. In [48], this problem was studied for the SRM drive system which had three Hall sensors for position detection. The dynamic time-wrapping algorithm was proposed as a solution to this problem. Another SRM drive application using a Hall sensor for rotor position detection with a movable conduction angle control strategy was explained in [49]. In [50], a Hall sensor-based rotor position detection method was proposed for the inner runner SRM application. The permanent magnets were placed inside each rotor pole and the spaces between the rotor poles. Three unipolar Hall sensors were placed at 120 degrees intervals to detect the permanent magnets.

The optical sensor is an alternative to the Hall sensor approach. In [51, 52, 53, 54, 55] optical sensor solutions were explained.

1.6. Novelty and Originality

1.6.1. Novelty in Flux Linkage Estimation of ERSRM

In the classical methodology of online phase flux linkage calculation of SRM, a flux linkage lookup table is used. One of the inputs of this lookup table is rotor angle and the other is phase currents. In this research, a novel phase flux linkage estimation algorithm using artificial neural networks (ANN) was developed. The phase flux linkage estimation was performed with the developed ANN model, solely from the phase current values without using the rotor angular position information.

The NARX NN teaching dataset was formed from the measured phase currents and phase excitation signals during the machine operation. These signals were obtained using the Simulink host-target serial communication interface between the PC and the embedded platform.

The measurement data was used to calculate the phase flux linkage values offline for each period of the phase current signals. The phase current signals and the offline calculated flux linkage values formed the training dataset. The ANN was trained using this training dataset. The trained NN model accurately estimated the phase flux linkage in real time without the requirement of extracting the magnetic characteristics of the SRM using an additional mechanical setup as it was discussed in [26].

The developed NN model consists of one input, two hidden layers, and one output layer. There were 26 neurons in the first hidden layer and 18 neurons in the second hidden layer. The neuron numbers were selected by performing trials. It started from 10 neurons and in every trial increased by five until it reached the least estimation error.

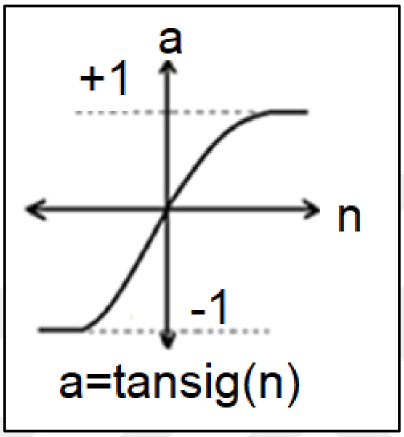

Figure 1.9. The tangent sigmoid transfer function

The number of neurons in the second layer was chosen as the two third of the number of neurons in the first hidden layer and added by one more neuron as formulated in [38]. The tangent sigmoid transfer function was the activation function as shown in Figure 1.9. The a = tansig (n) Matlab command takes a matrix of net input vectors M and returns the P-by-S matrix, A, of the elements of M compressed into (-1 1) [39]. This method yielded adequate results, which were explained in subtitle 2.4.3.

1.6.2. Originality of the Rotor Position Sensing Technique for ERSRM

With the rotor position sensing system developed throughout the Ph.D. thesis work, the SRM could be operated and this made real-time phase voltage and current measurements possible.

Figure 1.10 shows the Hall sensor system laboratory prototype. Using the Hall sensors' output signals, the phase switching signals were generated and the motor was operated. The Hall sensors' placement on the plate is shown in Figure 1.11. This plate was mounted on the flange surface. Numbers 1 to 6 were the Hall sensors. Numbers 7 to 10 were the screw Halls. Number 11 is the +Vdc line, number 12 is the ground (GND) line for the sensors' voltage supply. Number 13 is the plate; 14, and 15 are the voltage supplies lines. The signal cables were passing through the channel which was numbered 16.

In Figure 1.12, the magnets' places were shown and numbered from 18 to 24. One magnet was placed inside the holes that were drilled on the rotor enclosure aligned with each rotor pole. In Figure 1.13, the pictures of the Hall effect sensors and the magnets were shown. The input voltage range of each Hall effect sensor was 4.5 - 5 VDC. The operation temperature was - 40 to +80 ^{0}C. When one magnet aligns with one Hall sensor, the sensor signal output changes from a high level (supplied voltage level) to a low level (below +1 V), and this analog signal is converted to 0 and 1 digital outputs by the microcontroller. The stator phase excitation signals are generated according to the sensor signal outputs.

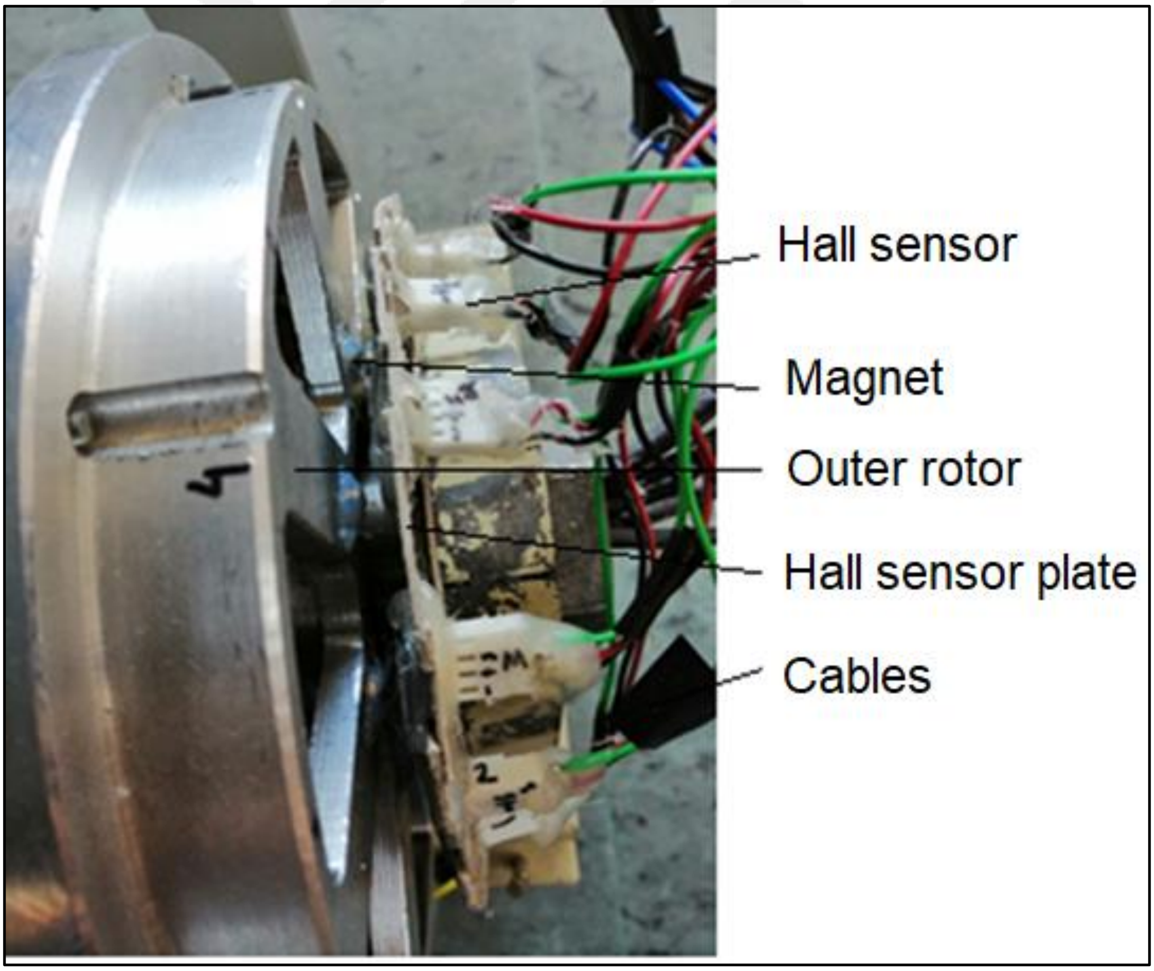

Figure 1.10. Hall sensor system

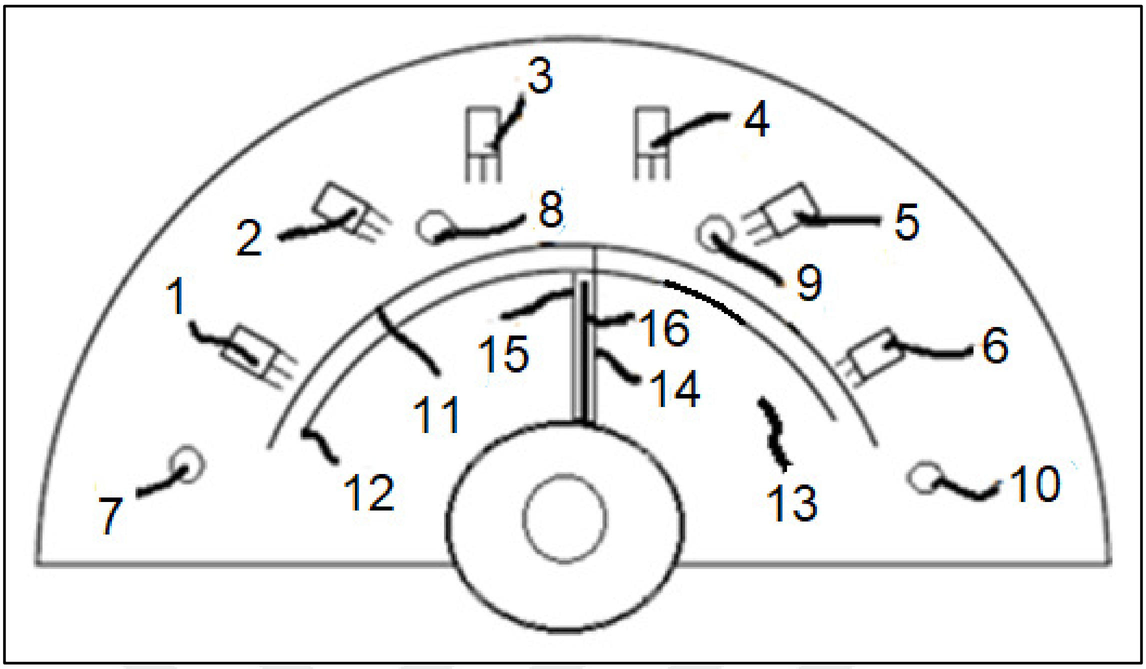

Figure 1.11. Hall sensor placement with numbers

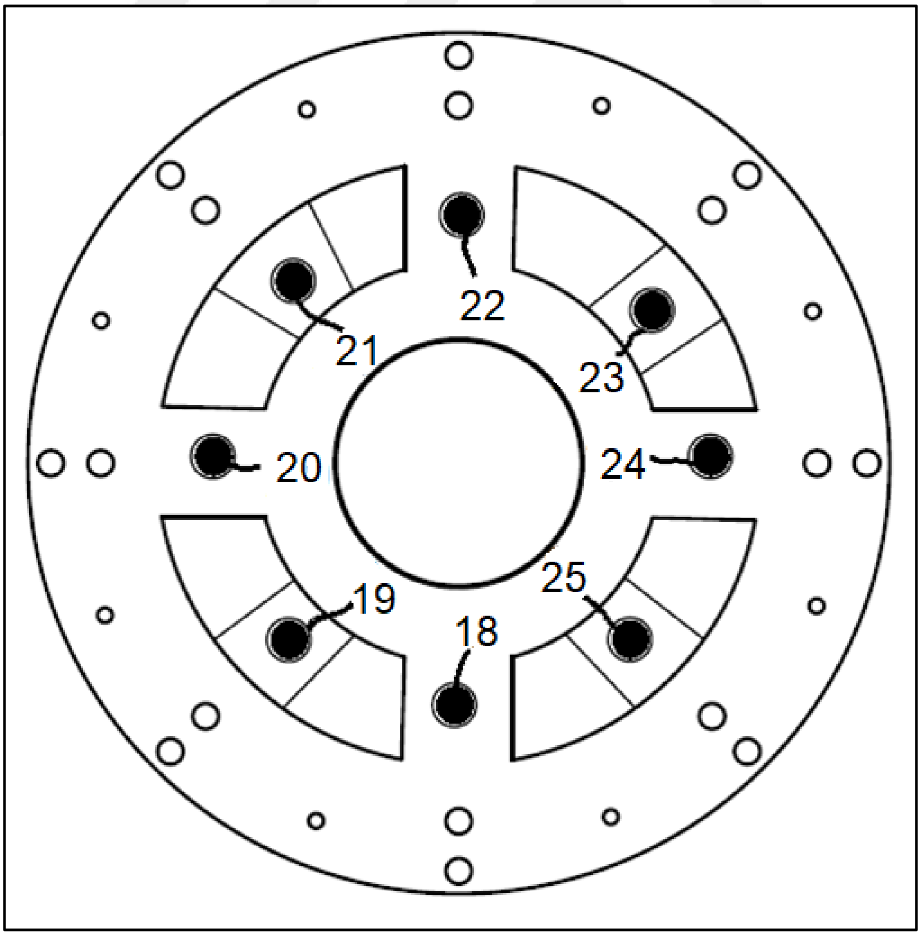

Figure 1.12. Magnets placements with numbers

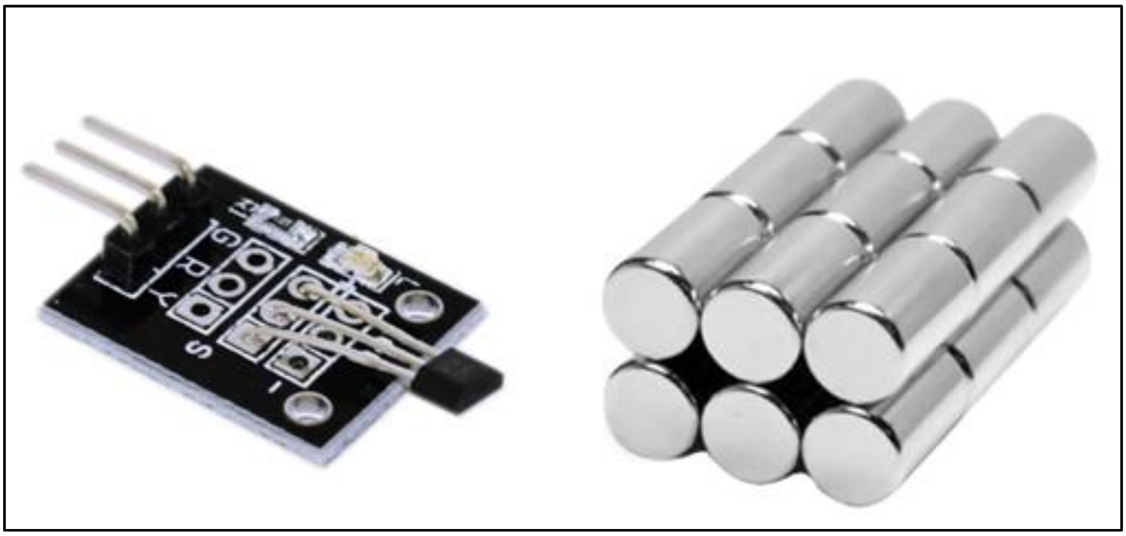

Figure 1.13. Hall sensor and cylindrical magnets

The phase switching order was defined by the Hall effect sensor outputs. First, during prototyping, for each sensor output change, the alignment or unalignment condition was observed from the slots shown in Figure 1.14. Then Table 1.1 was formed. In real-time operation, the controller selected the phase-switching signals from the table.

Table 1.1. Sensor outputs and phase-switching signals

Sensor numbers and outputs						Phase Switching Signals
1th	2th	3th	4th	5th	6th	
1	1	0	0	0	0	100
1	0	1	1	0	0	100
0	1	1	0	0	0	100
0	1	0	1	0	0	110
0	1	1	1	0	0	110
0	0	1	1	0	0	010
0	0	1	0	1	0	010
0	0	1	1	1	0	010
0	0	0	1	1	0	011
1	0	1	0	0	0	011
0	0	0	0	1	1	001
0	0	0	1	1	1	001
0	1	1	0	0	0	001
1	0	0	0	0	1	101

Figure 1.14. The slots on the outer enclosure of the motor prototype.

2. WORKS DONE

2.1. Construction of 6/8 ERSRM Motor and The Test Bench

2.1.1. Motor Coil Winding and Stator-Rotor Assembling

The coil windings were 3x1 mm^2 copper wires with 40 turns each. In Figure 2.1 the coils wounded on the stator were shown. The outer rotor enclosure was constructed from aluminum as shown in Figure 2.2. The outer body has a slotted structure for natural cooling.

Figure 2.1. SRM stator with coils

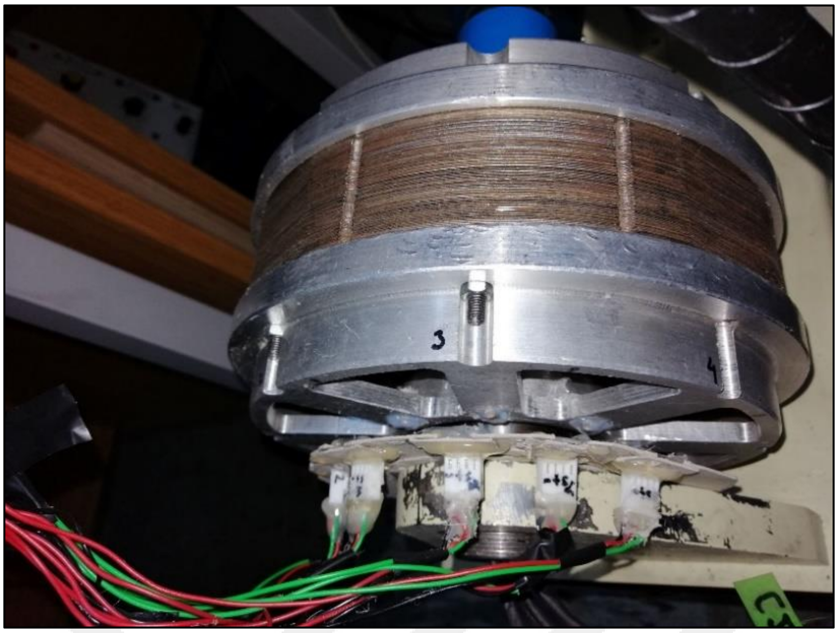

Figure 2.2. SRM stator-rotor assembled view

2.1.2. SRM Driver

The BTS7960B driver shown in Figure 2.3 formed one leg of the asymmetrical half-bridge drive system in Figure 2.4. The driver operates at 24 VDC and the maximum current rate is 42 Amperes.

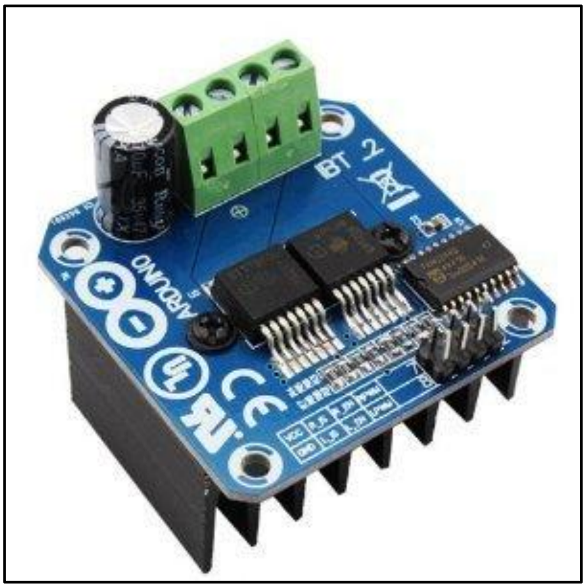

Figure 2.3. BTS7960B driver

Figure 2.4. Three BTS7960B drivers for three-phase ERSM

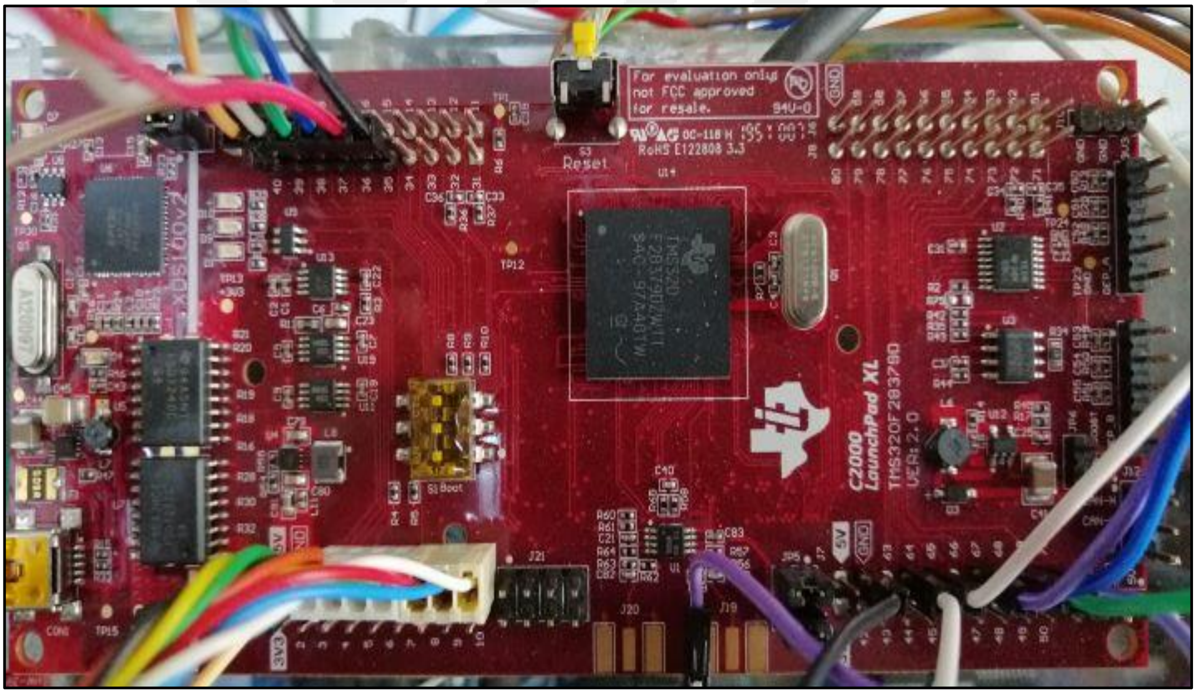

Figure 2.5. TI TMS320F28379D Launchpad

The developed phase flux linkage estimation algorithm was embedded on TI TMS320F28379D DSP shown in Figure 2.5.

2.2. Modelling of 6/8 ERSRM

2.2.1. Simulink Model

The SRM drive system model was realized in Simulink and shown in Figure 2.6. The converter subsystem block is shown in Figure 2.7. Each stator phase was modelled as a varying inductor connected in series with a varying resistor. The MOSFET switches and the gate drivers were used from the library. The resistor and inductor values were calculated offline using measured phase currents and voltages and stored in look-up tables. The SRM was modelled using flux linkage and torque lookup tables. The table data was obtained by making FEA. The FEA process was explained in the following subsection.

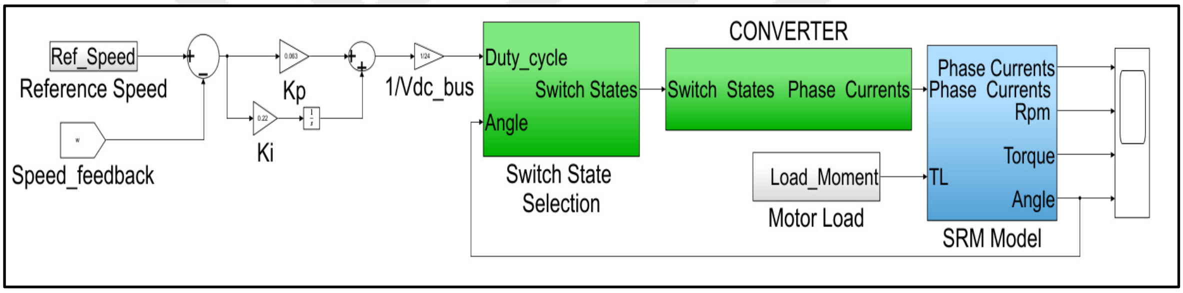

Figure 2.6. Simulink model complete view

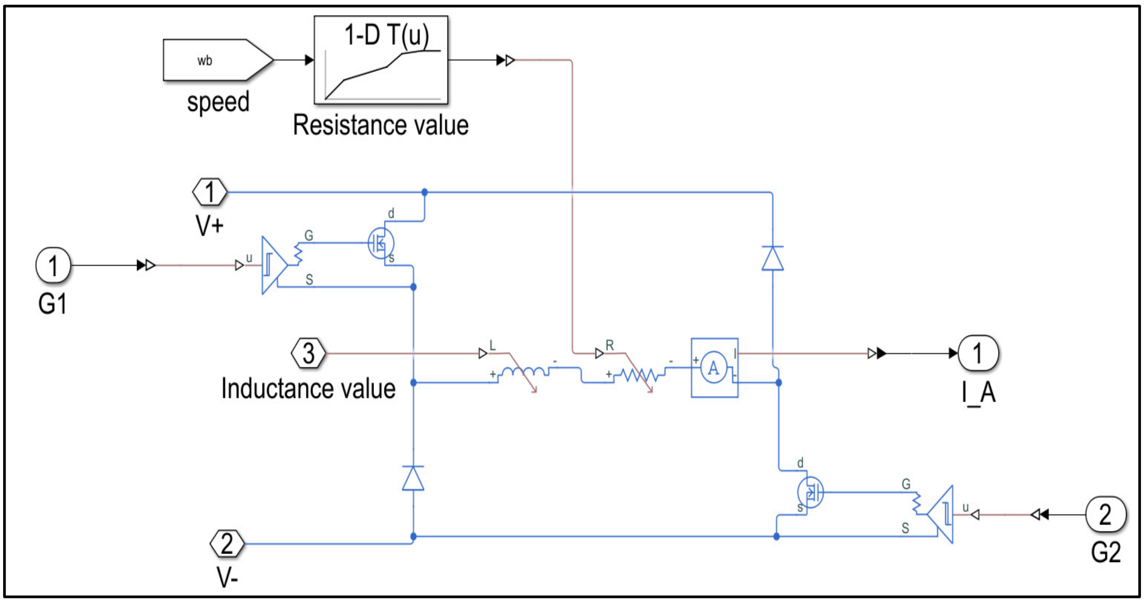

Figure 2.7. Converter model in Simulink

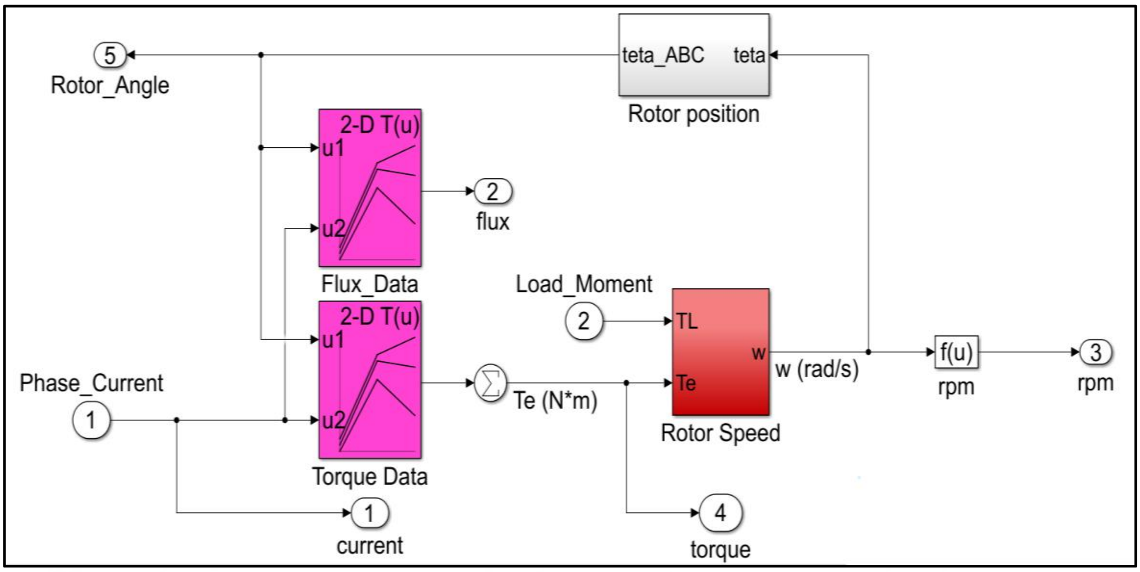

Figure 2.8. Switched reluctance motor model in Simulink

2.2.2. The Finite Element Analysis

The FEA was made with the Finite Element Method Magnetics (FEMM) software. The half-rotor FEMM image of the ERSRM model is shown in Figure 2.9. The program output showing magnetic flux lines and magnetic flux density plot were shown in Figure 2.10. The model was realized as a half rotor to speed up the simulation. Phase currents were changed from 1 Ampere to 50 Amperes and the rotor angle was changed from 0 to 45 mechanical degrees using the Luna Script Matlab code below to calculate the moment and flux values in each iteration. The torque LUT data as written in Attachment Table 8.1 – Table 8.5 and the flux LUT data as written in Attachment Table 8.6 - Table 8.10 were obtained from FEMM analysis.

The LUNA Script Matlab Code extracts torque and flux data of the ERSRM and is shared below.

```
addpath(genpath('D:\femm42'))
savepath D:\femm42\mathfemm\pathdef.m
cd D:\femm42
n1=45;
dtta1=1;
deg1=pi/180;
tq1=zeros(n1*dtta1,50);
```

```
fq1=zeros(n1*dtta1,50);
co_energy=zeros(n1*dtta1,50);
```

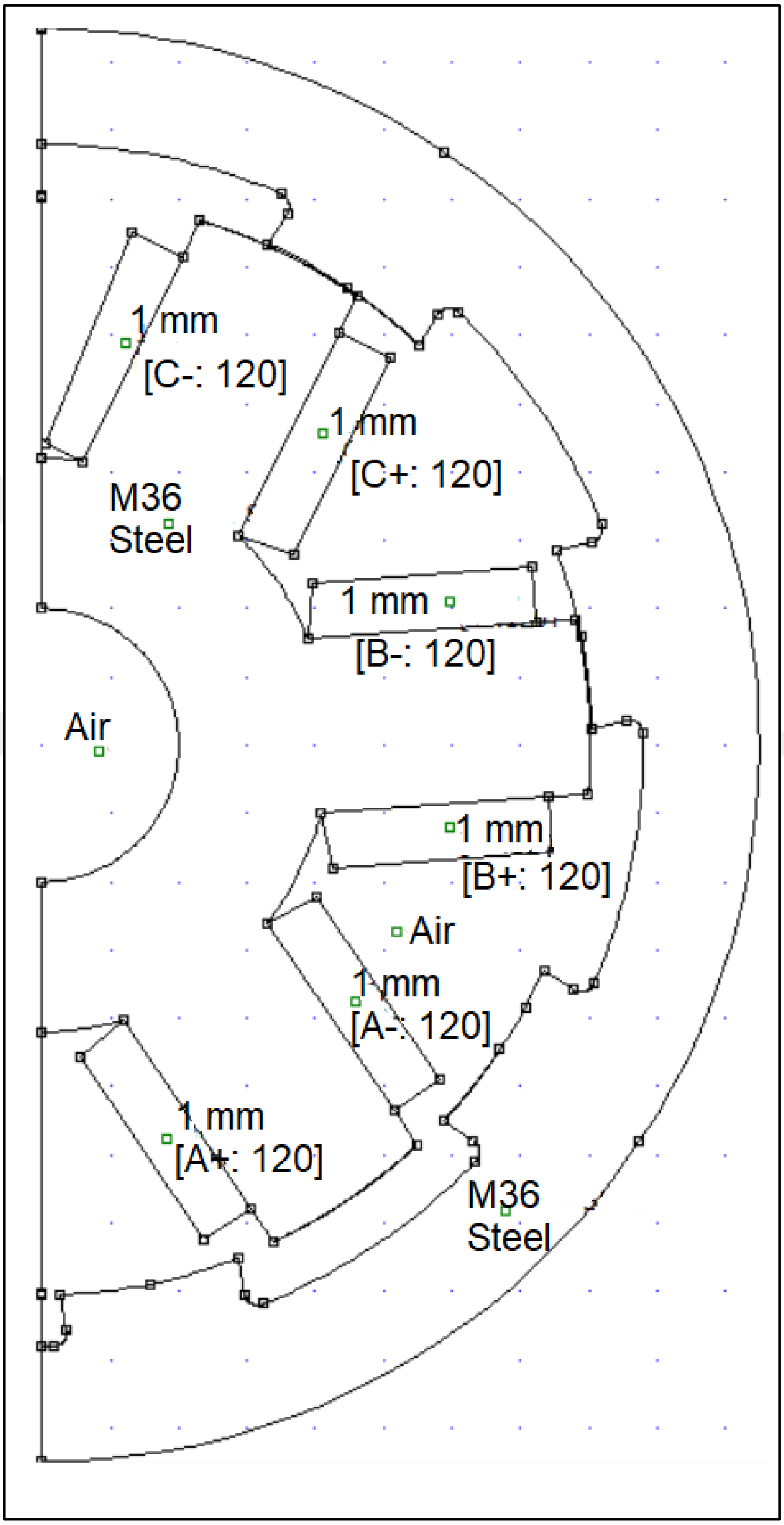

Figure 2.9. The image of half rotor ERSRM Model in FEMM

```
inductance=zeros(n1*dtta1,50);
mag_energy=zeros(n1*dtta1,50);
q1=[];
r3=80.25;
r4=80.125;
r5=80.5;
openfemm;
for m=1:50
    iphase1=m
    for k1=1:n1
     tta1=k1*dtta1;
     opendocument('half_rotor_0.25mm_Air_gap_v4.fem');
     a1=1;b1=0;c1=0;
   mi_modifycircprop('A+',1,a1*iphase1);
   mi_modifycircprop('B+',1,b1*iphase1);
   mi_modifycircprop('C+',1,c1*iphase1);
   mi_modifycircprop('A-',1,-1*a1*iphase1);
   mi_modifycircprop('B-',1,-1*b1*iphase1);
   mi_modifycircprop('C-',1,-1*c1*iphase1);
   mi_selectgroup(1);
   mi_moverotate(0,0,tta1);
   mi_addarc(0,r3,-r5*sin(tta1*deg1),r5*cos(tta1*deg1),tta1,1);
   mi_addarc(0,-r3,r5*sin(tta1*deg1),-r5*cos(tta1*deg1),tta1,1);
   mi_selectarcsegment(-r4*sin(tta1*deg1/2),r4*cos(tta1*deg1/2));
   mi_selectarcsegment(r4*sin(tta1*deg1/2),-r4*cos(tta1*deg1/2));
   mi_setarcsegmentprop(1,'apbc3',0,0);
   mi_clearselected;
   mi_saveas('temp.fem');
   mi_analyze(1);
   mi_loadsolution();
   mi_showmesh();
   mo_groupselectblock(1);
   ti=mo_blockintegral(22);
   area = mo_blockintegral(5);
   energy=mo_blockintegral(2);
   coenergy=mo_blockintegral(17);
   tq1(tta1,m)=2*ti;
   mo_clearblock();
   mo_addcontour(12.03,-40.24);mo_addcontour(32.9221,-26.0793);
   B=mo_lineintegral(0);
   fq1(tta1,m)=(B(1,2))*area;
   mo_close;
   mi_close;
   end

end
closefemm;
```

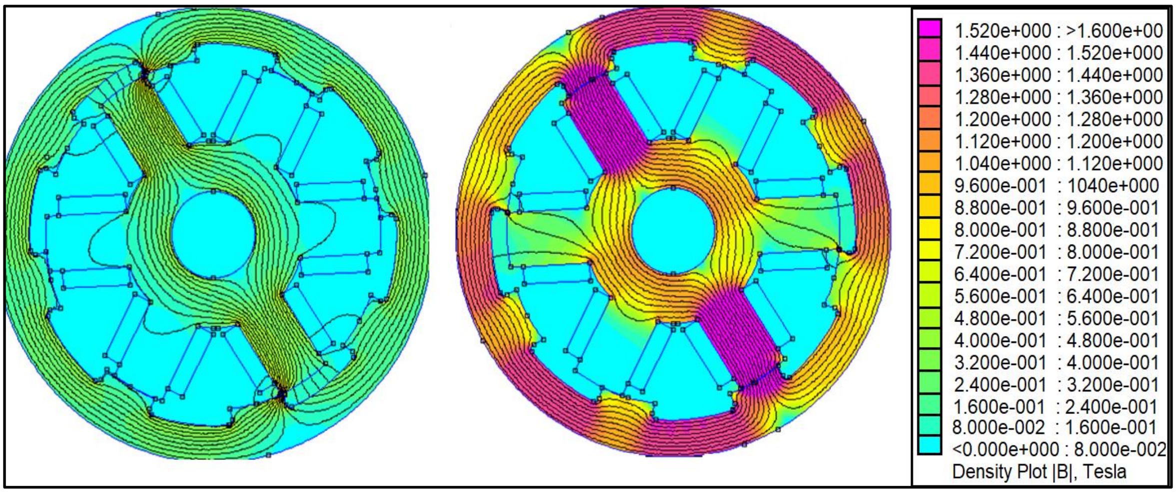

Figure 2.10. FEMM electromagnetic analysis during rotor-stator unalignment (left) and alignment (right) at 30 Ampere coil current

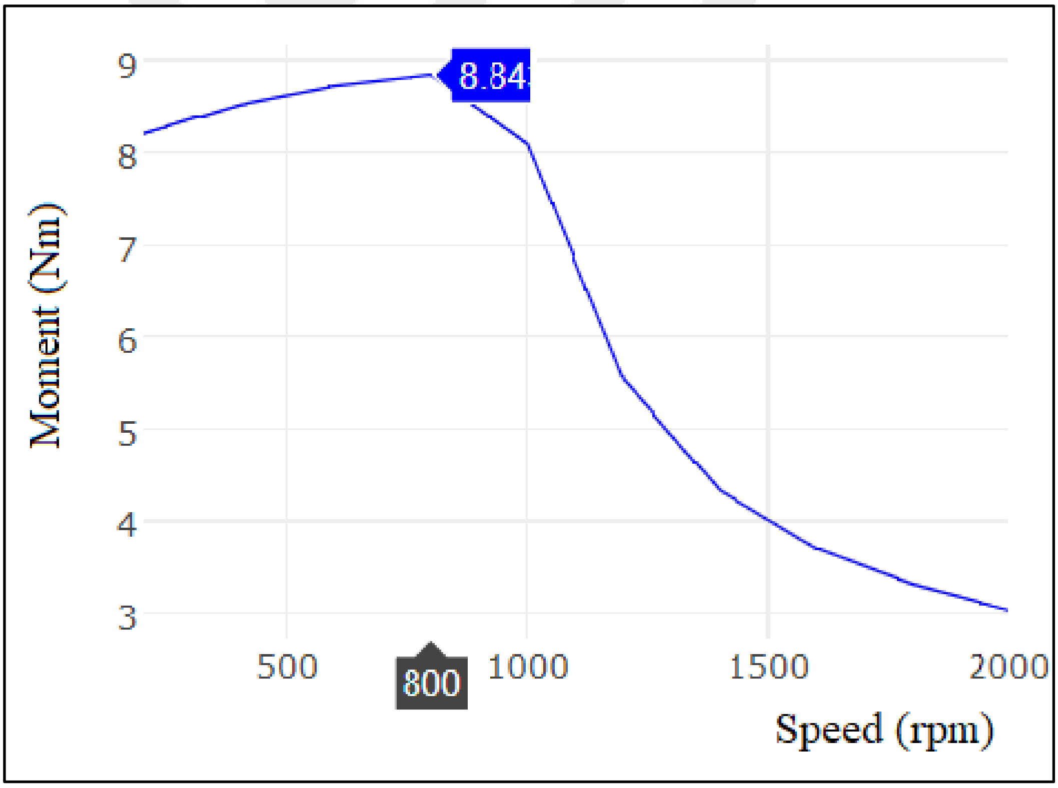

Figure 2.11. Motor moment-speed graph

The motor was also simulated in JMAG software. The moment-speed graph calculated by the JMAG software is given in Figure 2.11.

2.3. ERSRM and Motor Test Unit

2.3.1. Motor Test Unit

The motor control hardware is given in Figure 2.12. The motor testbench consists of ERSRM, couplings, a moment sensor, and the motor loading unit shown in Figure 2.13.

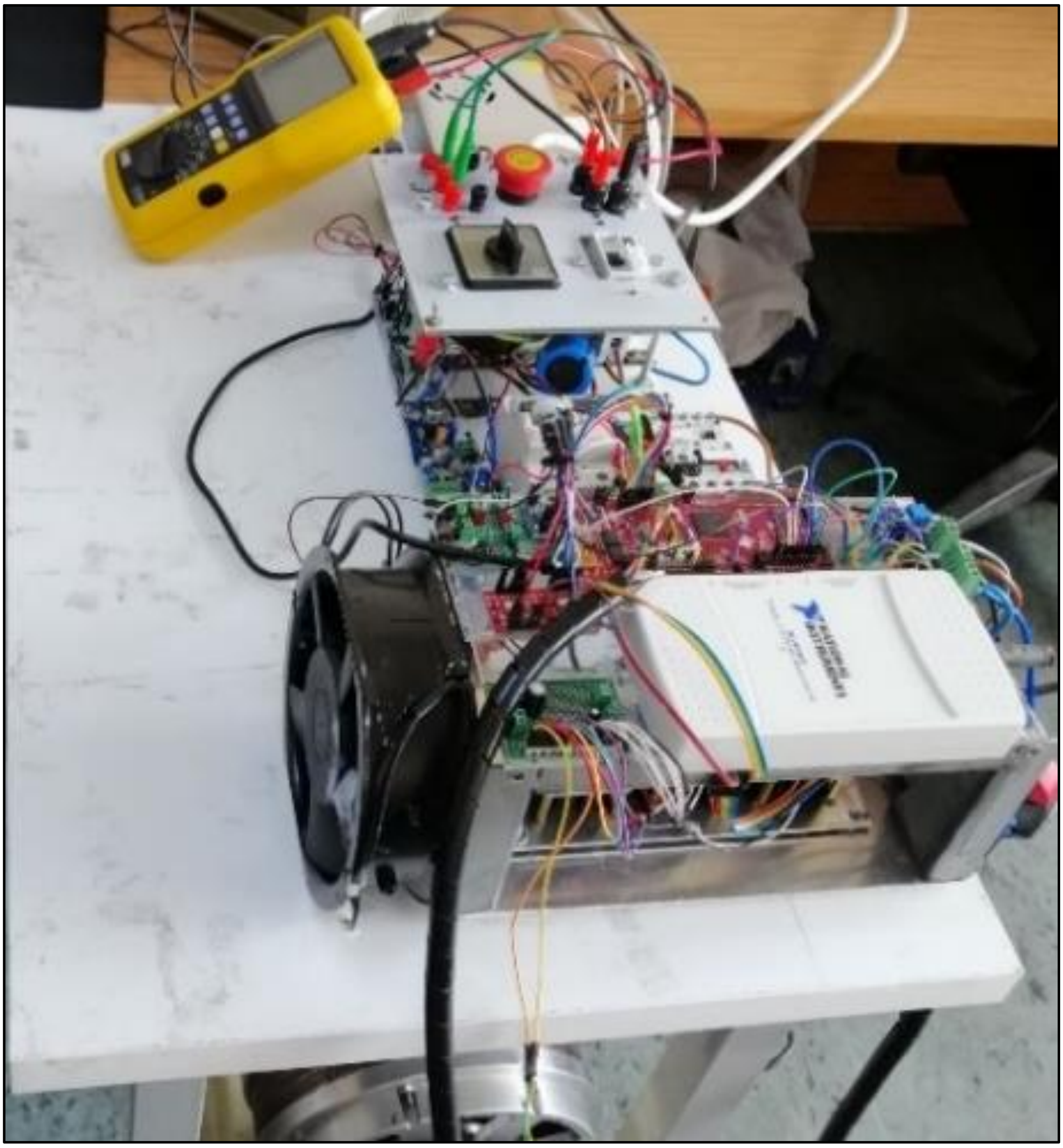

Figure 2.12. The motor control hardware

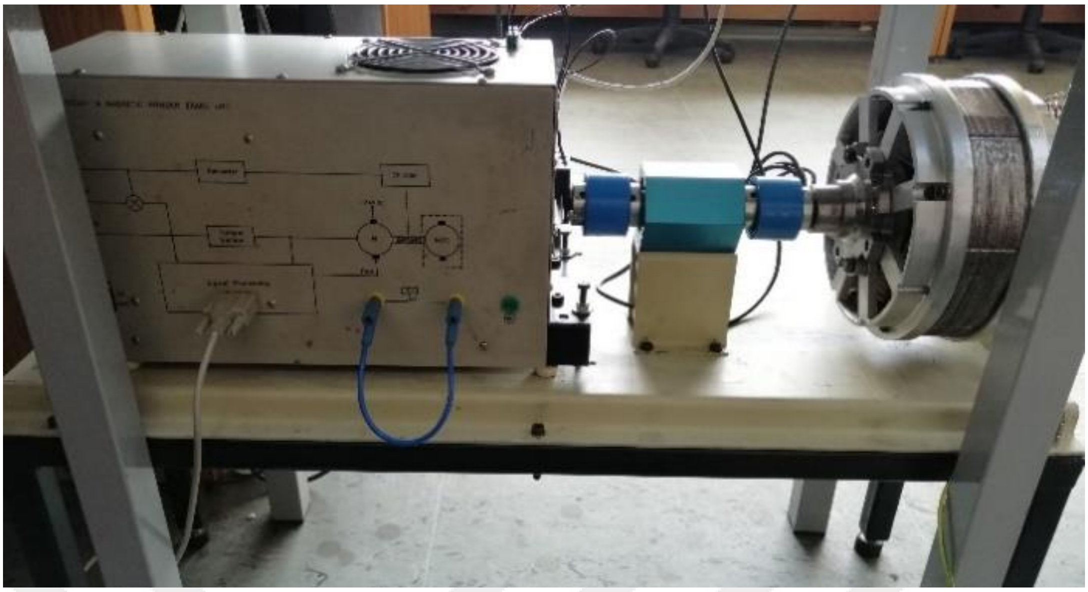

Figure 2.13. Outer runner SRM test unit

2.3.2. Materials List

In Figure 2.14, the torque sensor used on the test bench is shown. The moment sensor was DRBK-20-N rotary torque sensor. The data acquisition card in Figure 2.15 was used as an interface between the moment sensor and the computer.

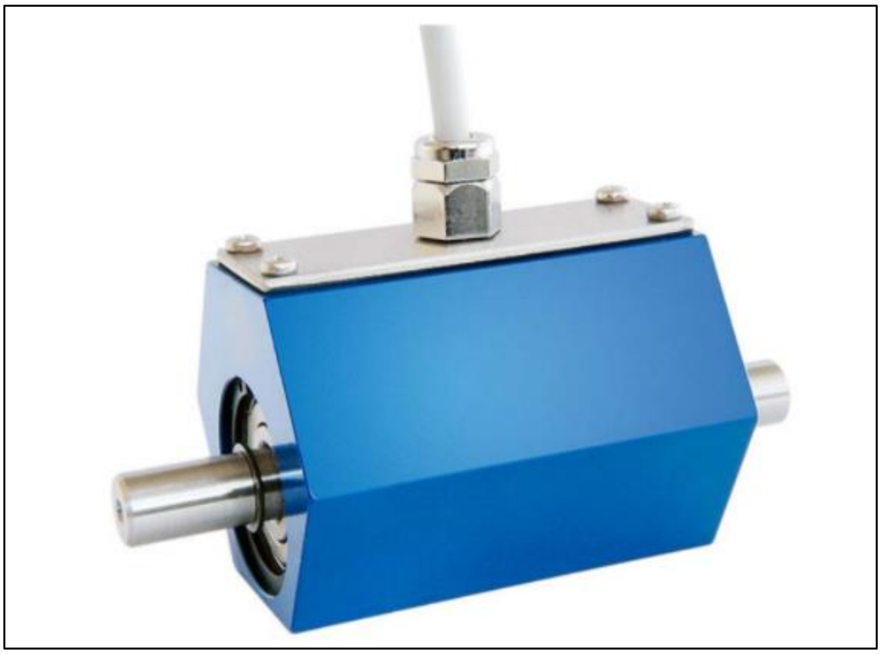

Figure 2.14. DRBK-20-N rotary torque sensor

Figure 2.15. NI USB 6211 DAQ Card

2.4. NARX Neural Network for Flux Linkage Estimation

Neural networks yield good results and accuracy in the modelling and parameter estimation of nonlinear dynamic systems [40].

The input of the developed NARX NN-based estimation block is the normalized phase current value while the output is the normalized value of the flux linkage. One input of the NARX NN model is the instantaneous current value and the second input is the two samples delayed output signal which is the flux linkage value. The developed model estimates the phase flux linkage in real time without using the rotor position information and the phase resistance variations do not need to be taken into account.

2.4.1. The NARX Neural Network

NARX neural networks can be taught to estimate dynamic system parameters, using the previous values of the same time series data as the feedback input, and another time series data called the external (or exogenous) time series data as the second input [12].

The network training was performed in an open loop. The network model is shown in Figure 2.16. After training the network, it was converted to the closed loop form and tested with the test dataset. The closed-loop structure of the network was illustrated in Figure 2.17.

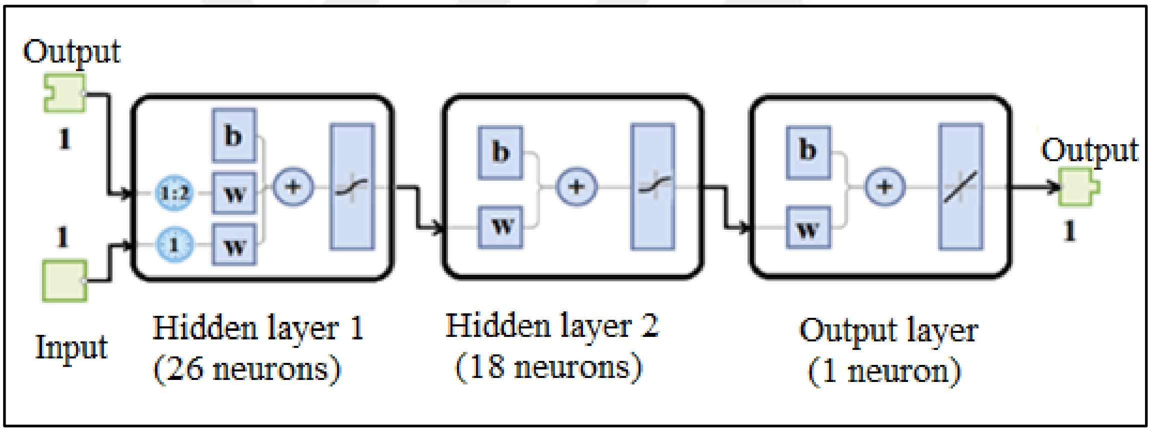

Figure 2.16. NARX NN training model

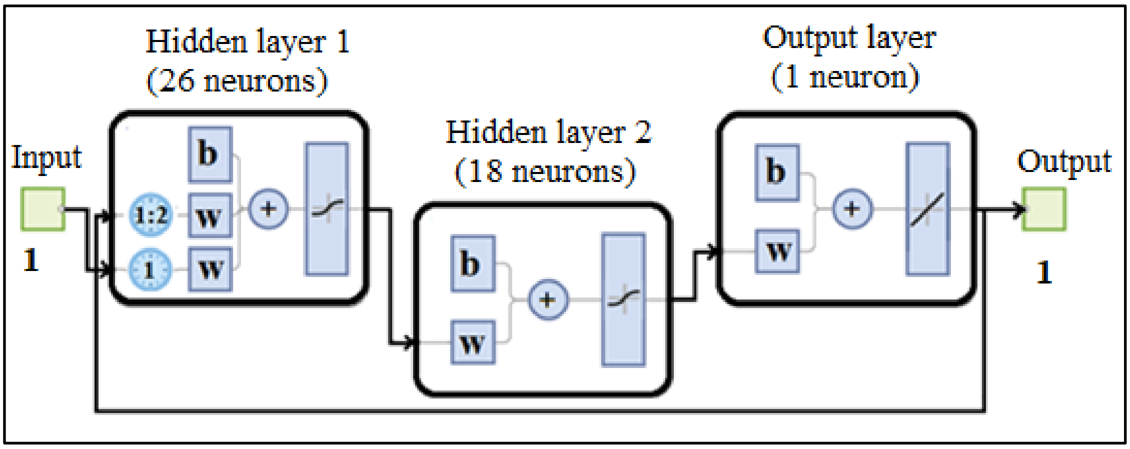

Figure 2.17. NARX NN testing model

2.4.2. The Preparation of the Training Data

The Simulink host target serial communication interface which was shown in Figure 2.18 was used to save the phase current values and the phase excitation signals into the Matlab workspace. From the phase excitation signals and the DC bus voltage, the phase voltages were calculated for each phase current period. During the measurement period, the driver bus voltage was 24 Volt DC.

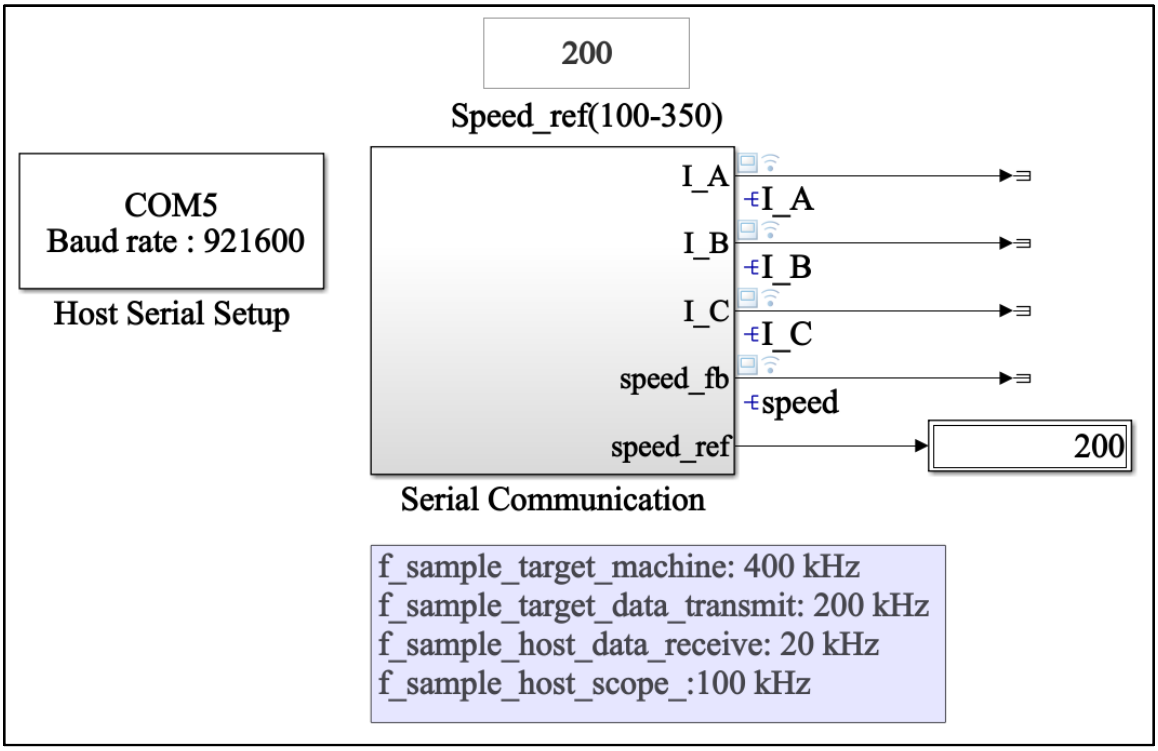

Figure 2.18. Simulink host interface

The Hall sensors' outputs were used to energize the correct stator phase. The reference speed was changed from the "Speed_ref" box shown in Figure 2.18. The voltage, current and speed values were stored in the Simulink workspace and used for the teaching data of the ANN-based phase flux linkage estimation algorithm. The host serial setup block was set to COM5 port, and the Baud rate was 921600 bps. The DSP sampling rate was 400 kHz. The data was transmitted from TI TMS320F28379D Launchpad with a 200 kHz sampling rate and the host machine read the data with a 20 kHz sampling rate.

For each phase current period, the related flux linkage values were calculated offline from (2.1) using the measurement data.

$$\lambda_k(t) = \int_0^t [U_k(t) - R_k i_k(t)] \tag{2.1}$$

The neural network training data was prepared in two steps. In the primary step, the measurements were taken for the start-up status and the dataset was created. An overshoot in phase current occurred during start-up as usual which was nearly 42 A, this was also the highest current capability that the motor driver was able to withstand. This part of the training process was performed to introduce the maximum value of the phase current to the NN which might occur during operation.

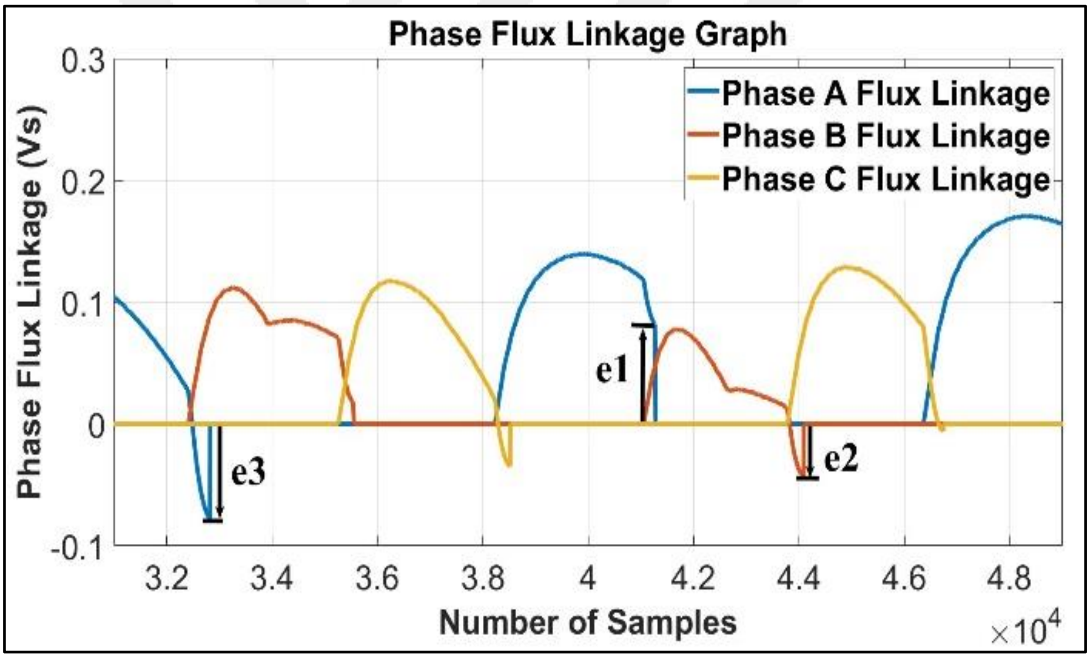

Figure 2.19. The flux linkage values in detail

As shown in Figure 2.19 flux linkage calculation errors occurred while making the online calculation using (2.1).

The phase flux linkage value was supposed to be zero at the end of each period. However, it did not happen due to the varying phase resistance. For each signal period, the flux linkage calculation errors were captured as e1, e2, and e3 in Figure 2.19, and used in (2.2) to determine the phase resistance variation.

The actual phase resistance values were calculated by adding the corresponding R_{error} value to the coils' initial resistance values which were calculated according to (2.3). Using the actual phase resistance values, the offline calculated phase flux linkage values were updated and the errors were compensated.

$$R_{error} = \frac{\lambda_{ph\_error}}{\int_{t_{on}}^{T} i_{ph} dt} \tag{2.2}$$

$$R_f = \frac{\int_0^{T_0} v_f(t)dt}{\int_0^{T_0} i_f(t)dt} \tag{2.3}$$

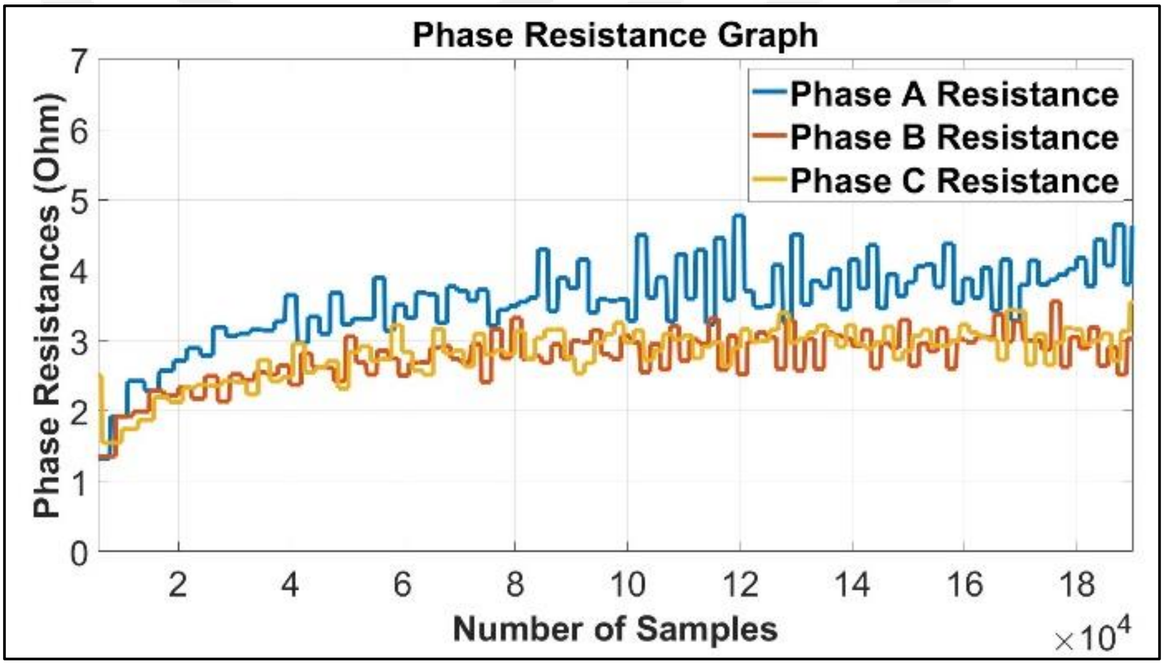

Figure 2.20. The resistance values of each coil

The varying phase resistances of each coil are drawn in Figure 2.20. The resistance of the phase coils' started from their initial value and varied depending on the coil temperature levels.

In Figure 2.21, the compensated and offline calculated flux linkage signals are shown in a detailed view. The phase-current and rotor speed graphs are given in Figure 2.22 and Figure 2.23 respectively.

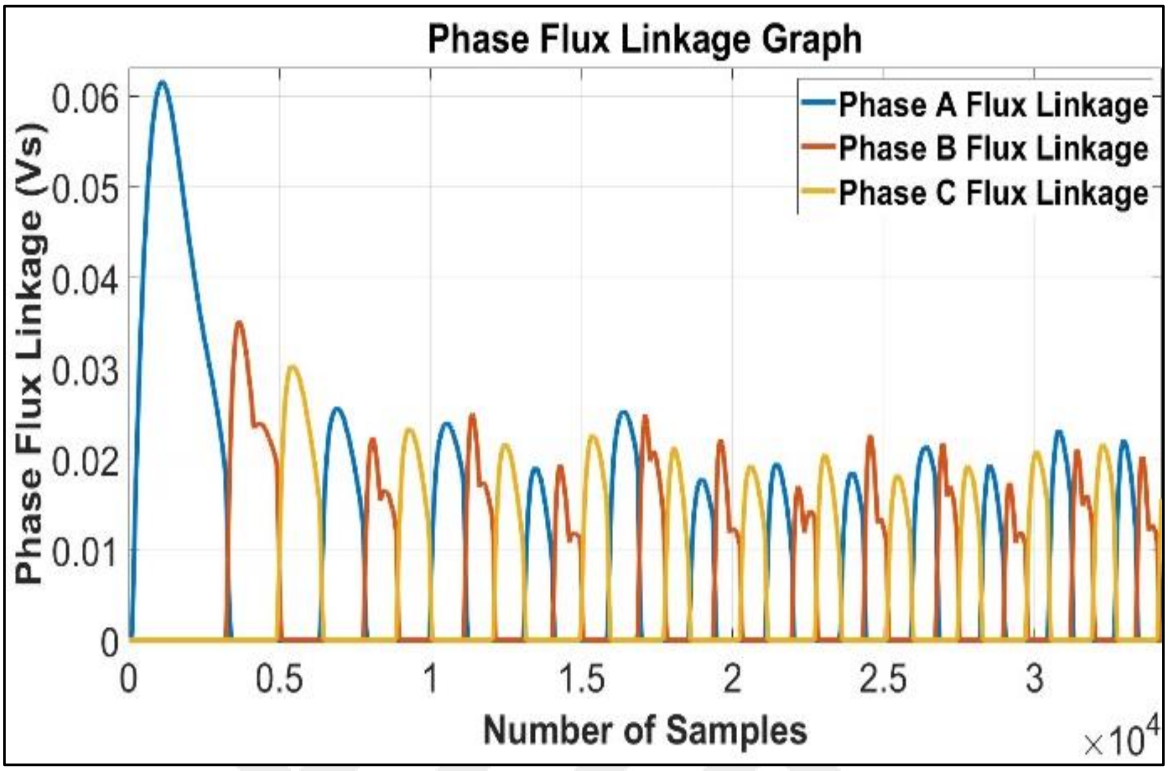

Figure 2.21. Flux linkage values using compensated phase resistances

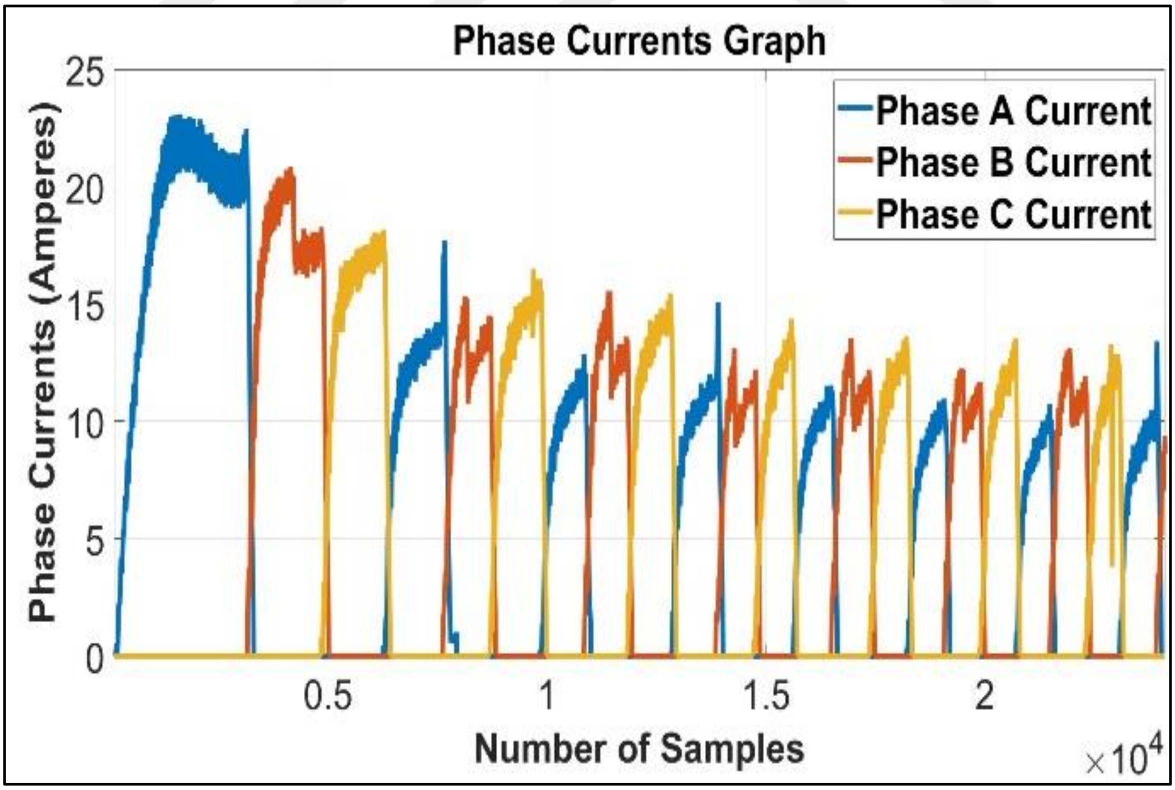

Figure 2.22. Stator-phase currents graph

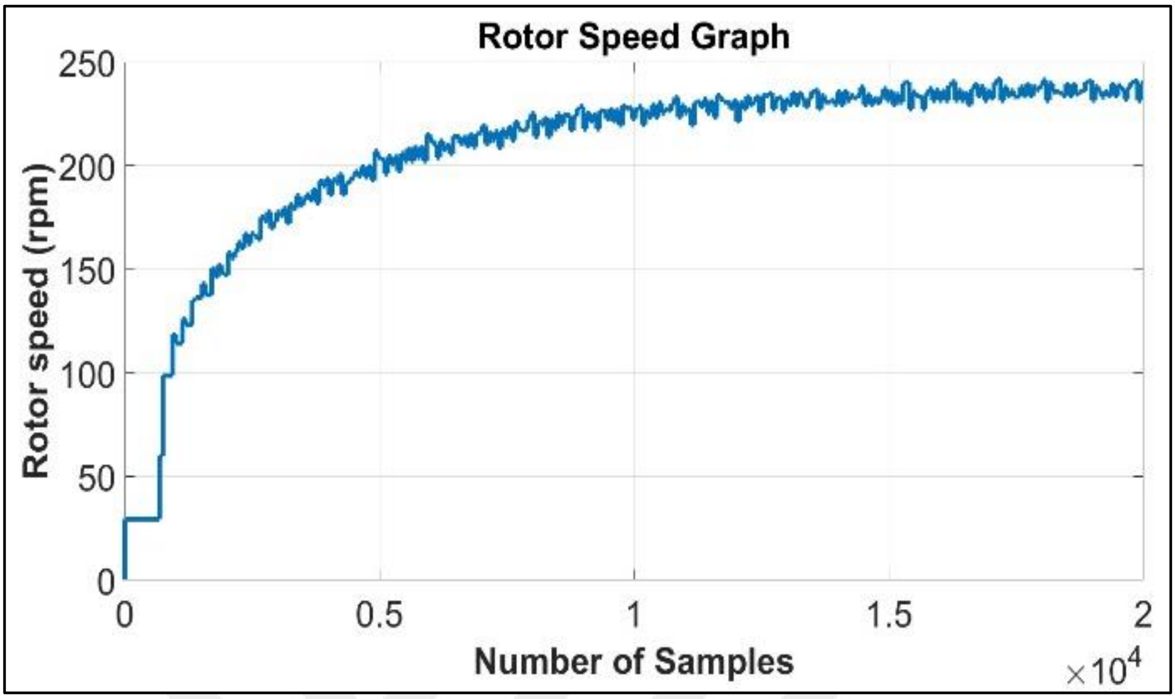

Figure 2.23. Rotor speed graph

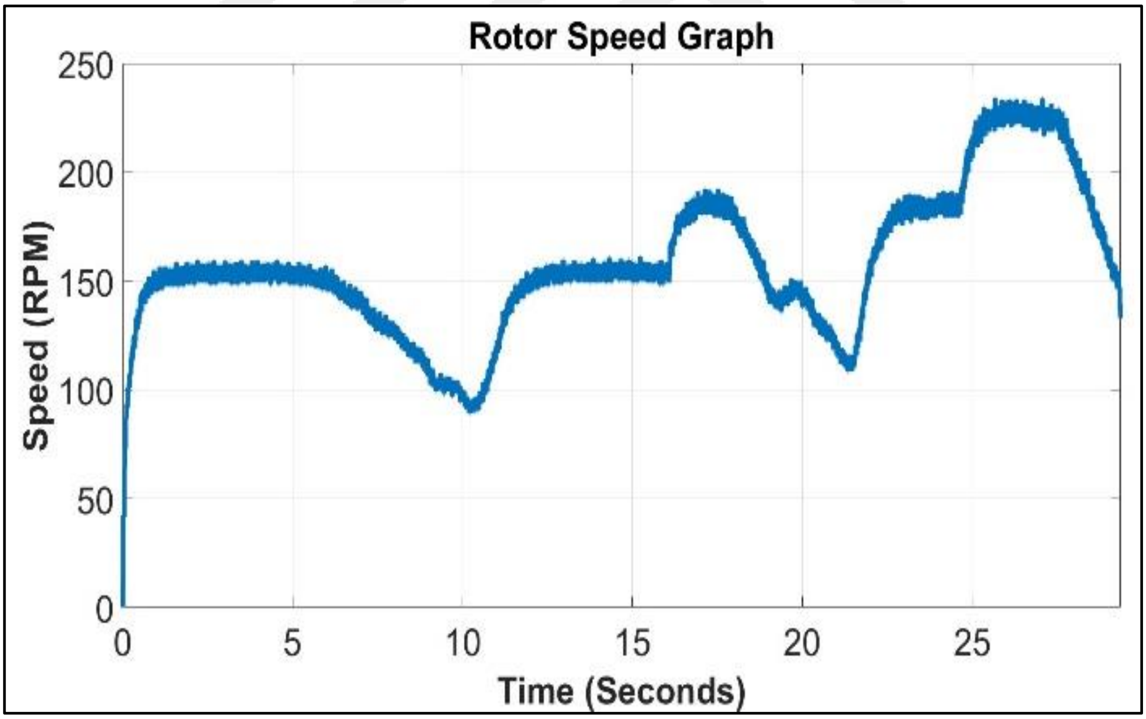

Figure 2.24. Rotor speed graph under different load moments

In the second step of preparing the training dataset, the motor was loaded with increasing order and operated at different rotor speeds while taking measurements. Figure

2.24 shows the rotor speed. The application of the load to the motor resulted in decreased rotor speed and increased phase currents. This part of the dataset was constructed to ensure the ANN was trained with more current and flux linkage data to make better predictions of the flux linkage under a variety of operating conditions. The dataset obtained in the two steps was merged and normalized for training the NN. The results of the NARX NN training process were explained in the following section.

2.4.3. The Results of NARX NN Training

Training the NARX NN yielded satisfactory results with small estimation errors. In Figure 2.25 targets, outputs, and errors of the training process are shown. The estimation error rates during the test process for each signal period were well under 0.05 which satisfies the accuracy requirements while the peak target values vary between 0.1 and 0.2. Decreasing the estimation error is also possible but this would cause an overfitting problem which is an unwanted situation in ANN. The best validation performance graph is shown in Fig. 2.26. It can be interpreted from the graph that the mean squared error is 0.0013294 at the 38th iteration.

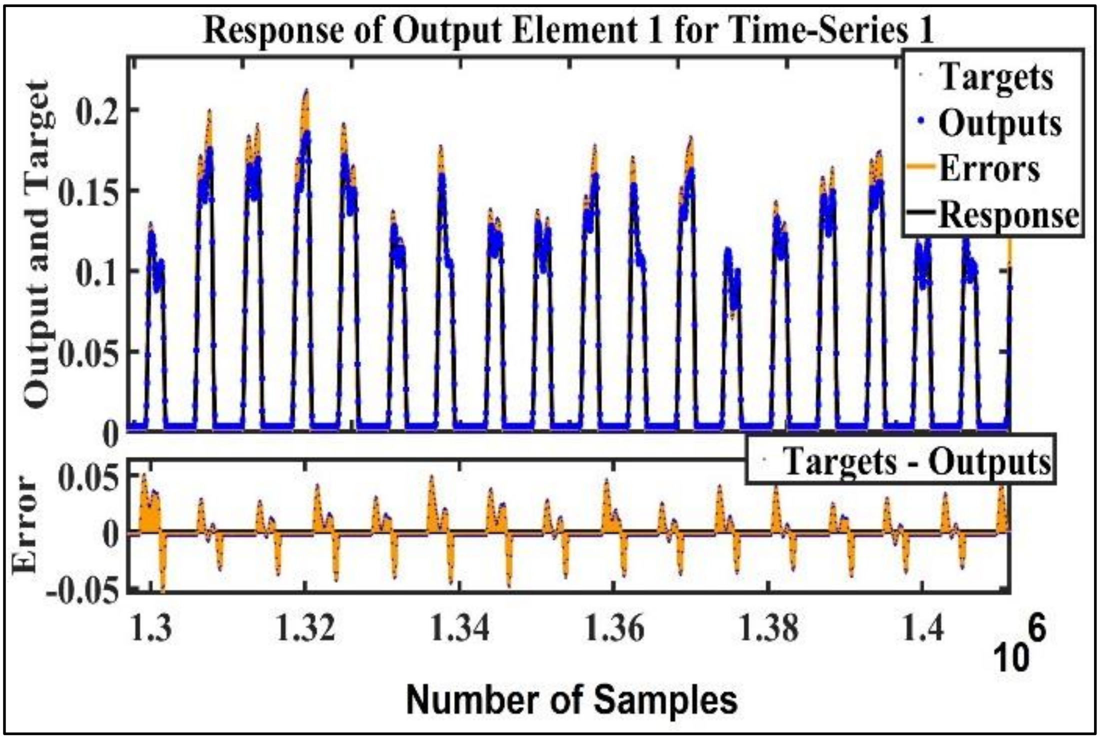

Figure 2.25. Response of output element for time series

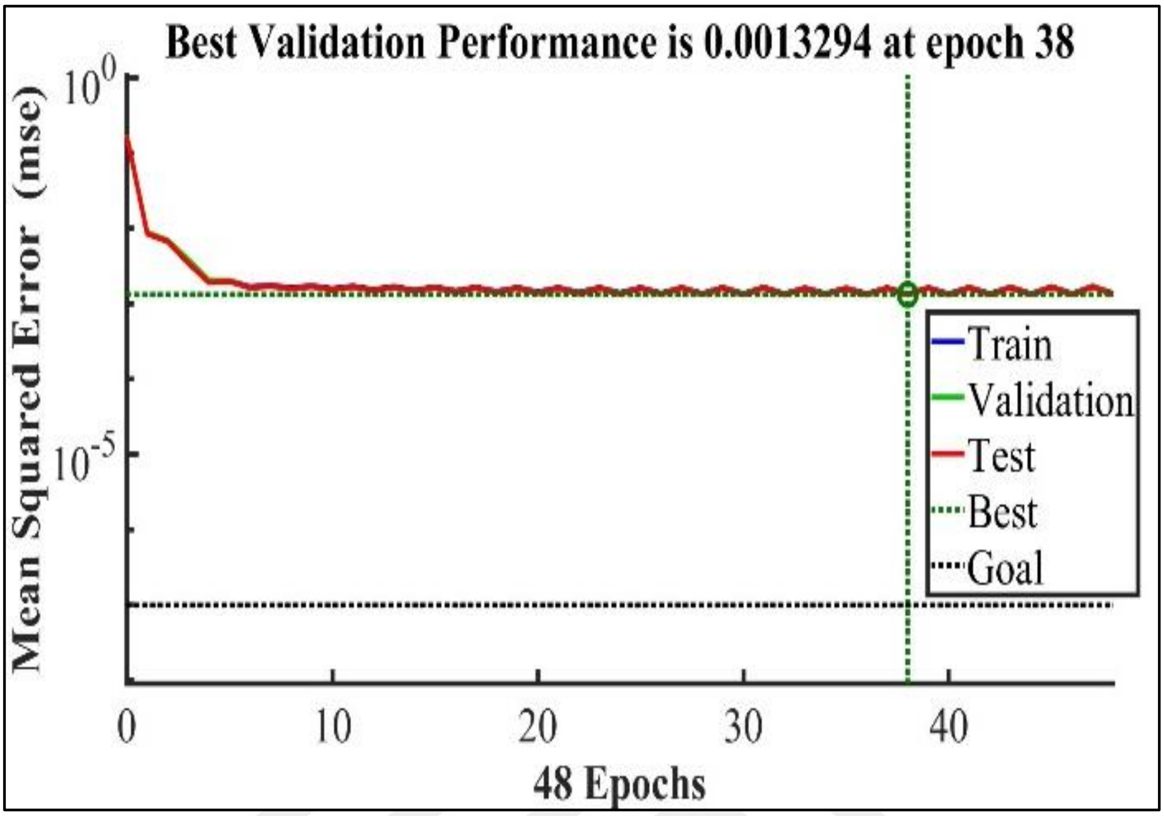

Figure 2.26. Mean squared error graph

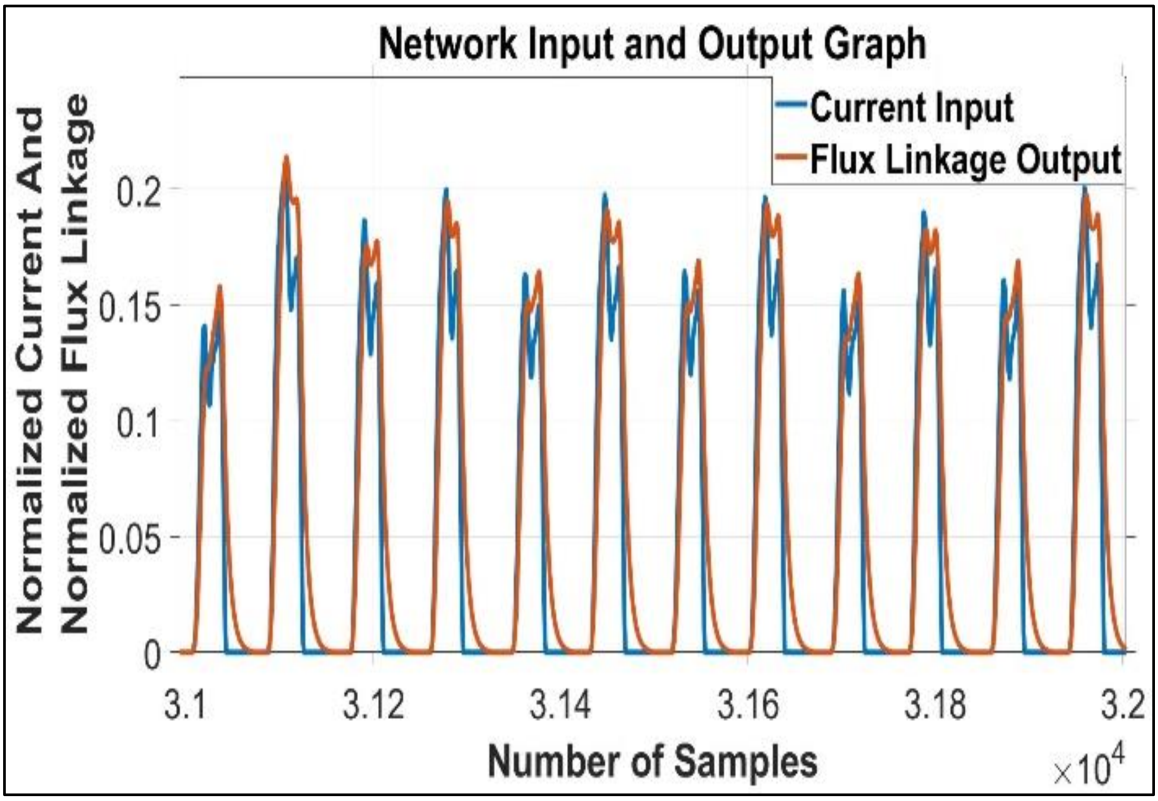

Figure 2.27. Network input and output graph

In the final stage, the trained network was tested with a different dataset then the estimation performance was evaluated. A small part of the input test data and network output was given in Figure 2.27. The estimated values overlapped the target dataset. The estimation error was between -0.0055 and 0.0038 while the output varied between 0 and 0.25. The results showed that the network output, accurately followed the input signal, and the estimation technique was validated. From these results, NARX NN is interpreted as a valid tool for parameter estimation such as phase-flux linkage of SRM using only the phase currents as the network input.

2.4.4. Embedded Code Generation For NARX NN

The NN to Simulink block conversion was achieved with Matlab coding. In real-time operation, the network input and output are required to be denormalized according to (2.4) and (2.5) to give the actual flux linkage values and this was done before generating the Simulink block. In which "I" is the phase current, and the symbol of "λ" is the phase flux linkage.

The Matlab command "closeloop(net)" was used to convert the network into its closed loop type before obtaining the Simulink block. The Simulink block representation of the developed neural network is shown in Figure 2.28.

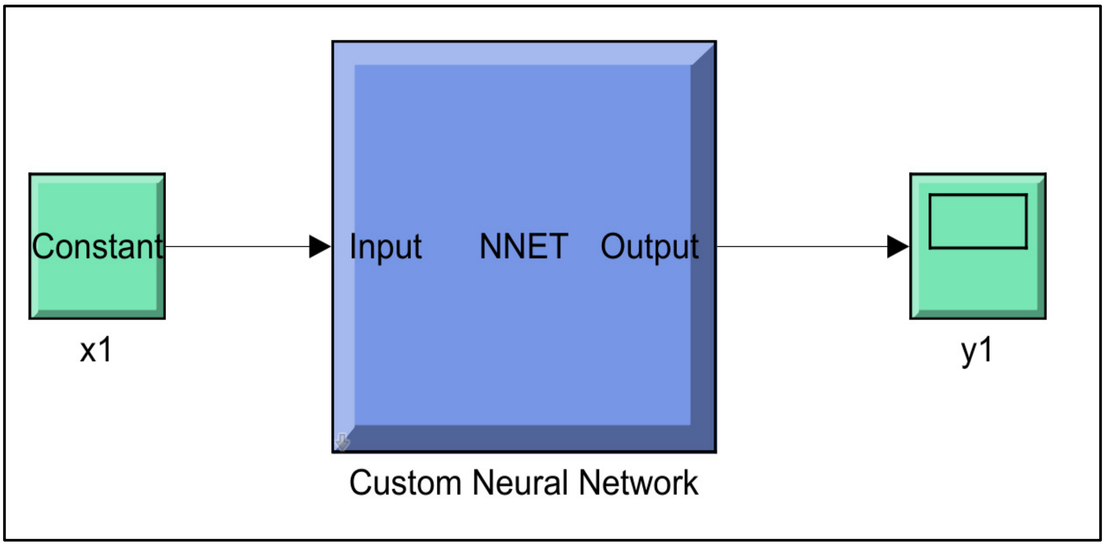

Figure 2.28. Simulink block of the developed network

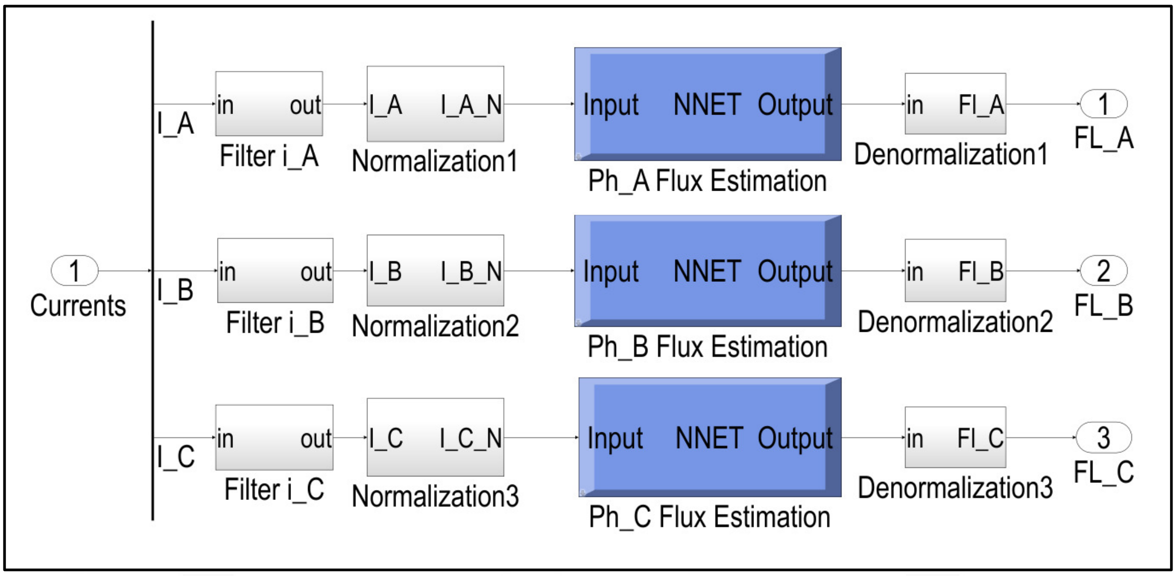

Figure 2.29. The Simulink view of the phase flux linkage estimation blocks for each of the stator phases

$$I_n(t) = \frac{I(t)}{\max\,(I(t))} \tag{2.4}$$

$$\lambda(t) = \frac{\lambda(t)}{\max\,(\lambda(t))} \tag{2.5}$$

In Figure 2.29, the Simulink blocks representation of the developed system was given. These blocks were converted to embedded codes using the Matlab Embedded Code Generation Tool for C2000 controllers.

2.4.5. Estimating Flux Linkage with Lookup Tables Approach

For estimating the flux linkage, the state-of-the-art mainly relies on the lookup table-based techniques. The developed technique in this thesis was analyzed comparatively with the LUT technique and the LUT data was generated with FEA realized with the FEMM software. In Figure 2.30, the LUT block is shown. The phase flux linkage waveform calculated from FEMM is given in Figure 2.31. The coil current varied between 1 to 50 Amperes and for each current level, the rotor rotated from 0 to 45 mechanical degrees. 3x1 mm2 copper wires with 40 turns were used as the phase coil. The analyzed motor structure had the geometric parameters described in [41].

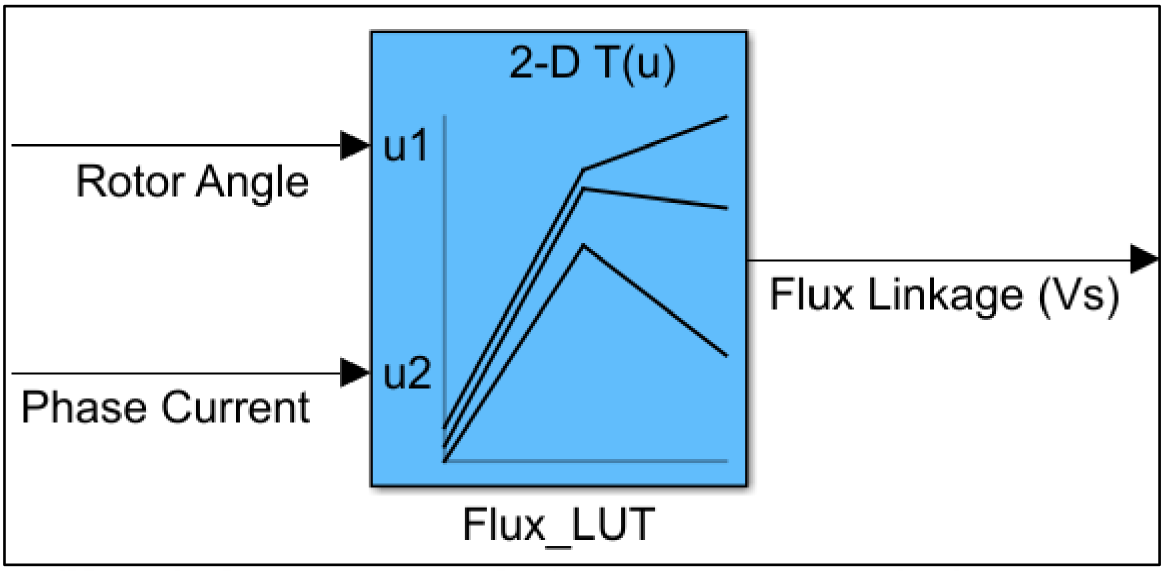

Figure 2.30. The lookup table block

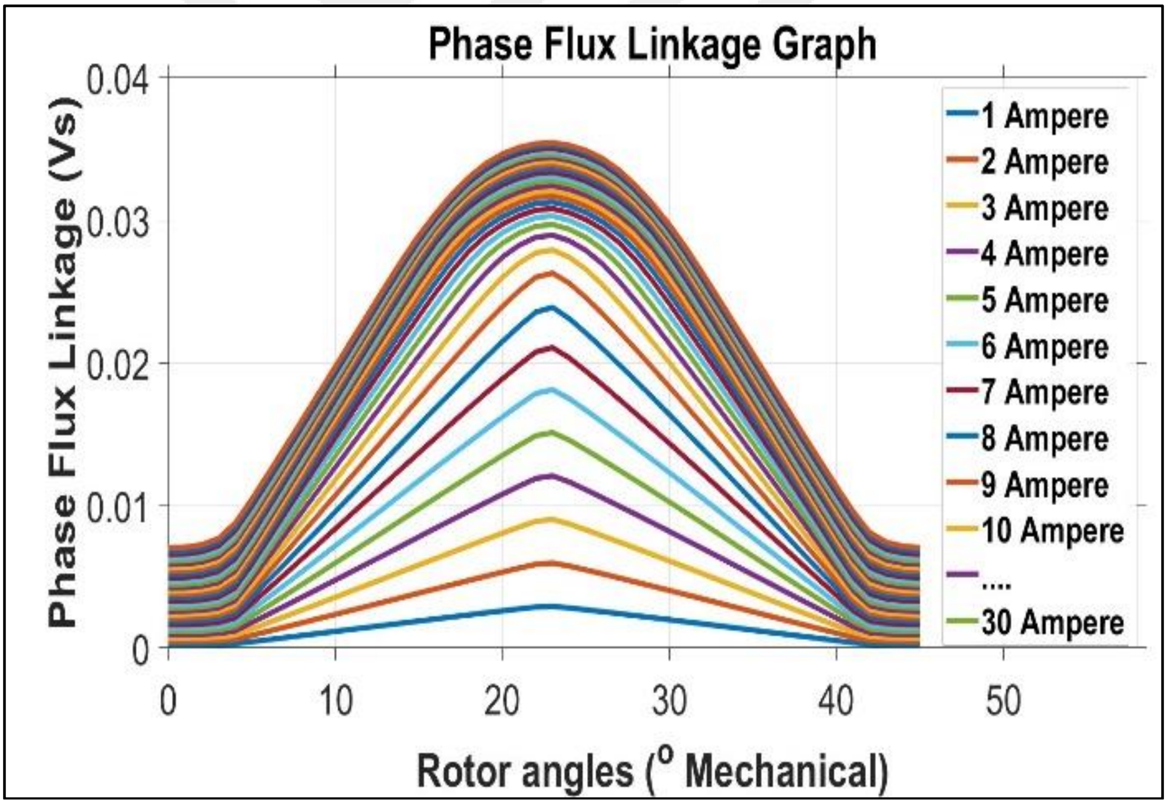

Figure 2.31. FEA results of the studied motor

2.4.6. Estimating Flux Linkage with Torque Balance Method

The FEA results obtained from the FEMM simulation have to be experimentally verified. The torque balance method was developed in [22, 23] to simplify the verification process. In this technique, the number of measurements was reduced by fixing the rotor at four positions (0◦ el, 60◦ el, 90◦ el, 120◦ el, 180◦ el). The flux linkage values at each rotor position

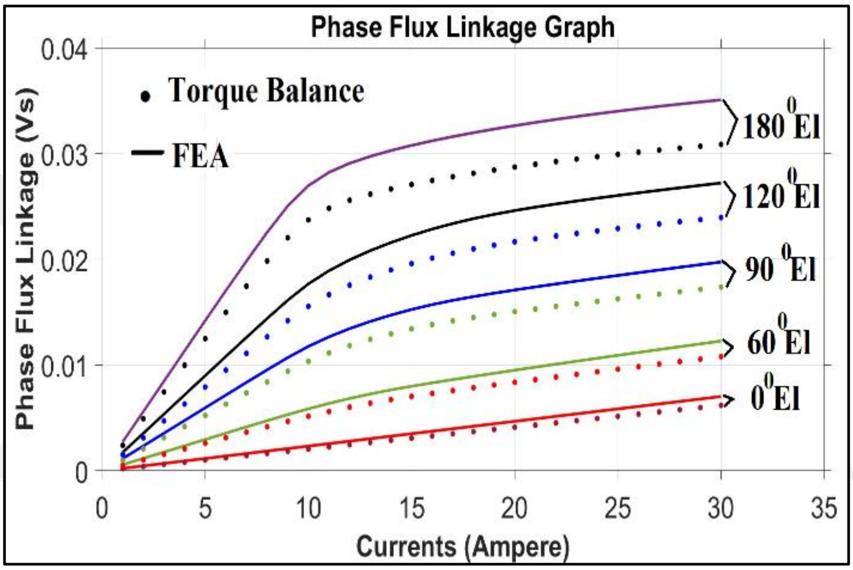

Figure 2.32. The flux linkage comparison between the FEA and the TBM

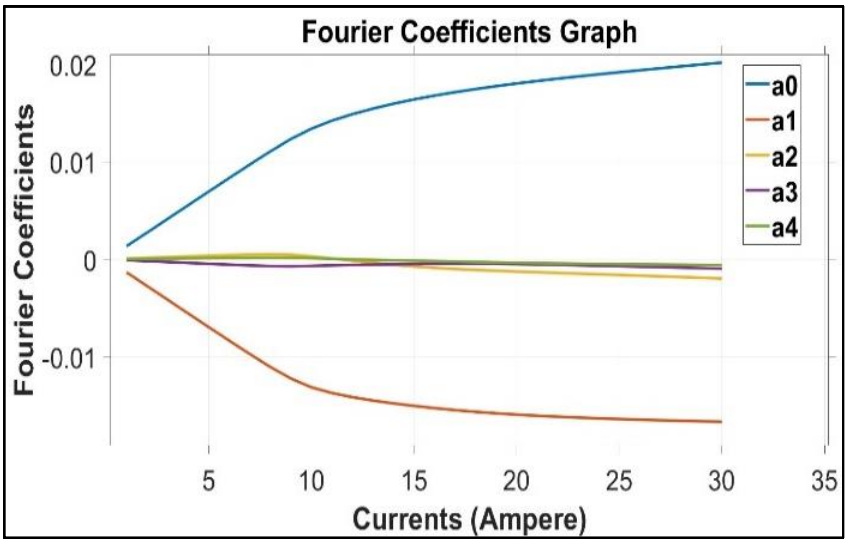

Figure 2.33. Fourier coefficients graph

was measured indirectly. Energizing the stator phases simultaneously by pulsed direct current voltage prevented the rotor to rotate. In Figure 2.32, the measurements which were taken with the TBM and FEA methods were shown comparatively.

The measured flux linkage values were used inside the four-order Fourier series in (2.6) and the Fourier coefficients shown in Figure 2.33 were calculated. Using (2.6), the flux linkage characteristics for each rotor position were calculated as shown in Figure 2.34.

$$\varphi_{ph}(\theta_{ph}, i_{ph}) = a_0(i_{ph}) + a_1(i_{ph})\cos(\theta_{ph}) + a_2(i_{ph})\cos(2\theta_{ph}) + a3\,(i_{ph})\cos(3\theta_{ph}) + a_4\,(i_{ph})\cos\,(4\theta_{ph}) \quad (2.6)$$

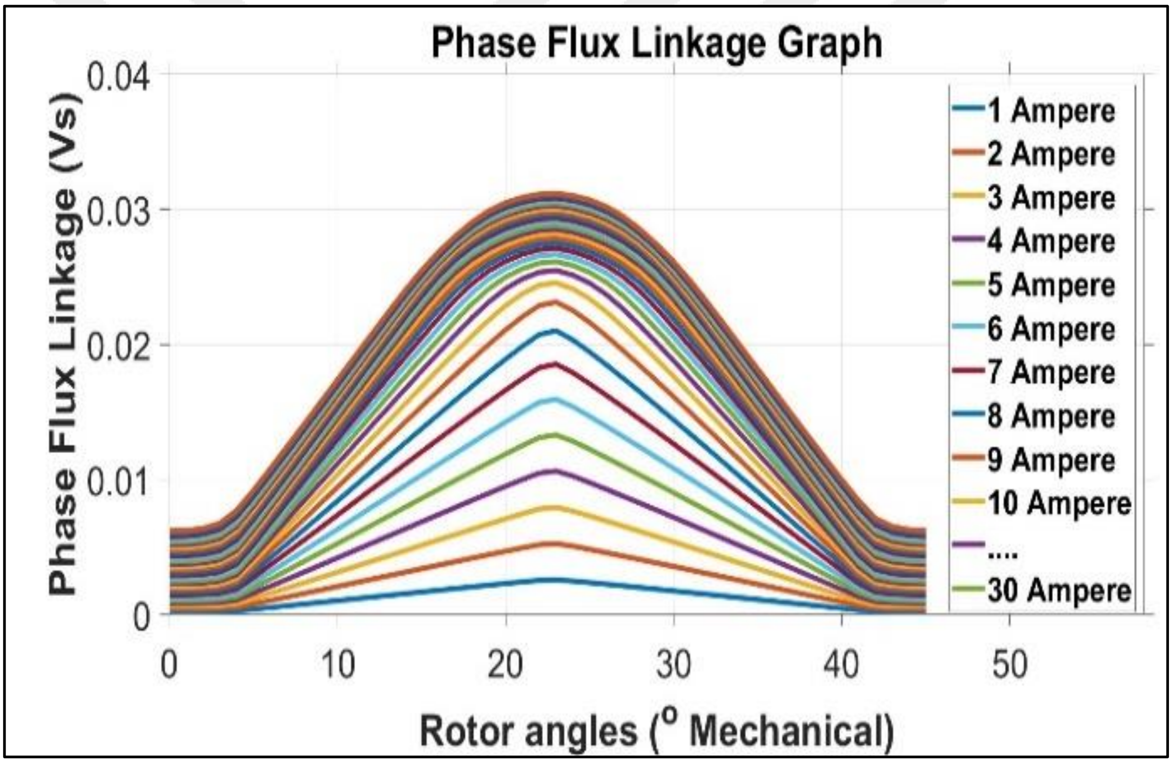

Figure 2.34. Flux linkage graph generated with TBM

2.4.7. ERSRM Controller Design

The host-target communication interface in Figure 2.18 was again used to store experimental measurement data and the system was modelled in Simulink using this data. The controller was designed using the Simulink model.

2.4.8. Experimental Measurements Under Open Loop Control

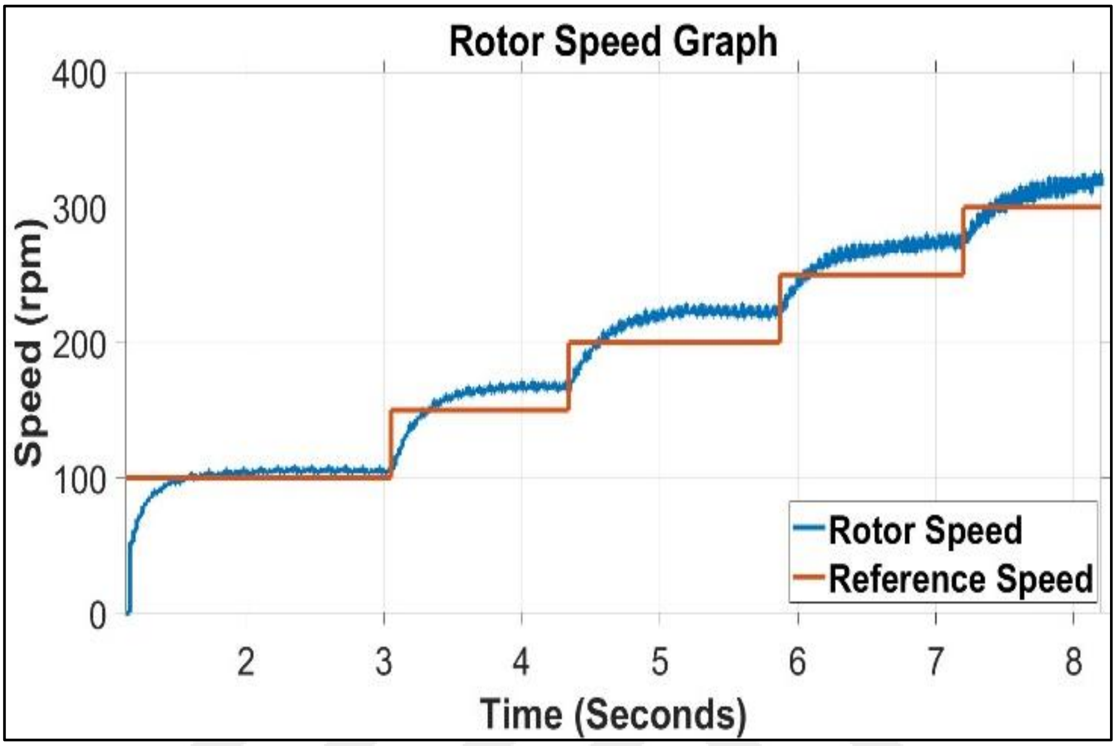

Figure 2.35. Open loop control speed response

The speed of the rotor and the phase currents were experimentally measured while the motor was driven under open loop control. First, the reference speed was applied with increasing order. The motor's speed response is shown in Figure 2.35.

2.4.9. Calculating PI Coefficients Using Zeigler-Nichols Method

In Figure 2.36, the phase currents are shown. During the start-up, the phase currents' maximum values were 21 Amps, 20 Amps, and 19 Amps for each stator phase respectively. When the rotor settles at 166 rpm, the steady-state phase currents were around 10 Amps. The Simulink model parameters were updated to match the experimentally measured outputs with the simulation outputs.

To apply the Ziegler-Nichols PI tuning method, the speed response was analyzed in the following section. From the speed response graph in Figure 2.37, the time delay and slope of the line were calculated.

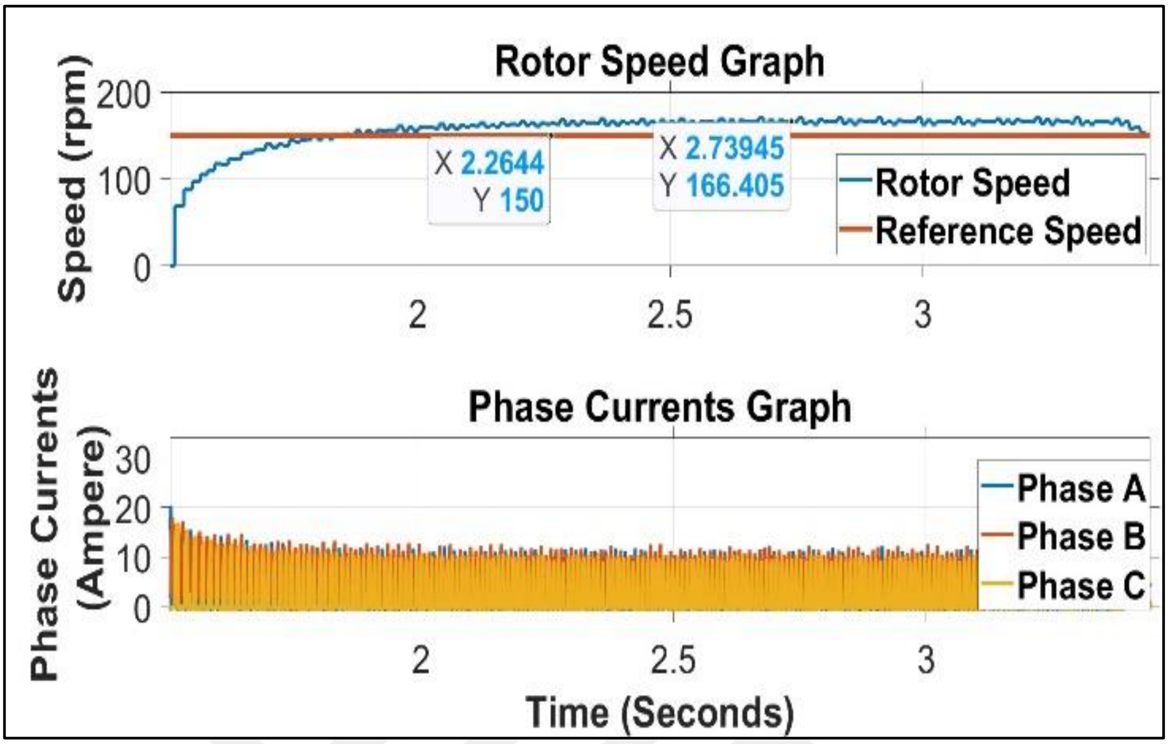

Figure 2.36. Experimental measurements of rotor speed and phase currents under open loop control

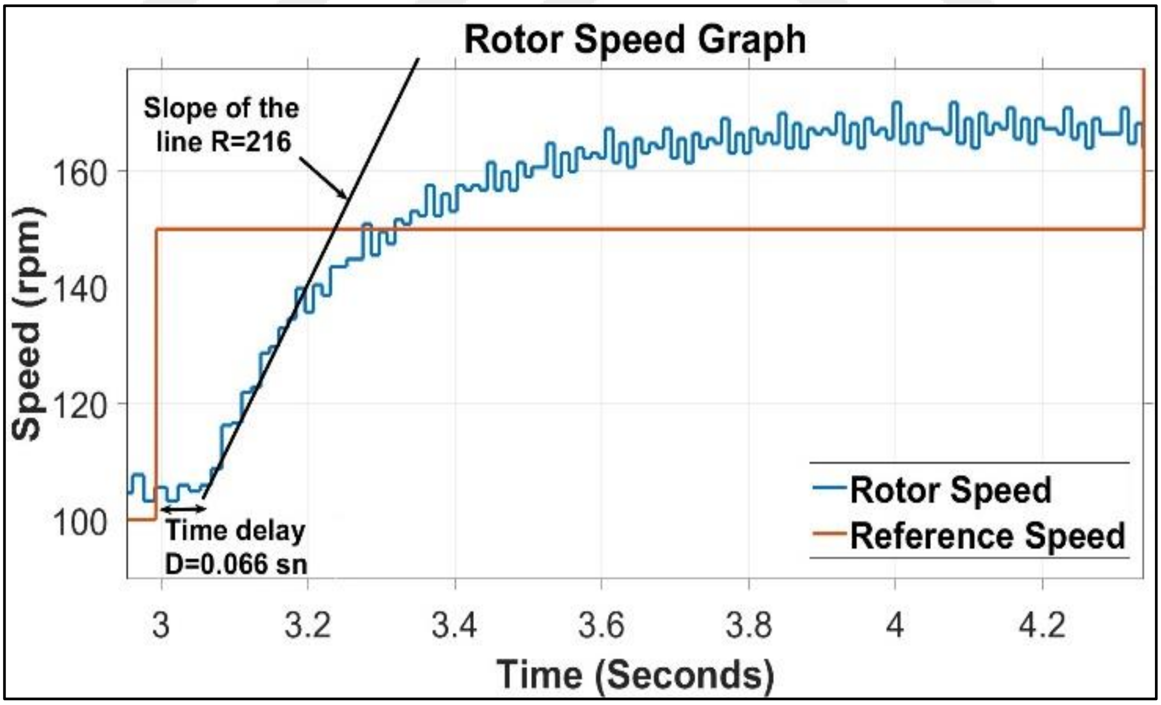

Figure 2.37. Speed response analysis

- Time delay (D)= 0.066 sn

- Slope of the line (R)=216

These values were used in the Zeigler-Nichols method and the PI parameters were calculated. According to the Zeigler-Nichols Method, the formulas in Table 2.1 was used to find the coefficients of the proportional (P) and integral (I) terms of the PI controller shown in Figure 2.38.

Table 2.1. Controller type and parameters

Controller Type	Kp	Ti
PI	0.9/(R*D)	D/0.3

From the above formulas, Kp was found as 0.063 and Ti is 0.22. Ki=Kp/Ti so Ki is 0,286. Hence, the integral gain is 0,286.

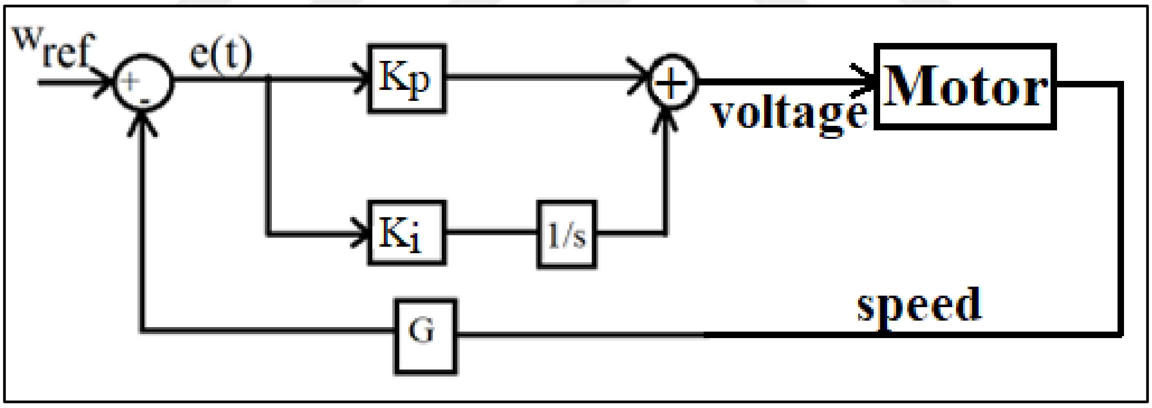

Figure 2.38. PI controller block diagram

2.4.10. Switching Table For Simulation

In the simulation, the rotor angular position was directly calculated from the rotor speed. The phase alignment and unalignment conditions were defined from the torque waveform in Figure 1.7 and Table 2.2 was formed.

Table 2.2. Phase switching signals depending on the rotor position

Rotor	S1	S2	S3	S4	S5	S6
0<θ<3	1	1	-1	-1	1	1
3<θ<13	1	1	-1	-1	-1	-1
13<θ<20	1	1	1	1	-1	-1
20<θ<30	-1	-1	1	1	-1	-1
30<θ<33	-1	-1	1	1	1	1
33<θ<45	-1	-1	-1	-1	1	1

3. FINDINGS

3.1. Real-Time Experimental Measurement Results

In Figure 3.1, the experimentally measured output of NARX NN is given. The experimental measurement showed that the estimator output followed the phase current. Similar measurement results were observed for the other two phases.

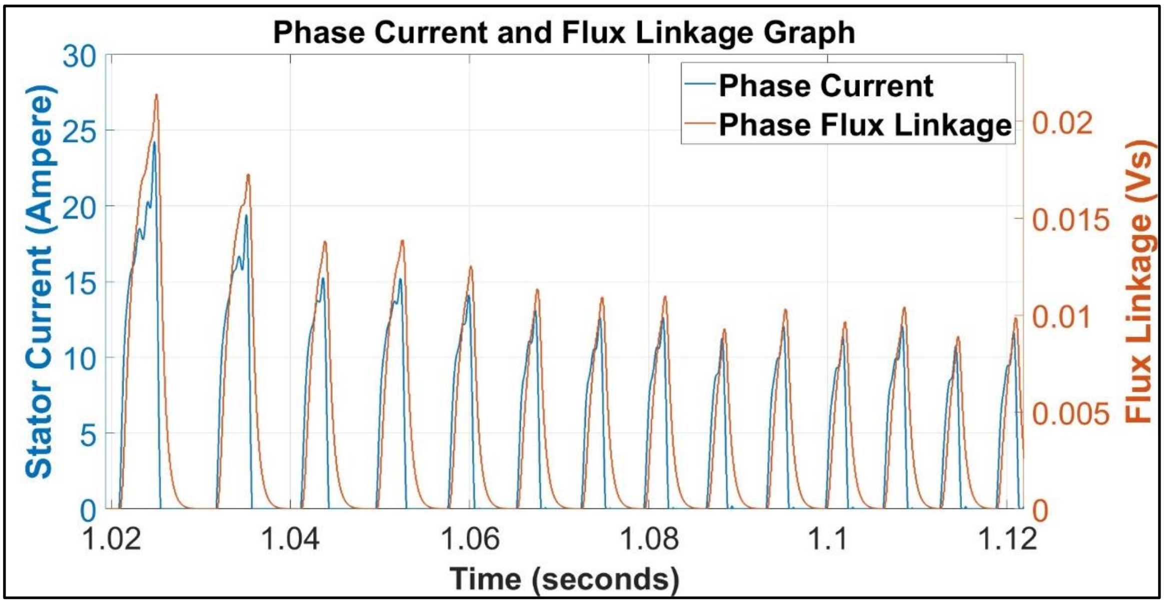

Figure 3.1. Estimated flux linkage and current measurement graphs

In Figure 3.2, the real-time measurement data which was taken using voltage – balance equation, NARX NN model, FEA, and TBM were shown comparatively.

The data values shown in Figure 3.2 at certain points were written in Table 3.1. The voltage-balance equation output was considered as the actual flux linkage value since it was calculated offline eliminating the flux linkage calculation errors as described in the previous chapter. In Figure 3.3 the estimation errors for each technique were shown as a comparison. Compared to other techniques, the NARX NN estimation output was the closest one to the actual flux linkage value. The elimination of the rotor position information during estimation also supported the superiority of the proposed technique among other techniques.

In Table 3.2 and Table 3.3, The estimation errors calculated for each technique were also written side by side with the data values in Table 3.2 and Table 3.3 to give a clearer understanding.

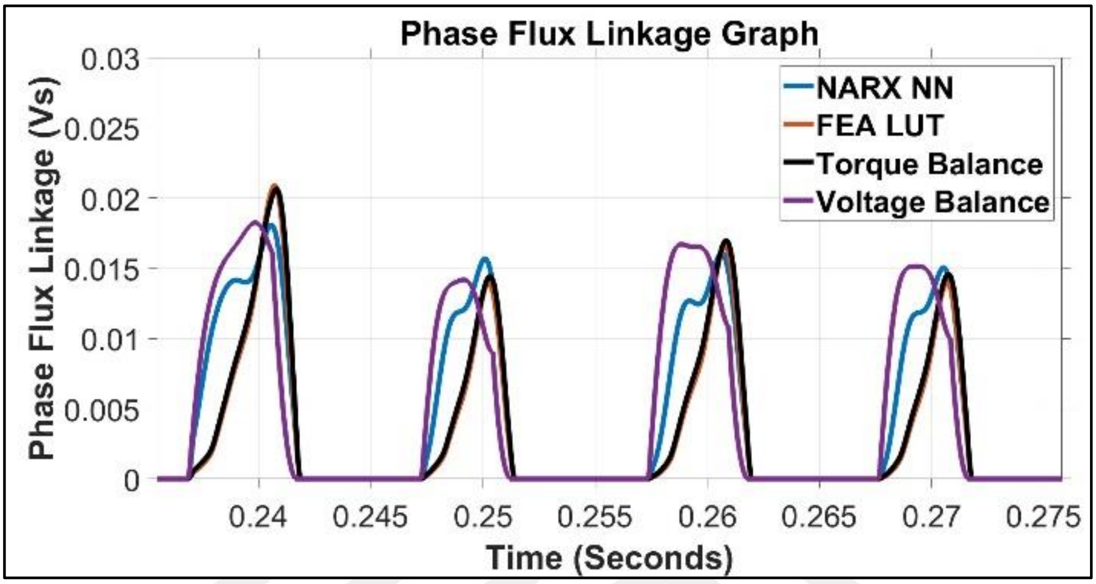

Figure 3.2. The estimation outputs using different techniques

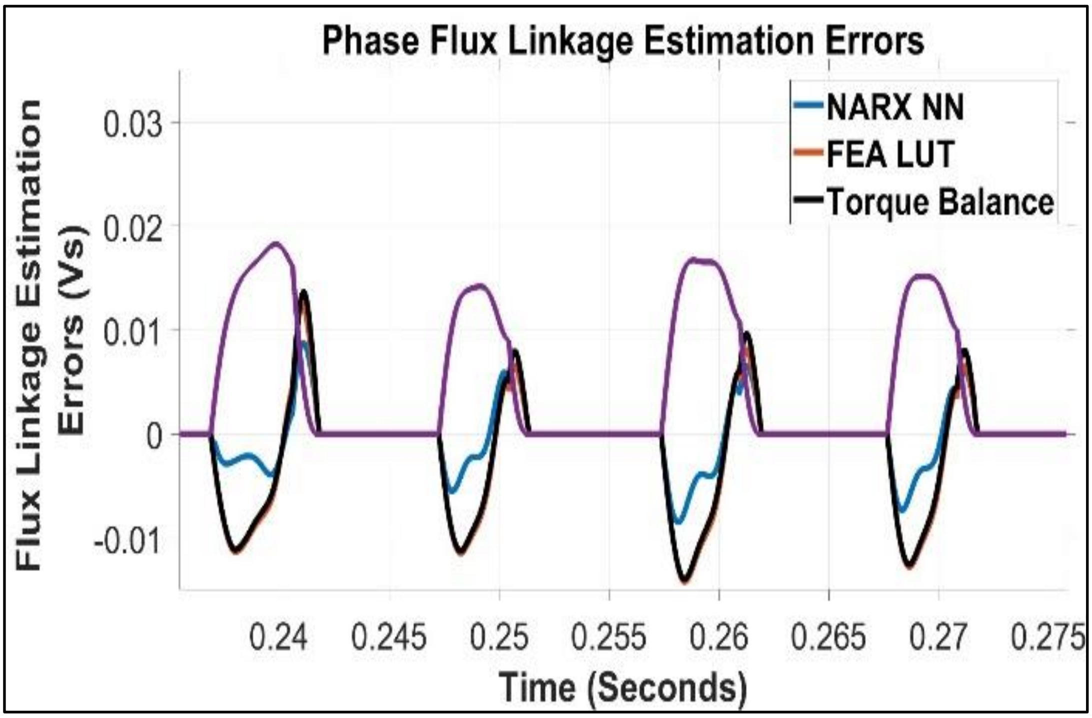

Figure 3.3. Estimation errors of the techniques compared to the voltage balance method

Table 3.1. Estimation outputs of different techniques

Voltage-balance method (reference)	NARX NN	FEA	TBM
0.0128	0.0102	0.00187	0.0019
0.0178	0.0139	0.012	0.012
0.0148	0.0179	0.018	0.0204
0.0078	0.0158	0.0194	0.019
0.013	0.0085	0.00149	0.0018
0.0139	0.0125	0.00708	0.0077
0.0118	0.0149	0.0118	0.0123
0.0059	0.0119	0.0118	0.0132
0.0149	0.0069	0.00115	0.0013
0.0164	0.0126	0.0063	0.0067
0.0145	0.0149	0.0138	0.013
0.0068	0.0129	0.0119	0.0157
0.0145	0.0084	0.0016	0.00183
0.0148	0.0124	0.00825	0.0089
0.0132	0.0141	0.0115	0.0117
0.0065	0.0120	0.0122	0.0125

Table 3.2. Comparison of the mean absolute errors

	NARX NN	FEA	TBM
Mean absolute error	-0.00089	-0.0042	-0.0037

Table 3.3. Comparison of the mean square errors

	NARX NN	FEA	TBM
Mean square error	$2.6e^{-5}$	$7.96e^{-5}$	$7.92e^{-5}$

In Figure 3.4, the oscilloscope view of the phase current and the corresponding NARX NN-based flux linkage value measured directly from the DSP Launchpad analog output pin was shown. The flux linkage value was multiplied by a constant to make it possible to view simultaneously with the phase current value. Here, the flux linkage peak value was measured as around 0.01 Vs while the peak current value was 12 Amperes.

Figure 3.4. Oscilloscope view of the current (blue line) and the flux linkage (yellow line)

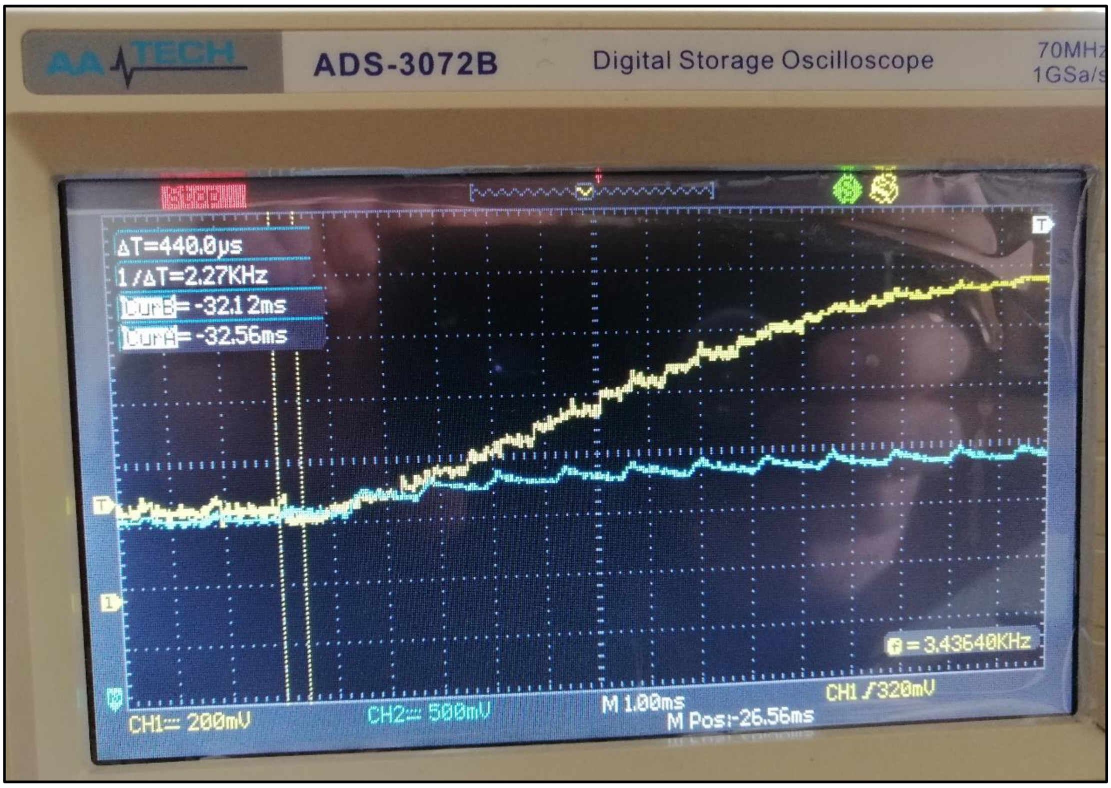

Figure 3.5. Oscilloscope view in detail

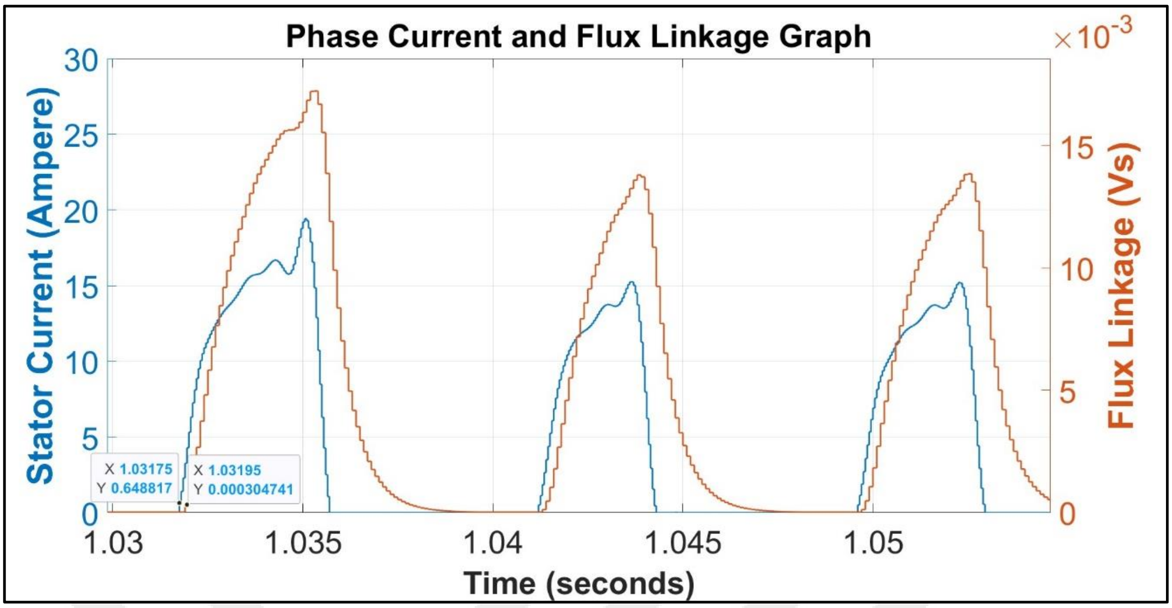

Figure 3.6. Phase current and flux linkage real-time measurement results in detail

One of the oscilloscope probes was connected to the current sensor output and the other probe was connected to the DSP Launchpad analog output pin where the flux linkage output value was given and the signal waveforms in Figure 3.5 were measured. The delay time between the unfiltered phase current and the estimated flux linkage output was measured as 440 uS. In Figure 3.6, the flux linkage and the current waveforms measured via the Simulink host-target communication interface were shown in detail. From the measurement results, the time delay between the estimated flux linkage and the filtered current was calculated as 200 uS. This means that there was a 240 uS filter delay and a 200 uS estimation delay. In terms of time delay, the NN-based estimator showed better performance than the current filter.

3.2. PI Controller Simulation Results

The PI controller speed response is illustrated in Figure 3.7. The rotor speed followed the reference speed with an acceptable overshoot and steady-state speed error. The torque waveform is shown in Figure 3.8. In Table 3.4, the torque measurement results are given. The phase currents are shown in Figure 3.9. The simulation outputs correlated with the real-time experimental measurements which are explained in the following section.

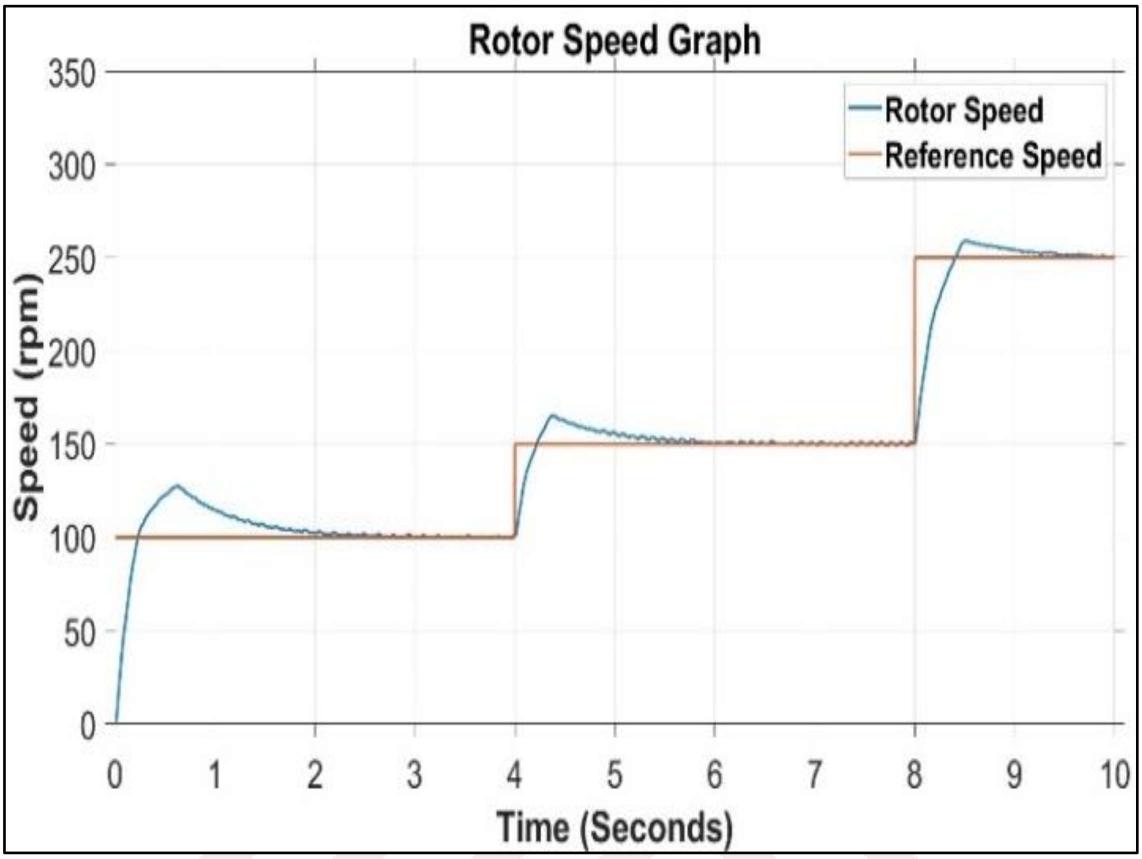

Figure 3.7. Speed response of simulation model under PI speed control

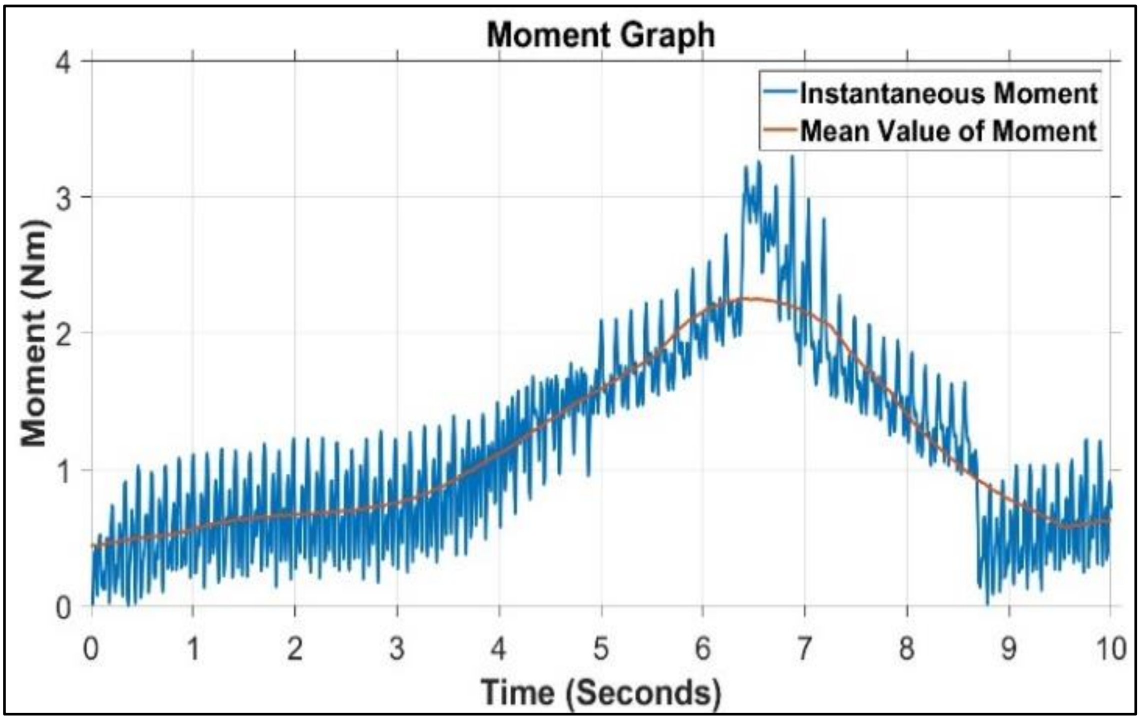

Figure 3.8. Torque waveform in ERSRM driver simulation

Table 3.4. Torque values

Torque values	At no	Loaded
Min (Nm)	0.14	1.94
Mean (Nm)	0.66	2.18
Max (Nm)	1.1	2.53
Torque Ripple	145	28

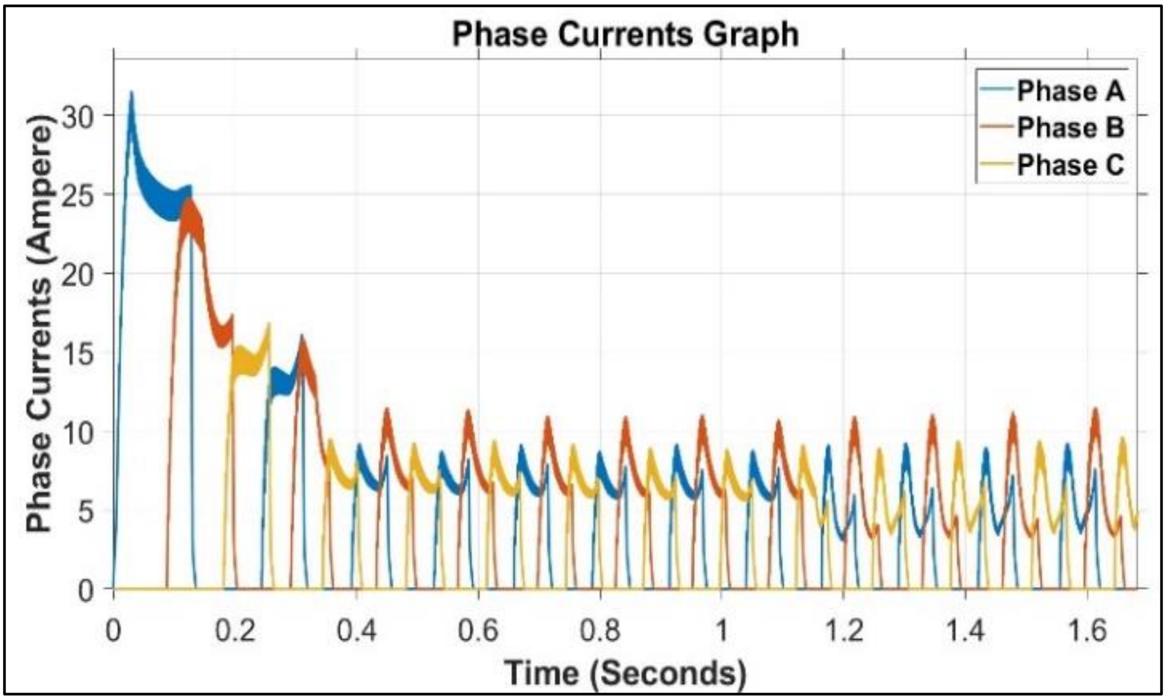

Figure 3.9. Phase currents in ERSRM driver simulation (in detail)

3.3. Experimental Results

3.3.1. Phase Excitation Measurements

The rotor position together with the phase excitation signal is shown in Figure 3.10. The rotor angular positions are shown in per-unit values to fit inside the graph. One rotational cycle was 45 mechanical degrees. There were 8 rotor poles so in one complete rotation each stator phase was energized and de-energized 8 times. In Figure 3.11, the phase excitation signals for the three phases are shown. The measured currents and the phase turn-on and off signals are drawn in Figure 3.12. The current values are given in per-unit values.

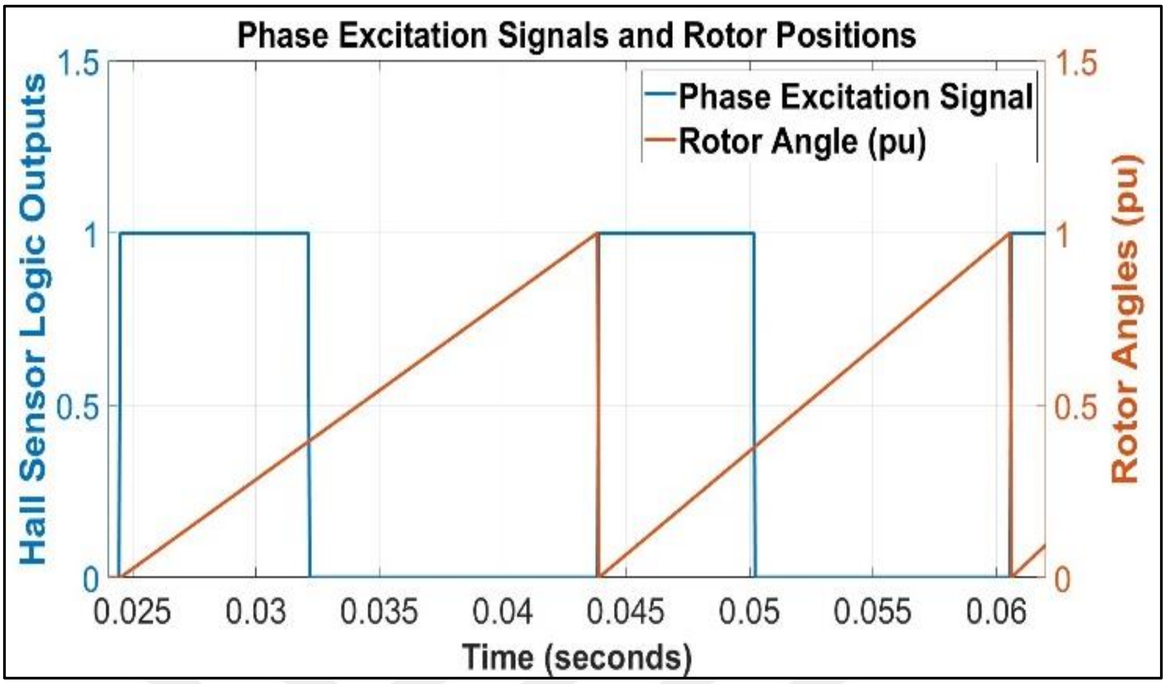

Figure 3.10. Phase excitation signals for one stator phase for each 0-45 mechanical degree

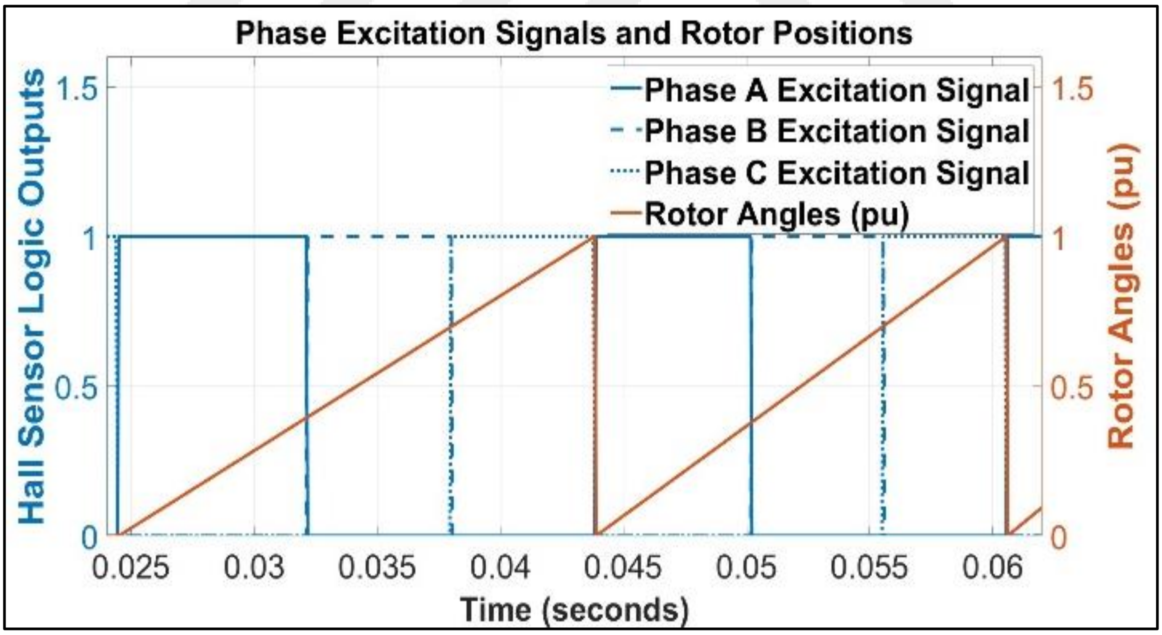

Figure 3.11. Phase excitation signals for three phases

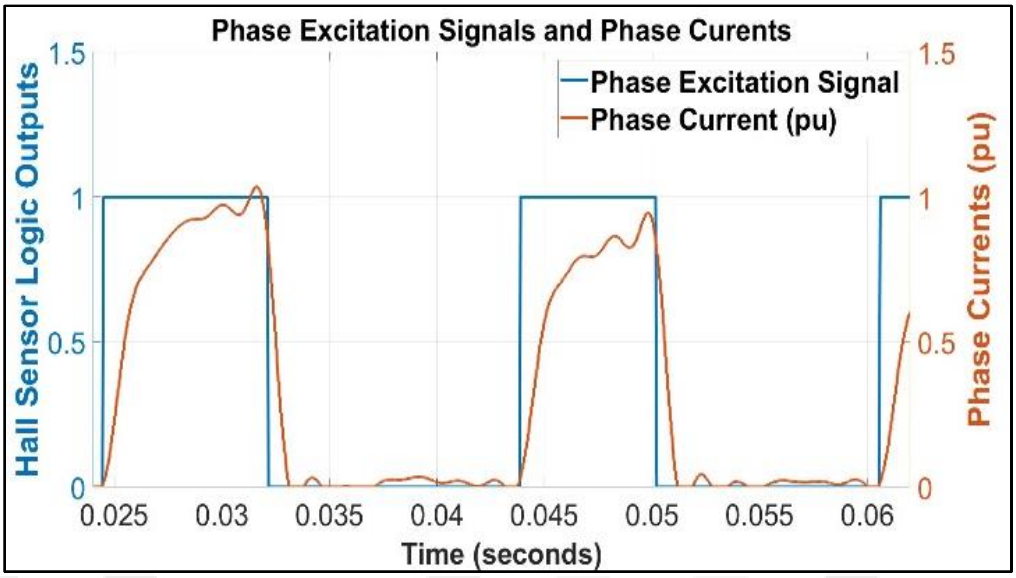

Figure 3.12. Phase excitation signal and current waveform for one phase

3.3.2. PI Controller Experimental Results

In Figure 3.13, the PI controller speed response is shown. The measurement results correlated with the simulation output which is shown in Figure 3.7. In Figure 3.14, the oscilloscope view of the phase currents is shown.

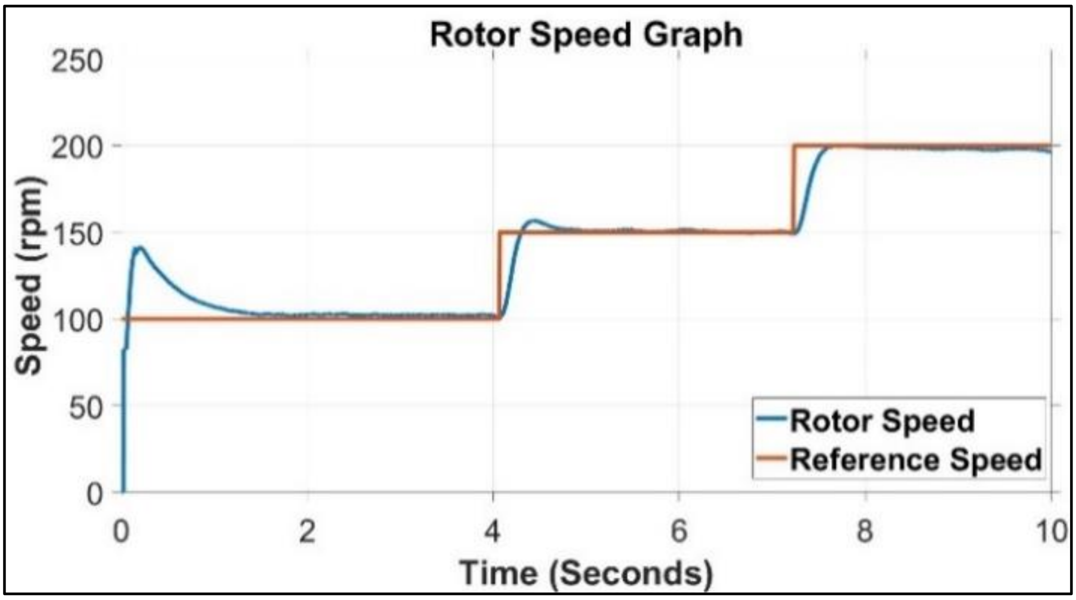

Figure 3.13. Speed response of ERSRM under PI speed control

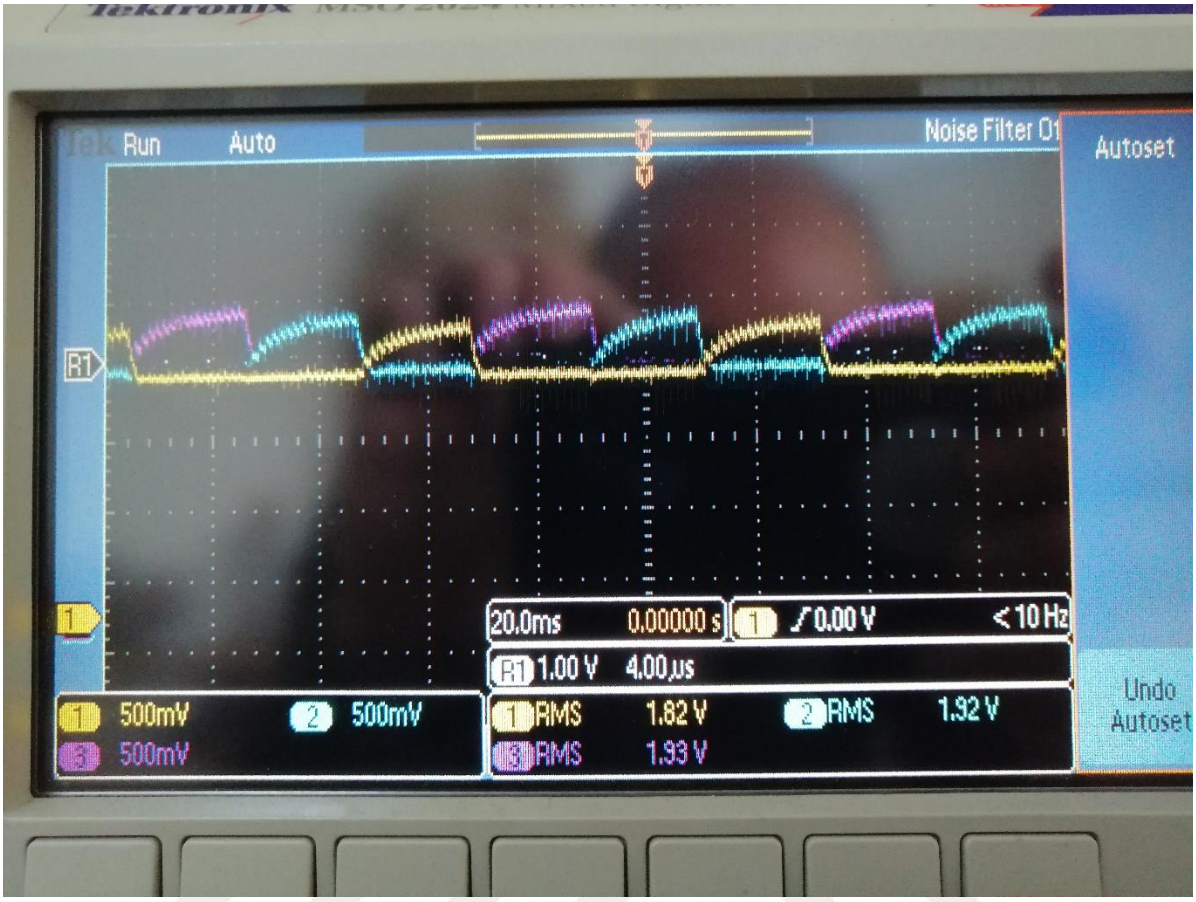

Figure 3.14. Phase current oscilloscope view under PI control

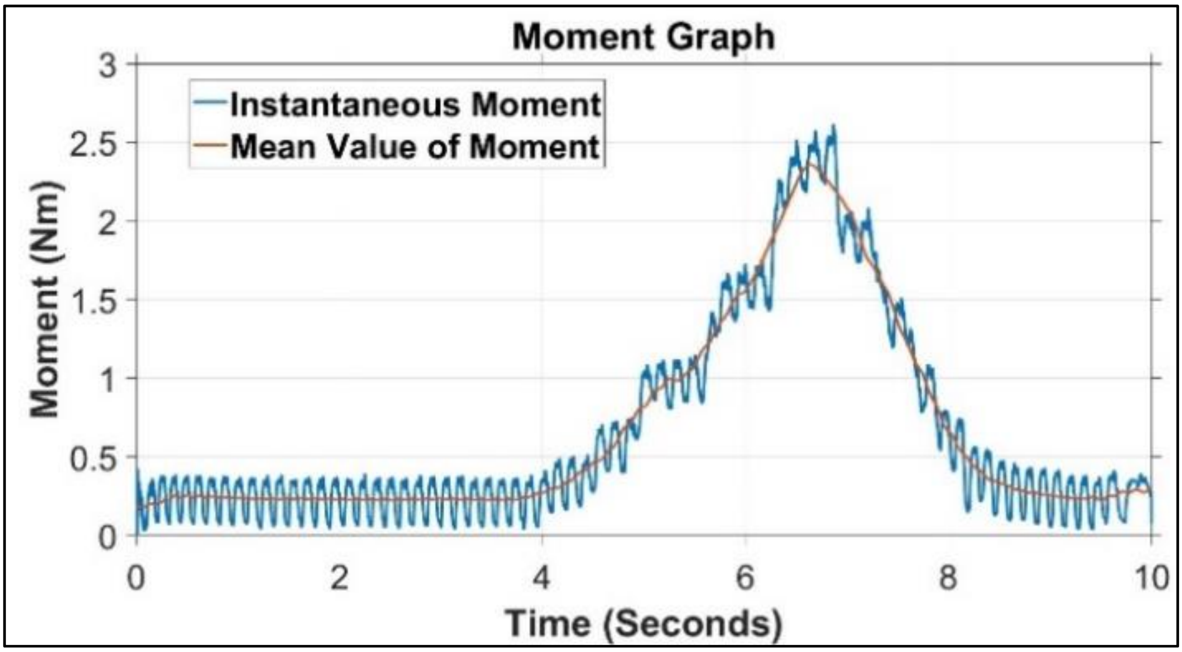

Figure 3.15. Applied motor load and output torque graph

Table 3.5. Torque waveform statistics

Torque values	No load	Loaded
Min (Nm)	0.042	2.26
Mean (Nm)	0.232	2.36
Max (Nm)	0.373	2.57
Torque Ripple (%)	142%	13%

In Figure 3.15, the moment measurement is shown. The torque ripple rates were calculated and given in Table 3.5. From the table data, the torque ripple of the 6/8 three phase ERSRM was found to be 13% under loaded conditions. The correct placement of the hall sensors contributed to this torque ripple rate.

4. DISCUSSION

4.1. Discussion of The Rotor Position Sensing System

The comparison between the current invention and the inventions in the patent database is made as follows.

Table 4.1. The comparison between the current invention and the Record 1 document

	Invention	Record 1 Document
The problem(s) solved with the invention.	Rotor position detection.	Rotor position detection.
The developed method that solves the problem.	Using one cylindrical magnet for each rotor pole and two Hall sensors for each stator pole, the rotor-stator poles' alignments and unalignments were detected for each stator phase, and the aligned stator phase was energized, the unaligned stator phase was de-energized.	The magnets were placed on the inner-runner rotor. The Hall sensor was placed on the stationary part of the motor. The position of the rotor was detected by the interaction of the magnets and the Hall sensor.
The differences between the two methods.	In record 1, the magnets were placed on the inner-runner rotor, and the magnets were placed on the outside of the rotor. In record 1, the effect of the magnets on the flux distribution was not explained.	

Table 4.1. continued

The differences between the two methods.	However, in the current invention, the magnets didn't react with the stator or rotor body hence it didn't affect the flux distribution inside the motor. The invention in record 1 was for the inner runner motor however the current invention was for the outer runner motor. In record 1, the Hall sensor was placed on the interior part of the stator, however in the current invention, the Hall sensors were outside the motor.
The comparison of the two methods.	With the current invention, the starting position of the rotor can be detected correctly. The magnetic field of the magnets didn't interact with the motor's flux path. The Hall sensor system was on the outer part of the motor so if any sensor fault occurs, the sensors can be replaced easily. Additionally, the modular structure of the Hall sensor system makes it easily mountable.

Table 4.2. The comparison between the current invention and the Record 2 document

	Invention	**Record 2 Document**
The problem(s) solved with the invention.	Rotor position detection.	Rotor position detection.
The developed method that solves the problem.	Using one cylindrical magnet for each rotor pole and two	The position sensor consists of one magnetic ring and

Table 4.2. continued

The developed method that solves the problem.	Hall sensors for each stator pole, the rotor-stator poles' alignments, and unalignments were detected for each stator pole, the rotor-stator poles' alignments and unalignments were detected for each stator phase and the aligned stator phase were energized, the unaligned stator phase was de-energized.	one Hall sensor plate. The magnetic ring was on the inner shaft of the motor. The magnet had uniform N and S poles. The position was detected by the interaction between the magnet ring and the Hall sensor.
The differences between the two methods.	In record 2, one magnet ring was used while in the current invention, one cylindrical magnet was used for each stator pole. The invention in record 2 was developed for the inner rotor motor, the current invention is developed for the outer runner motor. In record 2, the accuracy of the rotor's initial position detection was not supposed to be high because the magnet had only two poles hence there were only two possibilities about the magnet's position. When the number of stator or rotor poles was increased, the accuracy would be much lower. In the current invention, since there was one magnet for each rotor pole and two Hall sensors for each stator pole, the accuracy was much higher.	

Table 4.3. The comparison between the current invention and the Record 3 document

	Invention	**Record 3 Document**
The problem(s) solved with the invention.	Rotor position detection.	Rotor position detection.
The developed method that solves the problem.	Using one cylindrical magnet for each rotor pole and two Hall sensors for each stator pole, the rotor-stator poles' alignments and unalignments were detected for each stator phase, and the aligned stator phase was energized, the unaligned stator phase was de-energized.	A magnetic ring and a Hall sensor were used for rotor position detection. The magnetic ring mounted on the rotor didn't affect the stator magnetic flux path.
The differences between the two methods.	There was only one magnetic ring in Record 3 document, while there was one magnet for each rotor pole in the current invention. The invention in record 3 was developed for the inner runner motor, while the current invention was developed for outer runner motor.	
The comparison of the two methods.	In the current invention, using one magnet for each rotor pole and two Hall sensors for each stator pole increased the rotor position sensing accuracy.	

The comparison between the proposed rotor sensing system and the WOS literature was made as follows.

The position estimation techniques applied to SRM are restricted to a specified speed range, prone to estimation errors, and have a computational burden [42, 43]. Hence, the low cost easily mountable, and reliable rotor position detection solutions are required for the widespread usage of switched reluctance motors in the industry.

Applying the inductive sensing technique [42, 43, 44] or search coils [45] might have disadvantages such as mutual inductances that occur during the high-frequency switching operation and this might affect the position sensing accuracy. The effect of an additional winding process on the manufacturing cost of the motor is required to be clarified for this technique. The manufacturing cost of the implementation of the search coil inside the motor could be higher than the proposed system in this study.

The proposed technique in [46, 48, 49, 50] was for inner runner SRMs. The proposed technique in [47] might not be suitable for the drive system which frequently operates with start and stop. In [50], the effect of the magnets placed on the rotor's magnetic path on the motor's performance was not clearly explained.

The optical sensor [51, 52, 53, 54, 55] is an alternative to the Hall sensor approach, however, the motor's operating place conditions become important in this case. The sensors should be well-sealed to prevent any dust and dirt from coming from the outside. For precise rotor position detection, high-resolution optical encoders are required which are expensive. Additionally, with low-resolution and low-cost optical sensor solutions, the rotor initial position detection is problematic because of the incremental output of the optical sensor [54].

For in-wheel application, since the rotor is rotating outside the stator, mounting the magnets inside the drilled holes on the rotor enclosure was easier and more cost effective than mounting an optical rotary slote disc on the rotor enclosure surface. The magnets were easily stuck inside the small holes that were drilled into the rotor enclosure during production. During the experimental trials, three Hall sensors were used initially to detect the rotor's starting position. The angular distance between the Hall sensors was 120^0 mechanical. However, three Hall sensors were not sufficient to detect the starting position of three phase SRM. So, the sensor numbers were increased to two Hall sensors per stator phase. In this case, the stator-rotor pole alignment condition for each rotor position change was accurately detected. The sensors were placed at the right and left corners of each stator phase so that the motor could operate both in clockwise and counterclockwise directions.

4.2. Discussion of The NARX NN Flux Linkage Estimation Technique and The State of The Art

The magnetization characteristics of the SRM are required for drive system modelling. There are various techniques to obtain these characteristics such as the magnetic equivalent circuit method, finite element analysis (FEA) method, or by making measurements [15].

The accuracy of the magnetic equivalent circuit method [16, 17, 18, 19, 20] is lower compared to other methods due to the theoretical assumptions and simplifications made in this method [21].

More commonly, the FEA modelling technique is used in the literature for the extraction of the motor's magnetization characteristics [22, 23, 24, 25], however, the verification of the extracted data should be performed by making experimental measurements. The experimental verification process is time-consuming and might not be practical for motors operating in the field [26].

The phase flux linkage measurement methods can be classified as direct or indirect measurements [27]. Magnetic sensors were employed in the direct flux linkage measurement method [28, 29, 30]. CoCu nanowires that expose a giant magnetoresistive (GMR) effect are used for the direct measurement technique proposed in [28]. The motor's FEA model was validated using the measurement data. In [31], the number of sensors was reduced and its effect on the torque computation accuracy was studied. The direct measurement technique using magnetic sensors requires additional development and cost-reducing improvements.

In the indirect measurement method, the flux linkage profile is calculated from the voltage equation using the voltage, phase current, and phase resistance measurements. This method was more commonly used in the literature [21, 26, 32, 33, 34]. In [35], the extraction of the flux-linkage profile from the static torque measurements was also specified as an indirect method. Additionally, it was mentioned that numerical integration of the voltage equation had yielded better results.

The phase flux linkage of an SRM was measured indirectly in [26] from the phase winding voltage and the phase current measurements with and without rotor locking devices. The authors expressed the disadvantage of using a rotor locking device as the requirement of an additional mechanical construction to lock the rotor at each angular position and the spent time to perform the measurements. However, it was highlighted that eliminating the rotor locking device for the flux linkage profile measurement brings the necessity of an appropriate driver with special software.

A rotor clamping device was used in [21] to measure the flux linkage so that the rotor was fixed at each angular position by the stepper motor. The voltage-balance method was used to calculate the flux-linkage profile.

The torque balance method (TBM) which was explained in [33, 34] is another method for extracting the SRM flux linkage profile. This method reduces the measurement effort, but the rotor position is still required for real-time flux linkage estimation. So, in real-time operation, accurate rotor position measurement or estimation is required to calculate the phase flux linkage.

An online phase resistance compensation was proposed in [32] to improve the accuracy of the flux-linkage estimation.

The data reconstruction method was proposed in [36] to obtain the flux linkage profile of SRM, excluding the extra mechanics and absolute position encoder. The torque balance method was used for flux linkage measurements and the flux linkage profile at each angular rotation was interpolated from the measured data.

The flux linkage calculator in [32] still had an offset to be autotuned at every work cycle. The flux-linkage estimation model based on an artificial neural network (ANN) was proposed in [37]. The air gap magnetic field between the stator and translator was measured using a Hall effect sensor. The position and the phase current were used as inputs of an ANN which consists of two hidden layers. This ANN was used to estimate the flux linkage. The ANN-based flux linkage estimator in [36] had two inputs. The inputs were phase current and rotor position. However, in this Ph.D. thesis, there was one input which was only phase current. Additionally, the ANN-based estimator in [37] was designed for linear SRM.

5. RESULTS

The Hall sensor system which was developed throughout the Ph.D. thesis work, brought the advantage of controlling the motor without any prior knowledge of motor characteristics. This resulted in making direct measurements and generating data to develop the system model. Using the system model, a PI speed controller was designed. The torque ripple was measured as 13 % and the speed regulation was below 5 %. As a comparison, the torque ripple rate in [56] was 41.5 % without applying any special torque ripple minimization control technique. In [56], the fuzzy logic-based current modulation technique was applied and the torque ripple was reduced to 15.7 %. However, in this Ph.D. thesis, the torque ripple was measured as 13 % without applying any special torque ripple minimization technique and further improvements are possible by applying torque ripple minimization control techniques. These results occurred with the correct placement of Hall sensors. The stator phases were energized and de-energized according to the signals coming from Hall sensors.

The developed NARX Neural Network model was useful to estimate the flux linkage solely using the phase current signal as input. Hence, the rotor position information was not needed. As was mentioned in the "Discussion Section", other ANN-based flux estimation techniques in the literature used rotor position information to estimate phase flux linkage. Especially for direct torque control applications, phase flux linkage value is required to keep the flux linkage value in a certain trajectory. Both in the lookup table approach and other flux linkage estimation techniques, the magnetization characteristics of the SRM are required. In some applications, the rotor position was measured using high-resolution position encoders. In some other applications, the rotor position was estimated from the magnetization characteristics and measured phase currents. But in this Ph.D. thesis, it was proved that the SRM could be operated without prior knowledge of magnetization characteristics. To reach this goal, the NARX NN was thought with the previously calculated phase flux linkage values and phase current values. The NN teaching, validation, and test data were generated by operating the motor with the help of the original, low-cost Hall sensor system. As a result, the NARX NN technique for estimating the flux linkage eliminates the necessity of rotor position input and prior knowledge of the machine magnetization characteristics.

From the experimental measurements, the time delay between the NARX NN flux linkage estimator output and the filtered current signal was found as 200 uS. And the time delay between the unfiltered phase current and the NN-based-flux linkage estimation output was found as 440 uS. This means that there was a 240 uS filter delay and a 200 uS estimation delay. In terms of time delay, the NN-based estimator showed better performance than the current filter. For sure, the time delay of LUT-based estimation is much lower, but regarding the advantage of eliminating the rotor position sensor, the NN based-flux linkage estimator is applicable in electric motor control loops.

As a comparative study, the NARX NN flux linkage estimator output was compared with other methods which were the voltage balance method, FEA, and torque balance method. The flux linkage calculated using the voltage equation was taken as actual values. The mean absolute error value between the voltage balance method and NARX NN was -0.00079, while it was -0.0041 for FEA and -0.0038 for TBM based flux linkage estimator. This showed that even without the rotor encoder feedback, the NARX NN flux estimator gave satisfactory results.

6. SUGGESTIONS

The NARX NN flux linkage estimator model was developed mainly for direct torque control applications. In the real-time application, the time delay between the estimated flux linkage and the filtered current signal was 80 samples which means 200 uS at 400 kHz sampling frequency. For future studies, the developed estimation algorithm's performance will be evaluated for the direct torque control technique applied to SRM. Especially for high-speed operations, to deal with the time delay, the writer suggests using FPGA-based controllers which can operate at higher clock frequencies and the maximum achievable sampling frequency is higher.

The maximum sampling frequency of host-target communication in Matlab & Simulink is 20 kHz. However, Matlab & Simulink has a hardware support package for simulators that work at several Mhz sampling frequencies. Working at higher sampling frequencies means capturing signals with higher precision and with higher frequency components and this results in increasing the accuracy of the system modelling.

For future studies, the NARX NN-based phase flux estimator algorithm will be implemented with a direct torque control algorithm. ANN was proved to be an effective technique for electric machine parameter estimation. The ongoing research activities of the writer include rotor position estimation, torque estimation as well as modelling and control of electric drive systems.

7. RESOURCES

1. Xue, X. D., Cheng, K. W. E. and Cheung, N. C., Selection Of Electric Motor Drives For Electric Vehicles, Australasian Universities Power Engineering Conference, December 2008, Sydney, 170-176.

2. http://www.allianceorg.com/magnetandmaterialcosts.html Commodity Prices. 20.09.2022.

3. Andrada, P., Torrent, M., Blanqué, B. and Perat, J.I., Switched Reluctance Drives For Electric Vehicle Applications, Renewable Energies and Power Quality Journal, 1 (2003) 311-31.

4. Cao, W., Mecrow, B. C., Atkinson, G. J., Bennett, J. W. and Atkinson D. J., Overview Of Electric Motor Technologies Used For More Electric Aircraft (MEA), IEEE Transactions on Industrial Electronics, 59, 9 (2012) 3523-3531.

5. Lin, J., Cheng, K.W.E., Zhang, Z. and Xue, X., Experimental Investigation Of In-Wheel Switched Reluctance Motor Driving System For Future Electric Vehicles, 3rd International Conference on Power Electronics Systems and Applications, November 2009, Hong Kong, 1-6.

6. Cakir, K. and Sabanovic, A., In-wheel Motor Design for Electric Vehicles, 9th IEEE International Workshop on Advanced Motion Control, March 2006, Istanbul, 613-618.

7. Krishnan R. and Materu P., Measurement And Instrumentation Of A Switched Reluctance Motor, Conference Record of the IEEE Industry Applications Society Annual Meeting, 1 (1989) 116-121, doi: 10.1109/IAS.1989.96639.

8. DiRenzo M., Switched Reluctance Motor Control – Basic Operation and Example Using the TMS320F240, https://d1.amobbs.com/bbs_upload782111/files_9/ourdev_262731.pdf 20.09.2022.

9. Tang X., Sun X., Yao M., An Overview of Position Sensorless Techniques for Switched Reluctance Machine Systems, Applied Sciences, 12, 7 (2022), 3616, https://doi.org/10.3390/app12073616.

10. Narla S., Modelling and Control of Switched Reluctance Machines For Four Quadrant Operation, Master Thesis, The Graduate Faculty of The University of Akron, Akron, 2010.

11. M. V. de Paula, de Almada Lopes T., d. S. Barros T.A, Filho P. S. N. and Filho E. R., Mathematical Modeling of Switched Reluctance Machines: Development and Application, Modelling and Control of Switched Reluctance Machines, IntechOpen [Online], London, United Kingdom, 2020 Available: https://www.intechopen.com/chapters/68973 doi: 10.5772/intechopen.89061

12. https://uk.mathworks.com/help/deeplearning/ref/narxnet.html
Nonlinear Autoregressive Neural Network With External Input. 15.06.2022

13. Mathew A. R., Bindu R. and Thale S., Design of A Power Electronic Drive for a Small Utility Electric Vehicle, IEEE India Council International Subsections Conference (INDISCON), 2020, 72-77, doi: 10.1109/INDISCON50162.2020.00027.

14. R. Zhong et al., Accurate Model of Switched Reluctance Motor Based on Indirect Measurement Method And Least Square Support Vector Machine, IET Electrical Power Applications, 10, 9 (2016), 916–922.

15. Lukman G. F., Nguyen X. S. and Ahn J.-W., Design of a Low Torque Ripple Three-Phase SRM for Automotive Shift-by-Wire Actuator, Energies, 13, 9 (May 2020), 2329, doi: 10.3390/en13092329.

16. W. Sun, Q. Li, L. Sun, L. Zhu and L. Li, Electromagnetic Analysis on Novel Rotor-Segmented Axial-Field SRM Based on Dynamic Magnetic Equivalent Circuit, IEEE Transactions on Magnetics, 55, 6 (June 2019), 1-5, doi: 10.1109/TMAG.2019.2901002.

17. Grebennikov N., Talakhadze T. and Kashuba A., Equivalent Magnetic Circuit for Switched Reluctance Motor with Strong Mutual Coupling between Phases, 26th International Workshop on Electric Drives: Improvement in Efficiency of Electric Drives (IWED), 2019, 1-5, doi: 10.1109/IWED.2019.8664226.

18. Watthewaduge G. and Bilgin B., Reluctance Mesh-Based Magnetic Equivalent Circuit Modeling of Switched Reluctance Motors for Static and Dynamic Analysis, IEEE Transactions on Transportation Electrification, 8, 2 (June 2022), 2164-2176, doi: 10.1109/TTE.2021.3132885.

19. Franke M., Punk O., Brutscheck M. and Schmucker U., Magnetic Equivalent Circuit Modeling of Rolling Rotor Switched Reluctance Motors, 33rd International Spring Seminar on Electronics Technology, 2010, 320-325, doi: 10.1109/ISSE.2010.5547311.

20. Banerjee R. and Sensarma P., Improved Analytical Method to Determine Flux-Linkage Characteristics of a Switched Reluctance Machine, IEEE Transactions on Industry Applications, 56, 6 (November 2020), pp. 6314-6323, doi: 10.1109/TIA.2020.3012105.

21. Song S., Ge L., Ma S., Zhang M., and Wang L., Accurate Measurement and Detailed Evaluation of Static Electromagnetic Characteristics of Switched Reluctance Machines, IEEE Transactions on Instrumentation and Measurement, 64, 3 (March 2015), 704-714, doi: 10.1109/TIM.2014.2358132.

22. Singh V. K., Sharma U., and Singh B., A Robust Design Methodology with FEA of SRM for Efficient Heavy Duty Exhaust Fan Application, IEEE 4th International Conference on Computing, Power and Communication Technologies (GUCON), 2021, Kuala Lumpur, 1-6, doi: 10.1109/GUCON50781.2021.9573636.

23. Rallabandi V., Han P., Wu J., Cramer A. M., Ionel D. M. and Zhou P., Design Optimization and Comparison of Direct-Drive Outer-Rotor SRMs Based on Fast

Current Profile Estimation and Transient FEA," IEEE Transactions on Industry Applications, 57, 1 (Jan.-Feb. 2021), 236-245, doi: 10.1109/TIA.2020.3029995.

24. Singh V. K., Sharma U. and Singh B., Design FEA and Dynamic Simulation Based Model of an Outer Rotor SRM for an Efficient Fan Application, IEEE International Conference on Power Electronics, Drives and Energy Systems (PEDES), 2020, Jaipur, 1-6, doi: 10.1109/PEDES49360.2020.9379688.

25. Jayapragash R. and Chellamuthu C., Analysis of Switched Reluctance Machine Using FEA for Renewable Energy System, International Conference on Power, Energy and Control (ICPEC), 2013, Dindigul, 777-781, doi: 10.1109/ICPEC.2013.6527760.

26. Zhengyu L., Reay D. S. and Zhou B., Experimental Measurement of Switched Reluctance Motor Non-linear Characteristics, IECON 2013 - 39th Annual Conference of the IEEE Industrial Electronics Society, 2013, Vienna, 2827-2832, doi: 10.1109/IECON.2013.6699579.

27. Krishnan R. and Materu P., Measurement and Instrumentation of a Switched Reluctance Motor, Conference Record of the IEEE Industry Applications Society Annual Meeting, 1989, San Diego, 1, 116-121, doi: 10.1109/IAS.1989.96639.

28. McCann R. and Traore W., Investigation of Direct Flux Measurements In Switched Reluctance Motors, IEEE Power and Energy Society General Meeting - Conversion and Delivery of Electrical Energy in the 21st Century, 2008, Pittsburgh, 1-7, doi: 10.1109/PES.2008.4596841.

29. Prescot J. C. and. El-Kharashi A. K, A Method for Measuring Self-inductance Applicable to Large Electrical Machines, Proceedings of the IEE - Part A: Power Engineering, 106, 26 (1959), 169–173.

30. Cheok A. D. and Ertugrul N., Computer-based Automated Test Measurement System for Determining Magnetization Characteristics of Switched Reluctance Motors, IEEE Transactions on Instrumentation and Measurement, 50, 3 (June 2001), 690-696, doi: 10.1109/19.930441.

31. McCann R. A. and Traoré W. F., Determination of Instantaneous Torque From Airgap Flux Measurements In a Switched Reluctance Motor, IEEE PES General Meeting, 2010, Minneapolis, 1-8, doi: 10.1109/PES.2010.5589832.

32. Fuengwarodsakul N. H., Bauer S. E., Krane J., Dick C. P. and De Doncker R. W., Sensorless Direct Instantaneous Torque Control for Switched Reluctance Machines, European Conference on Power Electronics and Applications, 2005, Dresden, 10-P.7, doi: 10.1109/EPE.2005.219423.

33. Ge L., Zhong J., Huang J. and Song S., Model Predictive Torque Control of Switched Reluctance Machine Based on Torque-balanced Measurement and Flux-based Torque Estimation, 24th International Conference on Electrical Machines and Systems (ICEMS), 2021, Gyeongju, 867-872, doi: 10.23919/ICEMS52562.2021.9634366.

34. Ge L., Zhong J., Huang J., Jiao N., Song S. and Doncker R. W. D., A Novel Model Predictive Torque Control of SRMs with Low Measurement Effort, IEEE Transactions on Industrial Electronics, doi: 10.1109/TIE.2022.3179564.

35. Lu K., Rasmussen P. O. and Ritchie A. E., Investigation of Flux-Linkage Profile Measurement Methods for Switched-Reluctance Motors and Permanent-Magnet Motors, IEEE Transactions on Instrumentation and Measurement, 58, 9 (September 2009), 3191-3198, doi: 10.1109/TIM.2009.2017154.

36. Liu J., Wang G., Sun L., Liu D. and Fan Y., A Novel Method to Obtain the Flux-Linkage Characteristics of Switched Reluctance Motors, IEEE Transactions on Magnetics, 57, 11 (Nov. 2021), 1-11, doi: 10.1109/TMAG.2021.3111521.

37. Ozden S., Manav G. and Dursun M., ANN Based Magnetic Field and Inductance Modeling of Double Sided Linear Switched Reluctance Motor, 5th International Conference on Electrical and Electronic Engineering (ICEEE), 2018, Istanbul, 133-137, doi: 10.1109/ICEEE2.2018.8391316.

38. Sandhya Krishnan, How to Determine The Number of Layers and Neurons In The Hidden Layer? https://medium.com/geekculture/introduction-to-neural-network-2f8b8221fbd3 20.06.2022

39. https://uk.mathworks.com/help/deeplearning/ref/tansig.html;jsessionid=2cd8a35867066ff3a46d565cd804, Hyperbolic Tangent Sigmoid Transfer Function, 25.06.2022.

40 https://www.mathworks.com/help/deeplearning/ug/maglev-modeling.html, Maglev Modeling, 25.06.2022.

41. Ustkoyuncu N., Application of An In-wheel Direct Drive Motor Based on Switched Reluctance Motors for Low-power Electric Vehicles, Sadhana-Academy Proceedings In Engineering Sciences , 44, 1 (2019).

42. Cai J., Lu L., Liu Z., Jia H., Zhao X. and Xu F., An Inductive Position Sensor with Switched Reluctance Motor Structure, 20th International Conference on Electrical Machines and Systems (ICEMS), 2017, Sydney, 1-4, doi: 10.1109/ICEMS.2017.8056495.

43. J. Cai and Z. Deng, "Switched-Reluctance Position Sensor," IEEE Transactions on Magnetics, 50, 11 (November 2014), 1-4, doi: 10.1109/TMAG.2014.2329957.

44. Corda J.and Ouhab B., Discrete Position Sensing For a Linear Switched Reluctance Motor, Eighth International Conference on Power Electronics and Variable Speed Drives (IEE Conf. Publ. No. 475), September 2000, London, 317-320, doi: 10.1049/cp:20000265.

45. Duck-Shick S. et al., Rotor Position Sensing Method For Switched Reluctance Motors Using An Indirect Sensor", Journal of Power Electronics, 5, 3 (July 2005), 173-179.

46. Han, G., Chen, H. and Guan, G., Low-cost SRM Drive System With Reduced Current Sensors And Position Sensors. IET Electric Power Applications, 13, 7 (July 2019), 853-862, https://doi.org/10.1049/iet-epa.2018.5209.

47. Makni Z., Bouallaga K. and Dupuis D., Effective Starting Procedure For a Three-phase Switched Reluctance Motor, Ninth International Conference on Ecological Vehicles and Renewable Energies (EVER), 2014, Monte-Carlo, 1-7, doi: 10.1109/EVER.2014.6844130.

48. Han, G., Chen, H. and Guan, G., Rotor Position Tolerant Detection Method for SRM Drive System with Misaligned Position Sensors. IET Electric Power Applications, 13, 6 (June 2019), 730-741, https://doi.org/10.1049/iet-epa.2018.5243.

49. Lu J. X., Ebihara D., Hamatsu K. and Arima H., A Movable Angle Control Strategy of Switched Reluctance Motor with Hall-effect Position Sensor, Proceedings IPEMC Third International Power Electronics and Motion Control Conference (IEEE Cat. No.00EX435), 3, August 2000, Beijing, 1279-1284, doi: 10.1109/IPEMC.2000.883026.

50. Saifee M. B., Javed M. U., Sohaib M. and Zaffar N. A., PSIM Modelling and Hall Sensors Based Adaptive Control of Switched Reluctance Motor Drive for EV Applications, 43rd Annual Conference of the IEEE Industrial Electronics Society, 2017, Beijing, 2133-2137, doi: 10.1109/IECON.2017.8216358.

51. Yoon Y., et al., A Low Cost Position Sensing Method with Optical Sensors for Switched Reluctance Motor, Journal of Power Electronics, 5, 3 (July 2005).

52. Park S-J., Ahn J-W., Lee M-H. and Lipo T. A., Novel Encoder for SRM Drive with High Resolution Angle Control, IEEE International Symposium on Industrial Electronics Proceedings (Cat. No.01TH8570), 3, 2001, Pusan, 1781-1785, doi: 10.1109/ISIE.2001.931980.

53. Ahn J-W., Park S-J. and Lee D-H., Novel Encoder for Switching Angle Control of SRM, IEEE Transactions on Industrial Electronics, 53, 3 (June 2006), 848-854, doi: 10.1109/TIE.2006.874278.

54. Yoon, YH., A Study of Rotor Position Detection and Control Through Low-Cost Circuit Design of SRM. J. Electr. Eng. Technol., 16 (2021), 2817–2827 https://doi.org/10.1007/s42835-021-00813-6.

55. Kang F-S., Park S-J., Park H-W., Hong S-III. and Kim C-U., Linear Grade Encoder for High Resolution Angle Control of SRM Drive, Proceedings of IEEE Region 10 International Conference on Electrical and Electronic Technology. TENCON (Cat. No.01CH37239), 2, 2001, Singapore, 549-555, doi: 10.1109/TENCON.2001.949654.

56. Sahoo N.C., Panda S.K., Dash P.K., A Current Modulation Scheme for Direct Torque Control of Switched Reluctance Motor Using Fuzzy Logic. Mechatronics, 10, 3 (2000) 353-370, https://doi.org/10.1016/S0957-4158(99)00039-2.

8. APPENDIX

Appendix Table 8.1. Torque (table data) - rotor angle (first column) – current (first row) values extracted from FEMM

	1	2	3	4	5	6	7	8	9	10
1	0.0015	0.006	0.0135	0.0241	0.0378	0.0544	0.0741	0.0969	0.1227	0.1515
2	0.0042	0.017	0.0384	0.0685	0.1072	0.1545	0.2104	0.2749	0.3479	0.4294
3	0.0105	0.042	0.0949	0.169	0.2644	0.3807	0.5175	0.674	0.8492	1.0419
4	0.0497	0.1995	0.4382	0.7371	1.0723	1.4275	1.7946	2.1684	2.5385	2.9119
5	0.0683	0.2759	0.6149	1.0318	1.4623	1.8925	2.3187	2.7378	3.1531	3.5667
6	0.0685	0.2776	0.6206	1.0453	1.4936	1.9428	2.3876	2.828	3.2626	3.6917
7	0.0695	0.2819	0.6284	1.053	1.5046	1.9584	2.4104	2.8584	3.301	3.739
8	0.0693	0.2817	0.6273	1.0472	1.4987	1.9549	2.4091	2.8603	3.3074	3.7502
9	0.0697	0.2834	0.6301	1.047	1.4957	1.9536	2.4114	2.8657	3.3157	3.7614
10	0.0694	0.2826	0.6284	1.0424	1.4887	1.946	2.4035	2.8583	3.3093	3.7559
11	0.0708	0.288	0.6373	1.05	1.4921	1.9472	2.4033	2.8569	3.307	3.7528
12	0.0694	0.2826	0.6267	1.0347	1.4729	1.9257	2.38	2.8319	3.2801	3.7235
13	0.0695	0.283	0.6265	1.0316	1.4648	1.914	2.3661	2.8155	3.2589	3.6935
14	0.0706	0.2872	0.6341	1.0387	1.4677	1.911	2.3556	2.7937	3.2199	3.6291
15	0.0695	0.2824	0.622	1.0181	1.4355	1.8633	2.2864	2.6937	3.0811	3.4505
16	0.0702	0.2848	0.6237	1.0108	1.403	1.7881	2.1612	2.5211	2.8688	3.205
17	0.0706	0.2863	0.6208	0.9858	1.3225	1.6375	1.9539	2.2708	2.5841	2.8903
18	0.0691	0.2796	0.6009	0.9187	1.1821	1.4314	1.6882	1.9557	2.2268	2.4956
19	0.0676	0.2732	0.573	0.8223	1.0249	1.2199	1.4172	1.6211	1.8336	2.0519
20	0.0669	0.2693	0.5353	0.7178	0.8707	1.0177	1.1614	1.3042	1.4494	1.599
21	0.0647	0.2589	0.4773	0.6039	0.7124	0.8142	0.9108	1.004	1.0946	1.1835
22	0.056	0.2227	0.3779	0.4521	0.5145	0.5704	0.6216	0.6694	0.7145	0.7569
23	-0.0171	-0.068	-0.113	-0.137	-0.158	-0.177	-0.195	-0.212	-0.227	-0.242
24	-0.0612	-0.244	-0.431	-0.532	-0.619	-0.699	-0.775	-0.847	-0.916	-0.982
25	-0.0648	-0.26	-0.499	-0.652	-0.783	-0.908	-1.029	-1.147	-1.265	-1.384
26	-0.0654	-0.264	-0.543	-0.756	-0.933	-1.105	-1.276	-1.451	-1.631	-1.819
27	-0.0667	-0.27	-0.576	-0.859	-1.091	-1.313	-1.542	-1.781	-2.027	-2.276
28	-0.0683	-0.276	-0.6	-0.943	-1.244	-1.527	-1.817	-2.113	-2.409	-2.699
29	-0.0698	-0.283	-0.616	-0.992	-1.361	-1.714	-2.061	-2.4	-2.732	-3.055
30	-0.0698	-0.283	-0.621	-1.011	-1.418	-1.829	-2.231	-2.615	-2.982	-3.334
31	-0.0689	-0.28	-0.618	-1.016	-1.438	-1.876	-2.312	-2.739	-3.148	-3.538
32	-0.0704	-0.286	-0.63	-1.033	-1.464	-1.91	-2.359	-2.804	-3.241	-3.666
33	-0.0701	-0.285	-0.63	-1.036	-1.473	-1.924	-2.377	-2.827	-3.273	-3.713
34	-0.0688	-0.28	-0.621	-1.028	-1.466	-1.917	-2.37	-2.821	-3.268	-3.711
35	-0.0707	-0.288	-0.637	-1.051	-1.496	-1.952	-2.407	-2.86	-3.309	-3.755
36	-0.0706	-0.287	-0.637	-1.054	-1.502	-1.958	-2.413	-2.865	-3.314	-3.759
37	-0.0703	-0.285	-0.635	-1.054	-1.503	-1.958	-2.412	-2.863	-3.309	-3.753
38	-0.0682	-0.277	-0.62	-1.041	-1.491	-1.943	-2.394	-2.843	-3.287	-3.726
39	-0.0709	-0.287	-0.638	-1.066	-1.517	-1.968	-2.415	-2.858	-3.296	-3.731
40	-0.0723	-0.292	-0.646	-1.075	-1.518	-1.961	-2.401	-2.836	-3.266	-3.691
41	-0.071	-0.286	-0.631	-1.036	-1.447	-1.86	-2.276	-2.681	-3.084	-3.485
42	-0.0193	-0.078	-0.175	-0.312	-0.485	-0.692	-0.93	-1.191	-1.473	-1.77
43	-0.0065	-0.026	-0.059	-0.105	-0.164	-0.236	-0.321	-0.419	-0.53	-0.653
44	-0.0027	-0.011	-0.024	-0.043	-0.067	-0.097	-0.132	-0.173	-0.219	-0.27
45	-0.0005	-0.002	-0.004	-0.008	-0.012	-0.017	-0.023	-0.03	-0.038	-0.047

Appendix Table 8.2. Torque (table data)-rotor angle (first column)-current (first row) values extracted from FEMM

	11	12	13	14	15	16	17	18	19	20
1	0.1833	0.2181	0.2558	0.2965	0.3399	0.3862	0.4353	0.4869	0.5412	0.5981
2	0.5191	0.6171	0.7228	0.8363	0.9572	1.0852	1.2198	1.3607	1.5075	1.66
3	1.2508	1.4737	1.7092	1.9548	2.2094	2.4702	2.7375	3.0079	3.2808	3.5548
4	3.2867	3.6586	4.0184	4.3689	4.7224	5.0792	5.4375	5.7959	6.1524	6.5018
5	3.9778	4.3847	4.7832	5.175	5.5648	5.9484	6.3234	6.6935	7.0613	7.426
6	4.1134	4.5311	4.946	5.3557	5.7583	6.1541	6.544	6.9285	7.3064	7.6795
7	4.1709	4.5971	5.0188	5.4359	5.8465	6.2507	6.6491	7.0415	7.4281	7.8087
8	4.1874	4.6195	5.0485	5.4729	5.8897	6.2994	6.7034	7.1019	7.4939	7.8776
9	4.2017	4.6363	5.0653	5.4884	5.906	6.3183	6.7243	7.1222	7.5095	7.8832
10	4.1974	4.6338	5.0644	5.4886	5.9058	6.3152	6.7149	7.1013	7.4709	7.8223
11	4.1938	4.6295	5.0591	5.4804	5.8908	6.2867	6.6652	7.0257	7.3695	7.6982
12	4.1609	4.5903	5.0087	5.4118	5.7961	6.1618	6.511	6.8457	7.1676	7.4777
13	4.1158	4.5225	4.9107	5.2807	5.6341	5.9728	6.2987	6.6127	6.9152	7.2063
14	4.0186	4.39	4.7457	5.0875	5.417	5.7349	6.0413	6.3363	6.6201	6.8927
15	3.8044	4.145	4.4741	4.7922	5.0989	5.3943	5.6786	5.9519	6.2144	6.4662
16	3.5308	3.8459	4.15	4.4433	4.7258	4.9978	5.2594	5.5104	5.7505	5.9793
17	3.1874	3.4748	3.7522	4.0194	4.2764	4.5231	4.7589	4.9834	5.1953	5.3937
18	2.7587	3.0145	3.2619	3.4999	3.7275	3.9438	4.1473	4.3371	4.5133	4.6756
19	2.2709	2.4862	2.6949	2.8947	3.0833	3.2594	3.4227	3.573	3.7111	3.8383
20	1.7531	1.9092	2.0627	2.2096	2.348	2.4769	2.5961	2.7065	2.8093	2.9056
21	1.2708	1.3561	1.4387	1.5184	1.5948	1.6679	1.7377	1.8047	1.8692	1.9316
22	0.7962	0.8322	0.865	0.8949	0.9224	0.9479	0.9719	0.9949	1.0173	1.0392
23	-0.255	-0.2675	-0.279	-0.289	-0.298	-0.306	-0.314	-0.321	-0.328	-0.335
24	-1.046	-1.1058	-1.162	-1.216	-1.266	-1.314	-1.36	-1.404	-1.448	-1.491
25	-1.506	-1.6276	-1.748	-1.865	-1.977	-2.082	-2.18	-2.272	-2.359	-2.441
26	-2.012	-2.2033	-2.39	-2.568	-2.736	-2.892	-3.036	-3.169	-3.291	-3.405
27	-2.521	-2.7599	-2.992	-3.214	-3.426	-3.626	-3.812	-3.985	-4.145	-4.291
28	-2.981	-3.2552	-3.52	-3.774	-4.019	-4.253	-4.476	-4.687	-4.884	-5.067
29	-3.368	-3.6713	-3.964	-4.246	-4.517	-4.779	-5.03	-5.27	-5.499	-5.716
30	-3.674	-4.003	-4.321	-4.628	-4.923	-5.208	-5.482	-5.746	-5.999	-6.241
31	-3.909	-4.2642	-4.606	-4.937	-5.256	-5.564	-5.86	-6.145	-6.419	-6.682
32	-4.075	-4.4646	-4.836	-5.191	-5.532	-5.86	-6.177	-6.481	-6.775	-7.057
33	-4.145	-4.5664	-4.973	-5.361	-5.73	-6.082	-6.42	-6.744	-7.057	-7.358
34	-4.149	-4.5823	-5.007	-5.421	-5.82	-6.202	-6.565	-6.912	-7.244	-7.563
35	-4.196	-4.6309	-5.06	-5.483	-5.898	-6.303	-6.695	-7.07	-7.428	-7.768
36	-4.2	-4.6348	-5.064	-5.488	-5.905	-6.315	-6.718	-7.112	-7.493	-7.859
37	-4.192	-4.6252	-5.052	-5.474	-5.891	-6.302	-6.706	-7.104	-7.494	-7.873
38	-4.16	-4.5906	-5.016	-5.434	-5.846	-6.252	-6.653	-7.049	-7.439	-7.822
39	-4.16	-4.5825	-4.999	-5.412	-5.819	-6.221	-6.615	-7.003	-7.384	-7.76
40	-4.107	-4.5188	-4.927	-5.33	-5.727	-6.117	-6.499	-6.875	-7.247	-7.616
41	-3.881	-4.2738	-4.661	-5.039	-5.413	-5.788	-6.159	-6.524	-6.88	-7.229
42	-2.076	-2.39	-2.71	-3.033	-3.356	-3.679	-3.997	-4.315	-4.632	-4.947
43	-0.789	-0.9354	-1.093	-1.261	-1.438	-1.624	-1.818	-2.018	-2.224	-2.435
44	-0.327	-0.389	-0.456	-0.528	-0.605	-0.687	-0.774	-0.864	-0.959	-1.058
45	-0.057	-0.068	-0.08	-0.092	-0.106	-0.12	-0.136	-0.152	-0.168	-0.186

Appendix Table 8.3. Torque (table data)-rotor angle (first column)-current (first row) values extracted from FEMM

	21	22	23	24	25	26	27	28	29	30
1	0.6573	0.7187	0.7821	0.8476	0.9149	0.9837	1.0539	1.1251	1.1969	1.2688
2	1.817	1.9778	2.1423	2.3105	2.4812	2.6533	2.8262	2.9996	3.1716	3.34
3	3.8284	4.1015	4.3733	4.6433	4.9111	5.1751	5.4334	5.686	5.9325	6.1706
4	6.8369	7.162	7.4818	7.798	8.1091	8.4151	8.7154	9.007	9.2865	9.5512
5	7.7858	8.1403	8.4876	8.8262	9.1566	9.4782	9.7879	10.083	10.362	10.626
6	8.048	8.4112	8.7678	9.1158	9.4527	9.7751	10.081	10.37	10.644	10.905
7	8.1826	8.5486	8.9042	9.2464	9.5719	9.8799	10.172	10.449	10.714	10.968
8	8.2507	8.6104	8.9538	9.2803	9.5909	9.8867	10.169	10.44	10.699	10.947
9	8.2406	8.5805	8.9044	9.2138	9.5102	9.7947	10.067	10.328	10.578	10.817
10	8.1569	8.4763	8.7826	9.0772	9.3608	9.6333	9.895	10.146	10.386	10.616
11	8.0135	8.3166	8.6081	8.888	9.1567	9.4145	9.6618	9.8987	10.125	10.342
12	7.7761	8.0626	8.3377	8.6016	8.8546	9.0971	9.3292	9.5506	9.7611	9.96
13	7.4863	7.7555	8.014	8.2619	8.4992	8.7256	8.9408	9.1438	9.3339	9.5108
14	7.1545	7.4054	7.6456	7.8747	8.0923	8.2974	8.4892	8.6676	8.8326	8.9848
15	6.7071	6.9369	7.1548	7.3599	7.5514	7.7294	7.8938	8.0453	8.1854	8.3156
16	6.1958	6.399	6.5884	6.7641	6.9261	7.0755	7.2136	7.3422	7.4627	7.5768
17	5.5782	5.7489	5.9061	6.051	6.1851	6.3101	6.4275	6.5388	6.6448	6.7463
18	4.825	4.9626	5.0901	5.209	5.321	5.4273	5.5287	5.6259	5.7195	5.81
19	3.9562	4.0663	4.17	4.2685	4.3625	4.4528	4.5398	4.624	4.7057	4.7852
20	2.9966	3.0833	3.1663	3.2461	3.3232	3.3979	3.4706	3.5414	3.6106	3.6783
21	1.9923	2.0514	2.1092	2.1657	2.2212	2.2757	2.3294	2.3823	2.4344	2.486
22	1.0608	1.0823	1.1038	1.1253	1.147	1.1689	1.191	1.2134	1.236	1.2589
23	-0.342	-0.349	-0.3553	-0.362	-0.368	-0.375	-0.382	-0.389	-0.396	-0.403
24	-1.533	-1.576	-1.6178	-1.66	-1.701	-1.743	-1.784	-1.825	-1.866	-1.907
25	-2.52	-2.596	-2.669	-2.74	-2.809	-2.876	-2.941	-3.006	-3.069	-3.13
26	-3.511	-3.611	-3.7059	-3.797	-3.884	-3.968	-4.049	-4.128	-4.205	-4.28
27	-4.426	-4.551	-4.6682	-4.778	-4.882	-4.982	-5.077	-5.169	-5.258	-5.344
28	-5.237	-5.393	-5.5368	-5.67	-5.794	-5.911	-6.021	-6.127	-6.228	-6.325
29	-5.92	-6.109	-6.2852	-6.447	-6.597	-6.735	-6.864	-6.984	-7.098	-7.207
30	-6.472	-6.691	-6.898	-7.091	-7.27	-7.436	-7.589	-7.73	-7.862	-7.984
31	-6.934	-7.176	-7.4069	-7.627	-7.834	-8.028	-8.208	-8.376	-8.53	-8.672
32	-7.329	-7.59	-7.8405	-8.081	-8.31	-8.529	-8.735	-8.928	-9.108	-9.274
33	-7.648	-7.927	-8.1944	-8.451	-8.698	-8.933	-9.158	-9.372	-9.574	-9.764
34	-7.87	-8.166	-8.4495	-8.722	-8.984	-9.235	-9.476	-9.706	-9.925	-10.13
35	-8.093	-8.404	-8.7031	-8.99	-9.266	-9.531	-9.785	-10.03	-10.26	-10.49
36	-8.206	-8.536	-8.85	-9.151	-9.439	-9.716	-9.982	-10.24	-10.48	-10.72
37	-8.24	-8.59	-8.9232	-9.24	-9.543	-9.833	-10.11	-10.38	-10.63	-10.87
38	-8.194	-8.556	-8.906	-9.24	-9.558	-9.861	-10.15	-10.42	-10.69	-10.94
39	-8.13	-8.495	-8.8525	-9.198	-9.529	-9.843	-10.14	-10.42	-10.69	-10.95
40	-7.978	-8.335	-8.6843	-9.024	-9.353	-9.671	-9.977	-10.27	-10.55	-10.81
41	-7.574	-7.917	-8.2541	-8.583	-8.904	-9.215	-9.517	-9.808	-10.09	-10.35
42	-5.259	-5.562	-5.8588	-6.153	-6.447	-6.738	-7.023	-7.299	-7.562	-7.81
43	-2.651	-2.869	-3.0891	-3.311	-3.531	-3.75	-3.969	-4.187	-4.4	-4.607
44	-1.161	-1.267	-1.3762	-1.488	-1.602	-1.719	-1.836	-1.955	-2.073	-2.191
45	-0.204	-0.222	-0.2415	-0.261	-0.282	-0.303	-0.324	-0.346	-0.367	-0.39

Appendix Table 8.4. Torque (table data)-rotor angle (first column)-current (first row) values extracted from FEMM

	31	32	33	34	35	36	37	38	39	40
1	1.3402	1.41	1.4771	1.5415	1.6035	1.6631	1.7202	1.7746	1.8264	1.8758
2	3.503	3.6593	3.8087	3.951	4.0867	4.2164	4.3402	4.4579	4.5696	4.6753
3	6.3966	6.6092	6.809	6.9975	7.1764	7.3467	7.5087	7.6626	7.8088	7.9474
4	9.8008	10.036	10.257	10.468	10.667	10.857	11.037	11.207	11.369	11.522
5	10.876	11.114	11.341	11.557	11.761	11.956	12.141	12.317	12.484	12.643
6	11.154	11.392	11.619	11.835	12.041	12.237	12.424	12.601	12.769	12.927
7	11.211	11.444	11.667	11.88	12.084	12.279	12.464	12.639	12.804	12.958
8	11.185	11.412	11.629	11.837	12.034	12.222	12.4	12.566	12.72	12.863
9	11.046	11.264	11.473	11.671	11.86	12.037	12.202	12.356	12.498	12.628
10	10.835	11.044	11.242	11.428	11.603	11.765	11.914	12.052	12.179	12.297
11	10.547	10.741	10.922	11.09	11.246	11.389	11.522	11.644	11.759	11.867
12	10.146	10.32	10.48	10.628	10.765	10.891	11.01	11.122	11.227	11.329
13	9.6746	9.8256	9.965	10.094	10.215	10.329	10.438	10.541	10.64	10.736
14	9.1254	9.2559	9.378	9.4932	9.6026	9.7071	9.8074	9.9041	9.9975	10.088
15	8.4376	8.5528	8.6623	8.767	8.8675	8.9644	9.0581	9.149	9.2374	9.3235
16	7.6853	7.7891	7.8888	7.985	8.0782	8.1685	8.2564	8.3421	8.4259	8.5079
17	6.8439	6.9382	7.0295	7.1182	7.2045	7.2887	7.3711	7.4518	7.531	7.6088
18	5.8978	5.9831	6.0663	6.1475	6.2271	6.3051	6.3817	6.4571	6.5314	6.6047
19	4.8628	4.9387	5.0131	5.0862	5.158	5.2288	5.2986	5.3676	5.4358	5.5034
20	3.7447	3.81	3.8743	3.9377	4.0002	4.062	4.1232	4.1838	4.244	4.3037
21	2.537	2.5875	2.6376	2.6873	2.7367	2.7857	2.8345	2.883	2.9313	2.9794
22	1.2821	1.3056	1.3294	1.3534	1.3778	1.4024	1.4273	1.4524	1.4777	1.5033
23	-0.41	-0.417	-0.424	-0.4317	-0.439	-0.447	-0.455	-0.464	-0.472	-0.481
24	-1.948	-1.988	-2.029	-2.0691	-2.11	-2.15	-2.19	-2.231	-2.271	-2.311
25	-3.191	-3.251	-3.31	-3.369	-3.427	-3.484	-3.541	-3.597	-3.653	-3.709
26	-4.353	-4.425	-4.496	-4.5655	-4.634	-4.701	-4.768	-4.834	-4.9	-4.964
27	-5.428	-5.509	-5.589	-5.6674	-5.744	-5.82	-5.894	-5.967	-6.039	-6.11
28	-6.418	-6.509	-6.597	-6.6828	-6.766	-6.848	-6.929	-7.007	-7.085	-7.161
29	-7.311	-7.411	-7.507	-7.6004	-7.691	-7.779	-7.865	-7.949	-8.031	-8.111
30	-8.1	-8.211	-8.316	-8.4171	-8.515	-8.609	-8.7	-8.789	-8.875	-8.96
31	-8.804	-8.928	-9.044	-9.1544	-9.26	-9.361	-9.458	-9.553	-9.644	-9.733
32	-9.428	-9.569	-9.701	-9.8233	-9.939	-10.05	-10.15	-10.25	-10.35	-10.44
33	-9.941	-10.1	-10.26	-10.395	-10.52	-10.64	-10.76	-10.87	-10.97	-11.07
34	-10.33	-10.52	-10.69	-10.849	-11	-11.13	-11.26	-11.38	-11.49	-11.59
35	-10.7	-10.9	-11.09	-11.27	-11.44	-11.59	-11.73	-11.86	-11.98	-12.1
36	-10.94	-11.15	-11.36	-11.553	-11.74	-11.91	-12.06	-12.21	-12.35	-12.47
37	-11.11	-11.33	-11.54	-11.745	-11.94	-12.12	-12.29	-12.45	-12.6	-12.74
38	-11.18	-11.41	-11.62	-11.834	-12.03	-12.22	-12.41	-12.58	-12.74	-12.88
39	-11.2	-11.43	-11.65	-11.868	-12.07	-12.26	-12.45	-12.62	-12.79	-12.95
40	-11.06	-11.3	-11.53	-11.742	-11.95	-12.14	-12.33	-12.5	-12.67	-12.83
41	-10.6	-10.83	-11.06	-11.272	-11.47	-11.67	-11.85	-12.03	-12.19	-12.35
42	-8.045	-8.267	-8.477	-8.6757	-8.865	-9.046	-9.218	-9.382	-9.537	-9.685
43	-4.803	-4.988	-5.164	-5.3312	-5.491	-5.644	-5.789	-5.927	-6.058	-6.181
44	-2.307	-2.42	-2.526	-2.628	-2.725	-2.819	-2.909	-2.994	-3.076	-3.153
45	-0.411	-0.432	-0.453	-0.4726	-0.492	-0.51	-0.527	-0.544	-0.56	-0.575

Appendix Table 8.5. Torque (table data)-rotor angle (first column)-current (first row) values extracted from FEMM

	41	42	43	44	45	46	47	48	49	50
1	1.9229	1.9676	2.0101	2.0502	2.0877	2.1226	2.1549	2.1844	2.2114	2.236
2	4.7751	4.8692	4.9578	5.0409	5.1184	5.1899	5.2555	5.3154	5.3698	5.4197
3	8.0787	8.2027	8.3193	8.4283	8.5292	8.6219	8.7065	8.7835	8.8539	8.9187
4	11.667	11.804	11.933	12.052	12.162	12.263	12.355	12.44	12.518	12.59
5	12.792	12.933	13.063	13.184	13.294	13.395	13.489	13.575	13.656	13.732
6	13.075	13.213	13.34	13.456	13.563	13.662	13.754	13.841	13.923	14.001
7	13.101	13.233	13.353	13.465	13.568	13.664	13.754	13.841	13.923	14.002
8	12.995	13.116	13.228	13.332	13.43	13.523	13.611	13.696	13.778	13.857
9	12.748	12.86	12.965	13.064	13.158	13.248	13.335	13.419	13.499	13.578
10	12.407	12.512	12.611	12.705	12.796	12.884	12.968	13.05	13.13	13.208
11	11.97	12.068	12.162	12.252	12.34	12.425	12.507	12.587	12.666	12.742
12	11.426	11.519	11.609	11.697	11.782	11.865	11.945	12.024	12.101	12.177
13	10.828	10.917	11.004	11.089	11.171	11.252	11.331	11.409	11.485	11.56
14	10.176	10.262	10.345	10.427	10.507	10.586	10.663	10.739	10.814	10.888
15	9.4076	9.4899	9.5705	9.6497	9.7276	9.8042	9.8797	9.9543	10.028	10.101
16	8.5883	8.6673	8.7451	8.8216	8.8972	8.9717	9.0455	9.1184	9.1906	9.2621
17	7.6855	7.761	7.8356	7.9093	7.9822	8.0543	8.1258	8.1966	8.2667	8.3363
18	6.6772	6.7488	6.8198	6.8901	6.9597	7.0288	7.0972	7.1652	7.2326	7.2995
19	5.5703	5.6367	5.7026	5.768	5.833	5.8974	5.9615	6.025	6.0882	6.1509
20	4.3629	4.4218	4.4803	4.5384	4.5961	4.6535	4.7105	4.7672	4.8235	4.8795
21	3.0273	3.0749	3.1223	3.1694	3.2163	3.2629	3.3092	3.3552	3.4009	3.4463
22	1.5289	1.5547	1.5806	1.6066	1.6327	1.6587	1.6848	1.7108	1.7367	1.7626
23	-0.49	-0.499	-0.509	-0.519	-0.5284	-0.538	-0.549	-0.559	-0.569	-0.58
24	-2.351	-2.391	-2.431	-2.471	-2.511	-2.551	-2.59	-2.629	-2.668	-2.707
25	-3.764	-3.819	-3.873	-3.927	-3.9813	-4.035	-4.088	-4.141	-4.193	-4.246
26	-5.029	-5.093	-5.156	-5.219	-5.2811	-5.343	-5.405	-5.466	-5.527	-5.587
27	-6.181	-6.251	-6.32	-6.389	-6.4571	-6.525	-6.592	-6.658	-6.724	-6.79
28	-7.236	-7.31	-7.384	-7.456	-7.5283	-7.6	-7.67	-7.74	-7.809	-7.878
29	-8.19	-8.268	-8.345	-8.42	-8.4949	-8.569	-8.642	-8.714	-8.786	-8.857
30	-9.042	-9.123	-9.203	-9.281	-9.3579	-9.434	-9.509	-9.583	-9.656	-9.728
31	-9.819	-9.903	-9.986	-10.07	-10.146	-10.22	-10.3	-10.38	-10.45	-10.52
32	-10.53	-10.62	-10.71	-10.79	-10.87	-10.95	-11.03	-11.1	-11.18	-11.25
33	-11.16	-11.26	-11.34	-11.43	-11.515	-11.6	-11.68	-11.76	-11.83	-11.91
34	-11.69	-11.79	-11.88	-11.97	-12.059	-12.14	-12.23	-12.31	-12.38	-12.46
35	-12.2	-12.3	-12.4	-12.49	-12.583	-12.67	-12.75	-12.83	-12.91	-12.99
36	-12.59	-12.69	-12.8	-12.89	-12.987	-13.08	-13.16	-13.24	-13.32	-13.4
37	-12.87	-12.98	-13.09	-13.19	-13.286	-13.38	-13.46	-13.55	-13.63	-13.71
38	-13.02	-13.15	-13.26	-13.37	-13.47	-13.56	-13.65	-13.74	-13.82	-13.9
39	-13.09	-13.23	-13.35	-13.46	-13.568	-13.66	-13.76	-13.84	-13.92	-14
40	-12.98	-13.12	-13.25	-13.37	-13.476	-13.58	-13.67	-13.76	-13.84	-13.91
41	-12.49	-12.63	-12.76	-12.88	-12.991	-13.09	-13.18	-13.27	-13.35	-13.42
42	-9.825	-9.956	-10.08	-10.19	-10.298	-10.39	-10.48	-10.56	-10.64	-10.7
43	-6.297	-6.405	-6.508	-6.603	-6.6919	-6.774	-6.849	-6.917	-6.98	-7.037
44	-3.225	-3.293	-3.358	-3.418	-3.475	-3.528	-3.576	-3.621	-3.661	-3.699
45	-0.589	-0.602	-0.615	-0.627	-0.6377	-0.648	-0.657	-0.665	-0.673	-0.68

Appendix Table 8.6. Flux (table data)-rotor angle (first column)-current (first row) values extracted from FEMM

	1	2	3	4	5	6	7	8	9	10
1	2.69E-04	5.40E-04	8.11E-04	1.08E-03	1.35E-03	1.62E-03	0.0019	0.0022	0.0024	0.0027
2	2.76E-04	5.53E-04	8.31E-04	1.11E-03	1.39E-03	1.67E-03	0.0019	0.0022	0.0025	0.0028
3	2.93E-04	5.86E-04	8.81E-04	1.18E-03	1.47E-03	1.77E-03	0.0021	0.0024	0.0026	0.0029
4	3.47E-04	6.95E-04	1.04E-03	1.38E-03	1.72E-03	0.00204	0.0024	0.0027	0.003	0.0033
5	5.09E-04	1.02E-03	1.49E-03	1.87E-03	0.00221	0.00254	0.0029	0.0032	0.0035	0.0038
6	6.79E-04	1.36E-03	1.97E-03	0.00241	0.00276	0.00308	0.0034	0.0037	0.004	0.0043
7	8.47E-04	1.70E-03	0.00245	0.00295	0.00331	0.00363	0.0039	0.0042	0.0045	0.0048
8	1.02E-03	0.00205	0.00294	0.00349	0.00386	0.00419	0.0045	0.0048	0.0051	0.0054
9	1.19E-03	0.00239	0.00341	0.00403	0.00442	0.00474	0.005	0.0053	0.0056	0.0059
10	1.36E-03	0.00274	0.00389	0.00456	0.00497	0.0053	0.0056	0.0059	0.0062	0.0064
11	1.53E-03	0.00309	0.00437	0.00508	0.00552	0.00585	0.0062	0.0064	0.0067	0.007
12	1.71E-03	0.00344	0.00484	0.0056	0.00607	0.00641	0.0067	0.007	0.0073	0.0075
13	0.00188	0.00378	0.00532	0.00612	0.00662	0.00696	0.0073	0.0075	0.0078	0.008
14	0.00205	0.00413	0.00579	0.00663	0.00715	0.00751	0.0078	0.0081	0.0083	0.0085
15	0.00223	0.00448	0.00625	0.00713	0.00768	0.00804	0.0083	0.0086	0.0088	0.009
16	0.0024	0.00482	0.00671	0.00762	0.00817	0.00853	0.0088	0.009	0.0092	0.0094
17	0.00257	0.00517	0.00716	0.00808	0.0086	0.00894	0.0092	0.0094	0.0096	0.0097
18	0.00274	0.0055	0.00759	0.00847	0.00894	0.00926	0.0095	0.0097	0.0099	0.0101
19	0.00291	0.00584	0.00798	0.00876	0.00919	0.00952	0.0098	0.01	0.0102	0.0103
20	0.00308	0.00616	0.0083	0.00898	0.00939	0.00971	0.01	0.0102	0.0104	0.0105
21	0.00324	0.00647	0.00852	0.00914	0.00953	0.00984	0.0101	0.0103	0.0105	0.0106
22	0.00339	0.00676	0.00866	0.00924	0.00963	0.00993	0.0102	0.0104	0.0106	0.0107
23	0.00345	0.00685	0.0087	0.00927	0.00965	0.00995	0.0102	0.0104	0.0106	0.0107
24	0.00332	0.00663	0.0086	0.00919	0.00959	0.00989	0.0101	0.0103	0.0105	0.0107
25	0.00317	0.00633	0.00842	0.00906	0.00947	0.00978	0.01	0.0102	0.0104	0.0106
26	0.00301	0.00602	0.00816	0.00888	0.0093	0.00962	0.0099	0.0101	0.0103	0.0104
27	0.00284	0.0057	0.0078	0.00862	0.00907	0.00939	0.0096	0.0099	0.01	0.0102
28	0.00267	0.00537	0.00739	0.00828	0.00877	0.0091	0.0093	0.0096	0.0097	0.0099
29	0.0025	0.00503	0.00696	0.00786	0.00839	0.00873	0.009	0.0092	0.0094	0.0096
30	0.00233	0.00469	0.0065	0.00738	0.00792	0.00828	0.0085	0.0088	0.009	0.0092
31	0.00216	0.00435	0.00604	0.00688	0.00741	0.00776	0.0081	0.0083	0.0085	0.0088
32	0.00199	0.004	0.00558	0.00638	0.00688	0.00722	0.0075	0.0078	0.008	0.0083
33	0.00182	0.00366	0.00511	0.00587	0.00634	0.00668	0.007	0.0072	0.0075	0.0078
34	0.00164	0.0033	0.00463	0.00535	0.00579	0.00612	0.0064	0.0067	0.007	0.0072
35	1.47E-03	0.00295	0.00415	0.00482	0.00524	0.00557	0.0059	0.0061	0.0064	0.0067
36	1.29E-03	0.0026	0.00368	0.0043	0.00469	0.00501	0.0053	0.0056	0.0059	0.0061
37	1.12E-03	0.00225	0.0032	0.00376	0.00413	0.00445	0.0048	0.005	0.0053	0.0056
38	9.45E-04	0.0019	0.00271	0.00322	0.00358	0.0039	0.0042	0.0045	0.0048	0.0051
39	7.73E-04	0.00155	0.00223	0.00268	0.00303	0.00335	0.0037	0.004	0.0043	0.0046
40	6.00E-04	1.20E-03	0.00174	0.00214	0.00248	0.00281	0.0031	0.0034	0.0037	0.004
41	4.28E-04	8.55E-04	0.00125	0.00161	0.00195	0.00228	0.0026	0.0029	0.0032	0.0035
42	3.09E-04	6.20E-04	9.32E-04	0.00124	0.00155	0.00186	0.0022	0.0025	0.0028	0.0031
43	2.82E-04	5.66E-04	8.50E-04	1.13E-03	1.42E-03	0.0017	0.002	0.0023	0.0026	0.0028
44	2.72E-04	5.45E-04	8.19E-04	1.09E-03	1.37E-03	0.00164	0.0019	0.0022	0.0025	0.0027
45	2.68E-04	5.38E-04	8.08E-04	1.08E-03	1.35E-03	1.62E-03	0.0019	0.0022	0.0024	0.0027

Appendix Table 8.7. Flux (table data)-rotor angle(first column)-current (first row) values extracted from FEMM

	11	12	13	14	15	16	17	18	19	20
1	0.003	0.0033	0.0035	0.0038	0.0041	0.0043	0.0046	0.0049	0.0052	0.0054
2	0.0031	0.0033	0.0036	0.0039	0.0042	0.0044	0.0047	0.005	0.0053	0.0055
3	0.0032	0.0035	0.0038	0.0041	0.0044	0.0047	0.005	0.0052	0.0055	0.0058
4	0.0036	0.0039	0.0042	0.0045	0.0048	0.0051	0.0053	0.0056	0.0059	0.0062
5	0.0041	0.0044	0.0047	0.0049	0.0052	0.0055	0.0058	0.0061	0.0063	0.0066
6	0.0046	0.0049	0.0052	0.0054	0.0057	0.006	0.0063	0.0065	0.0068	0.007
7	0.0051	0.0054	0.0057	0.0059	0.0062	0.0065	0.0067	0.007	0.0073	0.0075
8	0.0056	0.0059	0.0062	0.0064	0.0067	0.007	0.0072	0.0075	0.0077	0.008
9	0.0062	0.0064	0.0067	0.007	0.0072	0.0075	0.0077	0.0079	0.0082	0.0084
10	0.0067	0.007	0.0072	0.0075	0.0077	0.008	0.0082	0.0084	0.0086	0.0088
11	0.0072	0.0075	0.0077	0.008	0.0082	0.0084	0.0086	0.0088	0.009	0.0092
12	0.0078	0.008	0.0082	0.0085	0.0087	0.0089	0.0091	0.0092	0.0094	0.0096
13	0.0083	0.0085	0.0087	0.0089	0.0091	0.0093	0.0094	0.0096	0.0098	0.0099
14	0.0088	0.0089	0.0091	0.0093	0.0095	0.0096	0.0098	0.0099	0.0101	0.0102
15	0.0092	0.0093	0.0095	0.0097	0.0098	0.01	0.0101	0.0102	0.0104	0.0105
16	0.0096	0.0097	0.0099	0.01	0.0101	0.0103	0.0104	0.0105	0.0106	0.0107
17	0.0099	0.01	0.0102	0.0103	0.0104	0.0105	0.0106	0.0107	0.0108	0.0109
18	0.0102	0.0103	0.0104	0.0106	0.0107	0.0108	0.0109	0.0109	0.011	0.0111
19	0.0105	0.0106	0.0107	0.0108	0.0109	0.0109	0.011	0.0111	0.0111	0.0112
20	0.0106	0.0108	0.0109	0.0109	0.011	0.0111	0.0111	0.0112	0.0112	0.0113
21	0.0108	0.0109	0.011	0.011	0.0111	0.0112	0.0112	0.0112	0.0113	0.0113
22	0.0108	0.0109	0.011	0.0111	0.0111	0.0112	0.0112	0.0113	0.0113	0.0113
23	0.0108	0.0109	0.011	0.0111	0.0112	0.0112	0.0112	0.0113	0.0113	0.0114
24	0.0108	0.0109	0.011	0.0111	0.0111	0.0112	0.0112	0.0113	0.0113	0.0113
25	0.0107	0.0108	0.0109	0.011	0.0111	0.0111	0.0112	0.0112	0.0113	0.0113
26	0.0106	0.0107	0.0108	0.0109	0.0109	0.011	0.0111	0.0111	0.0112	0.0112
27	0.0103	0.0104	0.0106	0.0107	0.0108	0.0109	0.0109	0.011	0.0111	0.0111
28	0.01	0.0102	0.0103	0.0104	0.0105	0.0106	0.0107	0.0108	0.0109	0.011
29	0.0097	0.0099	0.01	0.0101	0.0103	0.0104	0.0105	0.0106	0.0107	0.0108
30	0.0094	0.0095	0.0097	0.0098	0.01	0.0101	0.0102	0.0104	0.0105	0.0106
31	0.009	0.0091	0.0093	0.0095	0.0096	0.0098	0.0099	0.0101	0.0102	0.0103
32	0.0085	0.0087	0.0089	0.0091	0.0093	0.0094	0.0096	0.0098	0.0099	0.01
33	0.008	0.0082	0.0085	0.0087	0.0089	0.0091	0.0092	0.0094	0.0096	0.0097
34	0.0075	0.0077	0.008	0.0082	0.0084	0.0086	0.0088	0.009	0.0092	0.0094
35	0.0069	0.0072	0.0075	0.0077	0.0079	0.0082	0.0084	0.0086	0.0088	0.009
36	0.0064	0.0067	0.0069	0.0072	0.0074	0.0077	0.0079	0.0082	0.0084	0.0086
37	0.0059	0.0062	0.0064	0.0067	0.0069	0.0072	0.0074	0.0077	0.0079	0.0082
38	0.0054	0.0056	0.0059	0.0062	0.0064	0.0067	0.007	0.0072	0.0075	0.0077
39	0.0048	0.0051	0.0054	0.0057	0.0059	0.0062	0.0065	0.0067	0.007	0.0073
40	0.0043	0.0046	0.0049	0.0052	0.0055	0.0057	0.006	0.0063	0.0065	0.0068
41	0.0038	0.0041	0.0044	0.0047	0.005	0.0053	0.0056	0.0058	0.0061	0.0064
42	0.0034	0.0037	0.004	0.0043	0.0046	0.0049	0.0051	0.0054	0.0057	0.006
43	0.0031	0.0034	0.0037	0.004	0.0043	0.0045	0.0048	0.0051	0.0054	0.0057
44	0.003	0.0033	0.0036	0.0038	0.0041	0.0044	0.0047	0.0049	0.0052	0.0055
45	0.003	0.0032	0.0035	0.0038	0.0041	0.0043	0.0046	0.0049	0.0051	0.0054

Appendix Table 8.8. Flux (table data)-rotor angle(first column)-current (first row) values extracted from FEMM

	21	22	23	24	25	26	27	28	29	30
1	0.0057	0.006	0.0062	0.0065	0.0068	0.007	0.0073	0.0076	0.0078	0.0081
2	0.0058	0.0061	0.0064	0.0066	0.0069	0.0072	0.0074	0.0077	0.008	0.0082
3	0.0061	0.0064	0.0066	0.0069	0.0072	0.0074	0.0077	0.008	0.0082	0.0085
4	0.0065	0.0067	0.007	0.0073	0.0075	0.0078	0.008	0.0083	0.0085	0.0088
5	0.0069	0.0071	0.0074	0.0077	0.0079	0.0082	0.0084	0.0086	0.0089	0.0091
6	0.0073	0.0076	0.0078	0.0081	0.0083	0.0085	0.0088	0.009	0.0092	0.0093
7	0.0078	0.008	0.0082	0.0085	0.0087	0.0089	0.0091	0.0093	0.0095	0.0096
8	0.0082	0.0084	0.0086	0.0089	0.0091	0.0092	0.0094	0.0096	0.0097	0.0099
9	0.0086	0.0088	0.009	0.0092	0.0094	0.0096	0.0097	0.0099	0.01	0.0102
10	0.009	0.0092	0.0094	0.0095	0.0097	0.0099	0.01	0.0101	0.0103	0.0104
11	0.0094	0.0096	0.0097	0.0099	0.01	0.0101	0.0103	0.0104	0.0105	0.0106
12	0.0097	0.0099	0.01	0.0102	0.0103	0.0104	0.0105	0.0106	0.0107	0.0108
13	0.01	0.0102	0.0103	0.0104	0.0105	0.0106	0.0107	0.0108	0.0109	0.011
14	0.0103	0.0104	0.0106	0.0107	0.0108	0.0108	0.0109	0.011	0.0111	0.0111
15	0.0106	0.0107	0.0108	0.0109	0.0109	0.011	0.0111	0.0111	0.0112	0.0112
16	0.0108	0.0109	0.011	0.011	0.0111	0.0111	0.0112	0.0112	0.0113	0.0113
17	0.011	0.011	0.0111	0.0112	0.0112	0.0112	0.0113	0.0113	0.0113	0.0114
18	0.0111	0.0112	0.0112	0.0113	0.0113	0.0113	0.0114	0.0114	0.0114	0.0114
19	0.0112	0.0113	0.0113	0.0113	0.0114	0.0114	0.0114	0.0114	0.0115	0.0115
20	0.0113	0.0113	0.0114	0.0114	0.0114	0.0114	0.0115	0.0115	0.0115	0.0115
21	0.0113	0.0114	0.0114	0.0114	0.0115	0.0115	0.0115	0.0115	0.0115	0.0116
22	0.0114	0.0114	0.0114	0.0115	0.0115	0.0115	0.0115	0.0115	0.0116	0.0116
23	0.0114	0.0114	0.0114	0.0115	0.0115	0.0115	0.0115	0.0116	0.0116	0.0116
24	0.0114	0.0114	0.0114	0.0114	0.0115	0.0115	0.0115	0.0115	0.0116	0.0116
25	0.0113	0.0113	0.0114	0.0114	0.0114	0.0115	0.0115	0.0115	0.0115	0.0116
26	0.0113	0.0113	0.0113	0.0114	0.0114	0.0114	0.0114	0.0115	0.0115	0.0115
27	0.0112	0.0112	0.0113	0.0113	0.0113	0.0114	0.0114	0.0114	0.0114	0.0115
28	0.011	0.0111	0.0112	0.0112	0.0112	0.0113	0.0113	0.0113	0.0114	0.0114
29	0.0109	0.011	0.011	0.0111	0.0111	0.0112	0.0112	0.0113	0.0113	0.0113
30	0.0107	0.0108	0.0109	0.0109	0.011	0.0111	0.0111	0.0112	0.0112	0.0113
31	0.0104	0.0106	0.0107	0.0108	0.0108	0.0109	0.011	0.0111	0.0111	0.0112
32	0.0102	0.0103	0.0104	0.0105	0.0106	0.0107	0.0108	0.0109	0.011	0.0111
33	0.0099	0.01	0.0101	0.0103	0.0104	0.0105	0.0106	0.0107	0.0108	0.0109
34	0.0095	0.0097	0.0098	0.01	0.0101	0.0103	0.0104	0.0105	0.0106	0.0107
35	0.0092	0.0094	0.0095	0.0097	0.0098	0.01	0.0101	0.0103	0.0104	0.0105
36	0.0088	0.009	0.0092	0.0094	0.0095	0.0097	0.0098	0.01	0.0101	0.0103
37	0.0084	0.0086	0.0088	0.009	0.0092	0.0094	0.0096	0.0097	0.0099	0.01
38	0.008	0.0082	0.0084	0.0086	0.0089	0.0091	0.0092	0.0094	0.0096	0.0098
39	0.0075	0.0078	0.008	0.0083	0.0085	0.0087	0.0089	0.0091	0.0093	0.0095
40	0.0071	0.0073	0.0076	0.0078	0.0081	0.0083	0.0086	0.0088	0.009	0.0092
41	0.0067	0.0069	0.0072	0.0074	0.0077	0.008	0.0082	0.0085	0.0087	0.0089
42	0.0063	0.0065	0.0068	0.0071	0.0073	0.0076	0.0079	0.0081	0.0084	0.0086
43	0.0059	0.0062	0.0065	0.0068	0.007	0.0073	0.0076	0.0078	0.0081	0.0083
44	0.0057	0.006	0.0063	0.0066	0.0068	0.0071	0.0074	0.0076	0.0079	0.0081
45	0.0057	0.0059	0.0062	0.0065	0.0067	0.007	0.0073	0.0075	0.0078	0.0081

Appendix Table 8.9. Flux (table data)-rotor angle(first column)-current (first row) values extracted from FEMM

	31	32	33	34	35	36	37	38	39	40
1	0.0083	0.0086	0.0088	0.009	0.0092	0.0094	0.0096	0.0098	0.01	0.0101
2	0.0085	0.0087	0.0089	0.0091	0.0093	0.0095	0.0097	0.0099	0.01	0.0102
3	0.0087	0.0089	0.0091	0.0093	0.0095	0.0097	0.0099	0.01	0.0102	0.0103
4	0.009	0.0092	0.0094	0.0095	0.0097	0.0099	0.01	0.0102	0.0103	0.0105
5	0.0092	0.0094	0.0096	0.0098	0.0099	0.0101	0.0102	0.0104	0.0105	0.0106
6	0.0095	0.0097	0.0099	0.01	0.0102	0.0103	0.0104	0.0105	0.0107	0.0108
7	0.0098	0.0099	0.0101	0.0102	0.0104	0.0105	0.0106	0.0107	0.0108	0.0109
8	0.01	0.0102	0.0103	0.0104	0.0106	0.0107	0.0108	0.0109	0.011	0.011
9	0.0103	0.0104	0.0105	0.0106	0.0107	0.0108	0.0109	0.011	0.0111	0.0111
10	0.0105	0.0106	0.0107	0.0108	0.0109	0.011	0.0111	0.0111	0.0112	0.0112
11	0.0107	0.0108	0.0109	0.011	0.0111	0.0111	0.0112	0.0112	0.0113	0.0113
12	0.0109	0.011	0.0111	0.0111	0.0112	0.0112	0.0113	0.0113	0.0113	0.0114
13	0.0111	0.0111	0.0112	0.0112	0.0113	0.0113	0.0113	0.0114	0.0114	0.0114
14	0.0112	0.0112	0.0113	0.0113	0.0113	0.0114	0.0114	0.0114	0.0115	0.0115
15	0.0113	0.0113	0.0113	0.0114	0.0114	0.0114	0.0115	0.0115	0.0115	0.0115
16	0.0113	0.0114	0.0114	0.0114	0.0115	0.0115	0.0115	0.0115	0.0116	0.0116
17	0.0114	0.0114	0.0115	0.0115	0.0115	0.0115	0.0116	0.0116	0.0116	0.0116
18	0.0115	0.0115	0.0115	0.0115	0.0116	0.0116	0.0116	0.0116	0.0116	0.0117
19	0.0115	0.0115	0.0116	0.0116	0.0116	0.0116	0.0116	0.0117	0.0117	0.0117
20	0.0116	0.0116	0.0116	0.0116	0.0116	0.0117	0.0117	0.0117	0.0117	0.0117
21	0.0116	0.0116	0.0116	0.0117	0.0117	0.0117	0.0117	0.0117	0.0118	0.0118
22	0.0116	0.0116	0.0117	0.0117	0.0117	0.0117	0.0117	0.0118	0.0118	0.0118
23	0.0116	0.0116	0.0117	0.0117	0.0117	0.0117	0.0117	0.0118	0.0118	0.0118
24	0.0116	0.0116	0.0116	0.0117	0.0117	0.0117	0.0117	0.0117	0.0118	0.0118
25	0.0116	0.0116	0.0116	0.0116	0.0117	0.0117	0.0117	0.0117	0.0117	0.0118
26	0.0115	0.0116	0.0116	0.0116	0.0116	0.0116	0.0117	0.0117	0.0117	0.0117
27	0.0115	0.0115	0.0115	0.0116	0.0116	0.0116	0.0116	0.0116	0.0117	0.0117
28	0.0114	0.0115	0.0115	0.0115	0.0115	0.0116	0.0116	0.0116	0.0116	0.0116
29	0.0114	0.0114	0.0114	0.0115	0.0115	0.0115	0.0115	0.0116	0.0116	0.0116
30	0.0113	0.0113	0.0114	0.0114	0.0114	0.0115	0.0115	0.0115	0.0115	0.0116
31	0.0112	0.0113	0.0113	0.0113	0.0114	0.0114	0.0114	0.0115	0.0115	0.0115
32	0.0111	0.0112	0.0112	0.0113	0.0113	0.0113	0.0114	0.0114	0.0114	0.0115
33	0.011	0.0111	0.0111	0.0112	0.0112	0.0113	0.0113	0.0113	0.0114	0.0114
34	0.0108	0.0109	0.011	0.011	0.0111	0.0112	0.0112	0.0113	0.0113	0.0113
35	0.0106	0.0107	0.0108	0.0109	0.011	0.0111	0.0111	0.0112	0.0112	0.0113
36	0.0104	0.0105	0.0106	0.0107	0.0108	0.0109	0.011	0.0111	0.0111	0.0112
37	0.0102	0.0103	0.0104	0.0105	0.0107	0.0108	0.0109	0.0109	0.011	0.0111
38	0.0099	0.0101	0.0102	0.0103	0.0105	0.0106	0.0107	0.0108	0.0109	0.011
39	0.0096	0.0098	0.01	0.0101	0.0102	0.0104	0.0105	0.0106	0.0107	0.0108
40	0.0094	0.0096	0.0097	0.0099	0.01	0.0102	0.0103	0.0104	0.0106	0.0107
41	0.0091	0.0093	0.0095	0.0097	0.0098	0.01	0.0101	0.0103	0.0104	0.0105
42	0.0088	0.009	0.0092	0.0094	0.0096	0.0098	0.0099	0.0101	0.0102	0.0104
43	0.0086	0.0088	0.009	0.0092	0.0094	0.0096	0.0098	0.0099	0.0101	0.0102
44	0.0084	0.0086	0.0089	0.0091	0.0093	0.0095	0.0096	0.0098	0.01	0.0101
45	0.0083	0.0086	0.0088	0.009	0.0092	0.0094	0.0096	0.0098	0.0099	0.0101

Appendix Table 8.10. Flux (table data)-rotor angle(first column)-current (first row) values extracted from FEMM

	41	42	43	44	45	46	47	48	49	50
1	0.0103	0.0104	0.0105	0.0107	0.0108	0.0109	0.011	0.011	0.0111	0.0112
2	0.0103	0.0105	0.0106	0.0107	0.0108	0.0109	0.011	0.0111	0.0111	0.0112
3	0.0105	0.0106	0.0107	0.0108	0.0109	0.011	0.0111	0.0111	0.0112	0.0112
4	0.0106	0.0107	0.0108	0.0109	0.011	0.0111	0.0111	0.0112	0.0112	0.0113
5	0.0107	0.0108	0.0109	0.011	0.0111	0.0111	0.0112	0.0113	0.0113	0.0113
6	0.0109	0.011	0.011	0.0111	0.0112	0.0112	0.0113	0.0113	0.0113	0.0114
7	0.011	0.0111	0.0111	0.0112	0.0112	0.0113	0.0113	0.0114	0.0114	0.0114
8	0.0111	0.0112	0.0112	0.0113	0.0113	0.0113	0.0114	0.0114	0.0114	0.0115
9	0.0112	0.0112	0.0113	0.0113	0.0114	0.0114	0.0114	0.0115	0.0115	0.0115
10	0.0113	0.0113	0.0114	0.0114	0.0114	0.0115	0.0115	0.0115	0.0115	0.0116
11	0.0113	0.0114	0.0114	0.0114	0.0115	0.0115	0.0115	0.0116	0.0116	0.0116
12	0.0114	0.0114	0.0115	0.0115	0.0115	0.0115	0.0116	0.0116	0.0116	0.0116
13	0.0115	0.0115	0.0115	0.0115	0.0116	0.0116	0.0116	0.0116	0.0117	0.0117
14	0.0115	0.0115	0.0116	0.0116	0.0116	0.0116	0.0117	0.0117	0.0117	0.0117
15	0.0116	0.0116	0.0116	0.0116	0.0117	0.0117	0.0117	0.0117	0.0117	0.0118
16	0.0116	0.0116	0.0116	0.0117	0.0117	0.0117	0.0117	0.0118	0.0118	0.0118
17	0.0116	0.0117	0.0117	0.0117	0.0117	0.0118	0.0118	0.0118	0.0118	0.0118
18	0.0117	0.0117	0.0117	0.0118	0.0118	0.0118	0.0118	0.0118	0.0119	0.0119
19	0.0117	0.0117	0.0118	0.0118	0.0118	0.0118	0.0118	0.0119	0.0119	0.0119
20	0.0118	0.0118	0.0118	0.0118	0.0118	0.0119	0.0119	0.0119	0.0119	0.0119
21	0.0118	0.0118	0.0118	0.0119	0.0119	0.0119	0.0119	0.0119	0.0119	0.012
22	0.0118	0.0118	0.0119	0.0119	0.0119	0.0119	0.0119	0.0119	0.012	0.012
23	0.0118	0.0118	0.0119	0.0119	0.0119	0.0119	0.0119	0.012	0.012	0.012
24	0.0118	0.0118	0.0118	0.0119	0.0119	0.0119	0.0119	0.0119	0.012	0.012
25	0.0118	0.0118	0.0118	0.0118	0.0119	0.0119	0.0119	0.0119	0.0119	0.012
26	0.0117	0.0118	0.0118	0.0118	0.0118	0.0118	0.0119	0.0119	0.0119	0.0119
27	0.0117	0.0117	0.0117	0.0118	0.0118	0.0118	0.0118	0.0118	0.0119	0.0119
28	0.0117	0.0117	0.0117	0.0117	0.0117	0.0118	0.0118	0.0118	0.0118	0.0118
29	0.0116	0.0116	0.0117	0.0117	0.0117	0.0117	0.0118	0.0118	0.0118	0.0118
30	0.0116	0.0116	0.0116	0.0116	0.0117	0.0117	0.0117	0.0117	0.0118	0.0118
31	0.0115	0.0116	0.0116	0.0116	0.0116	0.0117	0.0117	0.0117	0.0117	0.0117
32	0.0115	0.0115	0.0115	0.0116	0.0116	0.0116	0.0116	0.0117	0.0117	0.0117
33	0.0114	0.0115	0.0115	0.0115	0.0115	0.0116	0.0116	0.0116	0.0116	0.0117
34	0.0114	0.0114	0.0114	0.0115	0.0115	0.0115	0.0115	0.0116	0.0116	0.0116
35	0.0113	0.0113	0.0114	0.0114	0.0114	0.0115	0.0115	0.0115	0.0116	0.0116
36	0.0112	0.0113	0.0113	0.0113	0.0114	0.0114	0.0114	0.0115	0.0115	0.0115
37	0.0111	0.0112	0.0113	0.0113	0.0113	0.0114	0.0114	0.0114	0.0115	0.0115
38	0.011	0.0111	0.0112	0.0112	0.0113	0.0113	0.0113	0.0114	0.0114	0.0115
39	0.0109	0.011	0.0111	0.0111	0.0112	0.0112	0.0113	0.0113	0.0114	0.0114
40	0.0108	0.0109	0.011	0.0111	0.0111	0.0112	0.0112	0.0113	0.0113	0.0114
41	0.0107	0.0108	0.0109	0.011	0.011	0.0111	0.0112	0.0112	0.0113	0.0113
42	0.0105	0.0106	0.0107	0.0108	0.0109	0.011	0.0111	0.0112	0.0112	0.0113
43	0.0104	0.0105	0.0106	0.0108	0.0109	0.0109	0.011	0.0111	0.0112	0.0112
44	0.0103	0.0104	0.0106	0.0107	0.0108	0.0109	0.011	0.0111	0.0111	0.0112
45	0.0102	0.0104	0.0105	0.0106	0.0108	0.0109	0.011	0.011	0.0111	0.0112

RESUME

He graduated from Kanuni Anatolian High School in 2004. He earned his Bachelor of Science degree from Karadeniz Technical University Electrical and Electronics Engineering Department in 2008. He earned his master's degree in 2014 from Gebze Institute of Technology Mechanical Engineering Department. He knows English.

The peer-reviewed article published from this Ph.D. thesis is:

Aydemir, M., Okumus, H.I., Phase flux linkage estimation of external rotor switched reluctance motor with NARX neural network, Springer Electrical Eng (2023). https://doi.org/10.1007/s00202-022-01726-x